TURBULENT HEAT TRANSFER IN SUPERCRITICAL FLUIDS UNDER TRANSCRITICAL TEMPERATURE CONDITIONS

A Dissertation

Submitted to the Faculty

of

Purdue University

by

Kukjin Kim

In Partial Fulfillment of the

Requirements for the Degree

of

Doctor of Philosophy

August 2018

Purdue University

West Lafayette, Indiana

THE PURDUE UNIVERSITY GRADUATE SCHOOL
STATEMENT OF DISSERTATION APPROVAL

Dr. Carlo Scalo, Chair

School of Mechanical Engineering

Dr. Issam A. Mudawar

School of Mechanical Engineering

Dr. Eckhard A. Groll

School of Mechanical Engineering

Dr. Jean-Pierre Hickey

Department of Mechanical and Mechatronics Engineering (Univ. of Waterloo)

Approved by:

Dr. Jay P. Gore

Associate Head for Graduate Studies

To my dearly beloved maternal grandmother in heaven

ACKNOWLEDGMENTS

I would like to express my gratitude to my advisor, Prof. Carlo Scalo, for giving me a chance to study and research at Purdue University. His expert guidance, patience, and encouragement throughout my Ph.D. study are truly appreciated. I am thanking Prof. Jean-Pierre Hickey for being my co-advisor as well as valuable discussions, suggestions, and feedback. I also thank my committee members, Profs. Issam A. Mudawar and Eckhard A. Groll for their helpful comments.

My research work has been partly supported by the Purdue/Rolls-Royce University Technology Center (UTC) grant in Advanced Thermal Management Systems lead by Mr. Pat Sweeney (Rolls-Royce, Indianapolis) and Prof. Stephen D. Heister (lead PI, Purdue). This support is greatly appreciated.

I am thankful to my labmates, Jean-Baptiste Chapelier, Rikhi Bose, Prateek Gupta, Mario Tindaro Migliorino, Zongxin Yu, Victor Sousa, Danish Patel, Emmanuel Gil Torres, Yongkai Chen, and Shubham Thirani in Compressible Flow and Acoustics Lab for all the times we have discussed and shared.

I would like to thank my best friends, Noyoung Kwak and Jaehoon Chang, and my brother, Chansoo Kim. Without their encouragement, I could not finish my Ph.D. study.

My heartfelt appreciation and thanks go to my father and my mother for their boundless love and support. My father has always given a sincere praise and encouragement and cheered me up whenever I have faced challenges. My mother prays every single day for my happiness and success with her unfailing patience. I am immensely grateful to them. My maternal grandmother whom I miss dearly, I believe that she would be pleased to hear me finish well and graduate.

Finally, to my lover, Eunmin Koh, I express thanks and love from the bottom of my heart.

TABLE OF CONTENTS

Page

LIST OF TABLES

Table Page

LIST OF FIGURES

Figure Page

Figure Page

Figure Page

Figure Page

Figure Page

ABSTRACT

Kim, Kukjin PhD, Purdue University, August 2018. Turbulent Heat Transfer in Supercritical Fluids Under Transcritical Temperature Conditions. Major Professor: Carlo Scalo, School of Mechanical Engineering.

Boiling at the ambient pressure undergoes a critical heat flux in the nucleate boiling regime and it determines the thermal efficiency and the applicable range of heat flux (low/moderate heat flux, $<10^5$ W/m^2; high heat flux, 2.5×10^5–10^7 W/m^2; ultra-high heat flux, 10^7–10^9 W/m^2). Since the regime beyond the critical heat flux shows a significant reduction in the overall achievable heat transfer rate, it is a reference for efficient heat transfer.

We propose to investigate supercritical fluids to overcome such a limit. A supercritical state is reached when the fluid is at temperatures and pressures exceeding its critical point. The supercritical fluid has simultaneously a liquid-like density and gas-like diffusivity, without a distinctive phasechange or surface tension, with the potential of overcoming deleterious effects and limitations of classical boiling.

In this study, we have performed direct numerical simulations solving the compressible Naview–Stokes equations for natural (R-134a, carbon dioxide, and methanol) and forced (R-134a) convection in transcritical temperature ranges in order to investigate and discuss the phenomena of pseudophase change with a specific focus on the heat transfer and turbulence structures/dynamics using structural and statistical approaches.

In natural convection pseudoboiling at supercritical pressure in transcritical temperature ranges ($\Delta T = 1$ K, 5 K, 20 K, and 40 K where ΔT is bottom-to-top temperature difference), increasing ΔT leads to the higher recirculation frequencies, enhancement of heat transfer, and breakup of global circulating motion. Two-dimensional simulations have limitations to proper prediction of the flow dynamics and heat flux

compared to three-dimensional ones. The proposed heat transfer correlation explains the natural convection pseudoboiling well, yet not perfectly. The real fluid effects cause the large thermodynamic gradients at the pseudotransition interface and increasing ΔT requires finer grid resolution due to unresolved length scales.

Turbulent forced convection is studied with $\Delta T = 5$ K, 10 K, and 20 K ($T_{top/bot} = T_{pb} \pm \Delta T/2$). At these conditions, a pseudophase change occurs at various wall-normal locations within the turbulent channel from $y_{pb}/h = -0.23$ ($\Delta T = 5$ K) to 0.89 ($\Delta T = 20$ K), where h is the channel half-height and $y = 0$ the centerplane position. Increases in ΔT also result in increasing wall-normal gradients in the semi-local friction Reynolds number. Classical, compressible scaling laws of the mean velocity profile are unable to fully collapse real fluid effects in this flow. The proximity to the pseudotransitioning layer inhibits the turbulent velocity fluctuations, while enhancing the temperature and density fluctuations. The latter reach peak values (relative to their mean) comparable to what is observed in a $M = 3.0$ ideal gas isothermal-wall compressible turbulent channel flow. Conditional probability analysis reveals that the sheet of fluid undergoing pseudophase change is characterized by a dramatic reduction in the kurtosis of density fluctuations, hence becoming thinner as ΔT is increased. Instantaneous visualizations show dense fluid ejections from the pseudoliquid viscous sublayer, some reaching the channel core, causing positive values of density skewness in the respective buffer layer region (vice versa for the top wall) and an impoverishment of the turbulent flow structure population near pseudotransitioning conditions.

1 INTRODUCTION

This chapter provides a brief background on critical heat flux and thermodynamic characteristics at supercritical conditions. Subsequently, natural/forced convection in supercritical fluids are introduced, and finally the objectives and the outline of the dissertation are presented.

1.1 Critical Heat Flux, Supercritical Condition, and Pseudophase Change

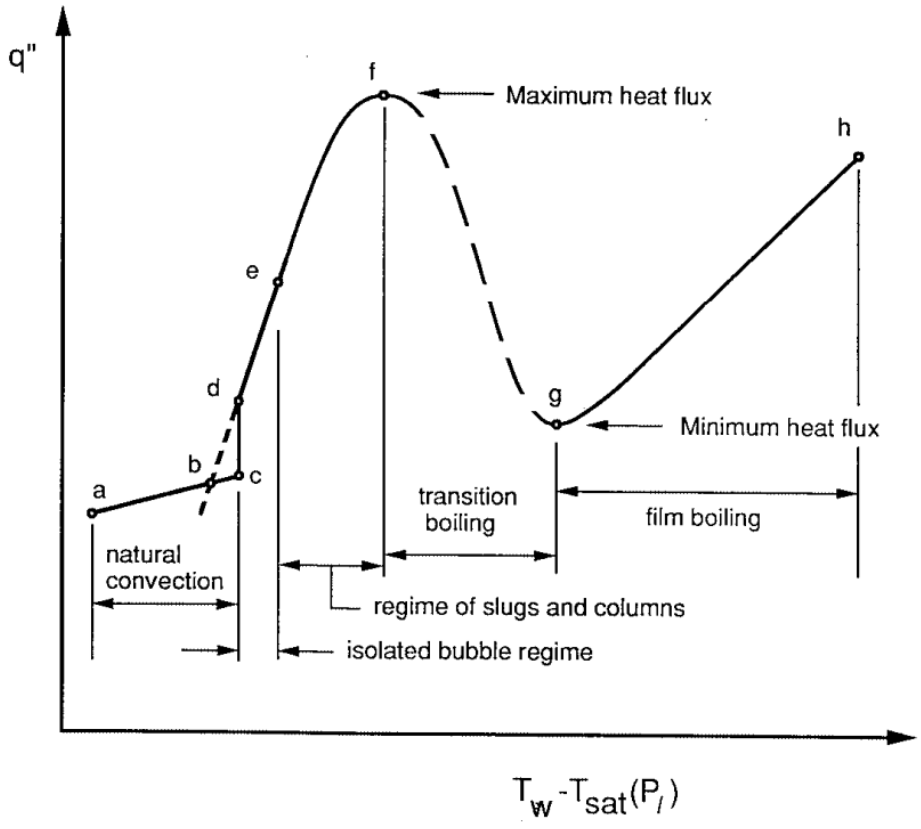

Figure 1.1. Boiling regimes and heat flux trend with increasing wall temperature [1].

In a typical pool boiling experiment, e.g. a heated plate submerged in water, the state of flow undergoes several transitions as the plate temperature is increased as shown in Figure 1.1. Initially, natural convection occurs and then boiling starts when temperature reaches a certain value. As temperature keeps increasing, the second state, isolated bubble regime, is observed which is followed by the third state characterized with slugs and columns. These two states can be both referred to as nucleate boiling. In the final stage of nucleate boiling, heat flux is maximized, reaching a so-called critical heat flux (CHF, also termed a boiling crisis) which is a key factor determining the thermal efficiency and limiting the range of applicability (low/moderate heat flux, $<10^5$ W/m^2; high heat flux, 2.5×10^5–10^7 W/m^2; ultra-high heat flux, 10^7–10^9 W/m^2). In transition boiling as the fourth regime, heat flux deteriorates and decreases rapidly. Finally, only when the fifth state, film boiling, is achieved, the heat flux rises again. Namely, the CHF refers to the maximum attainable heat flux before cessation of nucleate boiling so that causes low efficiency of heat transfer in transition boiling and it is essentially based on the phase change mechanism between liquid and vapor [1, 2].

The operating pressure of propulsion systems and power generators, such as gas turbines, liquid rocket engines, or supercritical water-cooled reactors, is continuously increasing in order to improve mechanical and thermodynamics performances. As a result, the working fluid often reaches pressures and temperatures exceeding its critical values, $p > p_{cr}$ and $T > T_{cr}$ respectively, hence achieving a supercritical state, and the fluid in that regime is named a supercritical fluid (see Figure 1.2).

The lay understanding is that supercritical fluids share properties of both gases and liquids, in a seemingly homogeneous, yet ambiguous state of matter, such as surface tension converging to zero, liquid-like density, and gas-like diffusivity [3, 4]. In reality, there is an identifiable transition between pseudoliquid (or liquid-like) and pseudogas (or gas-like) conditions, especially in the vicinity of the critical point corresponding to a transcritical temperature regime, determined by the pseudoboiling line (PBL) or the Widom line defined as the set of maxima of the thermodynamic corre-

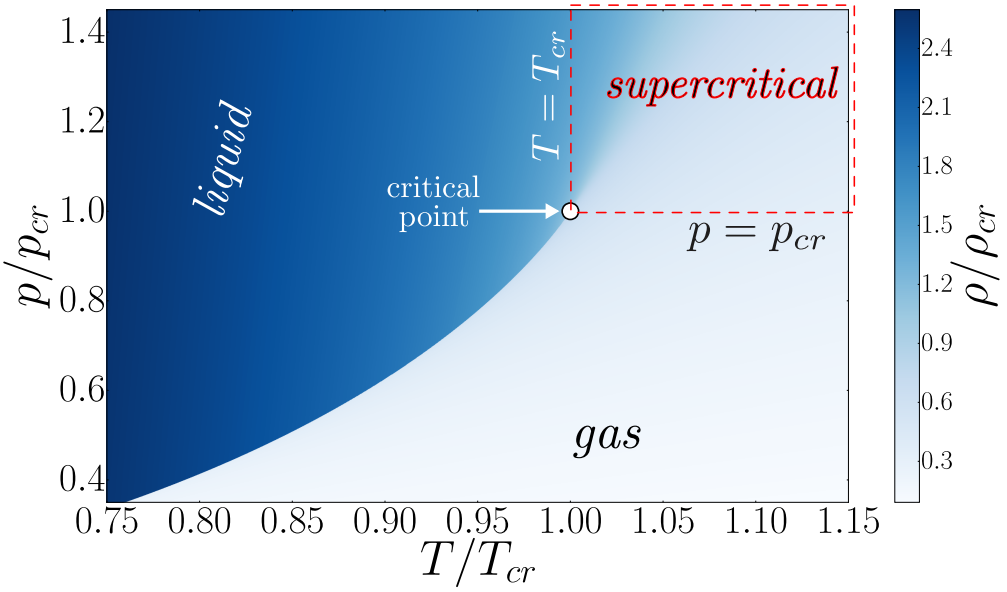

Figure 1.2. Pressure-temperature phase diagram showing the critical point ($T = T_{cr}$, $p = p_{cr}$) and the supercritical regime ($T > T_{cr}$, $p > p_{cr}$) (Credit: Mario Tindaro Migliorino).

lation lengths [5] and the maximum correlation length is represented with various response functions which are the second derivative of thermodynamic potential [5–10]. The PBL is an extension of the subcritical liquid-gas coexistence curve above the critical point [11] and is hereafter defined as the locus of pressure and temperature values ($p_{pb} > p_{cr}$, $T_{pb} > T_{cr}$) at which the thermal expansion coefficient of the fluid, $\alpha_p = -\left(\partial\rho/\partial T\right)_p/\rho$, is maximum. A pseudophase transition, or simply pseudotransition, occurs, for example, when temperature changes from $T < T_{pb}$ to $T > T_{pb}$ (or vice versa), for given pressure conditions $p = p_{pb}$, hence crossing the PBL in the $p-T$ phase diagram.

Unlike a subcritical phase change where the concept of latent heat accounts for the discontinuity of enthalpy, supercritical pseudotransition takes place progressively over a finite temperature range bracketing pseudoboiling (PB) conditions. While molecules are homogeneously distributed in space with a well-defined mean free path in the liquid-like ($T << T_{pb}$) or gas-like ($T >> T_{pb}$) supercritical states, heteroge-

neously distributed microscopic clusters of tightly packed molecules are formed during pseudotransition [12]. This results in abrupt changes in compressibility and density and a rapid, albeit continuous, increase in the heat capacity with gas-like behavior retained between denser molecular clusters as well as optical dispersion effects allowing the experimental identification of pseudotransition [8, 13].

1.2 Natural/Forced Convection in Supercritical Fluids

In modern engineering applications, improvement in heat transfer is a key issue in terms of thermodynamic efficiency and thermal instability/fatigue since mechanical integration and complexity become higher, especially in advanced power systems operating at supercritical pressure, and most of the heat transfer mechanism are intimately related to natural and forced convection.

Natural convection by the buoyancy effect has been applied for pumping fluids or cooling advanced systems such as a thermal pump, a solar heating system, and a nuclear reactor in the supercritical environment and their performance and stability have been studied [14–23]. While higher flow rate in a natural convection loop system can be achieved by loading the working fluid initially near its pseudoboiling region as well as large density difference between a cooling and a heating part [14], high speed flow causes a steep gradient of near-wall temperature and as a result, high heat transfer coefficient is accompanied [15]. It has been reported that approaching the critical point increases the heat transfer coefficient [16] and accelerates heat transfer significantly by a so-called '*piston effect*' [24–26]. Hasan & Farouk [17] investigated that in the nearcritical natural convection, the mechanism of thermal energy transport is highly dependent on the Rayleigh number, pressure, and temperature and a divergence of bulk viscosity near the critical point affects the boundary layer development. However, abnormal flow instability with pressure perturbation is observed near the pseudoboiling point (PBP) due to the rapid variation of thermodynamic properties [18, 19] and the pressure perturbation is responsible for the repetitive reversal

flow in the natural convection circulation loop [20, 21]. Chen *et al.* [22] reported that in the transcritical temperature and supercritical pressure regime of carbon dioxide, there exists the second transition point beyond the PBP at which viscosity and thermal conductivity begin increasing after a sharp decrease near the PBP and therefore, it impedes flow acceleration and improves heat transfer resulting in a stabilized flow pattern. Also, supercritical carbon dioxide flow in a large diameter pipe (D = 15 mm) is more stable with smoothened velocity profiles compared to a small one (D = 6 mm) [23]. Even though some studies have suggested supercritical heat transfer correlations predicting the unusual deterioration phenomenon as well as the normal and enhanced heat transfer regions in forced convection [27–29] or covering the behaviors in the nearcritical regime along with far from the critical point in natural convection [14, 15, 30, 31], a robust explanation has not been obtained yet due to the complexity of combined factors and the drastic variations of thermodynamic properties [32–34].

Even though forced convection needs additionally complex devices controlling fluid flow compared to natural convection, it has been studied in various aspects, such as heat transfer, turbulent characteristics, and thermodynamic fluctuations affected by real fluid effects, because of its more pratical use in the mechanical systems. The characteristics of supercritical fluid have been found to avoid the CHF and increase the gross thermal efficiency [35]. Also, heat transfer is enhanced near the PBP where specific heat and thermal conductivity have a peak or a hump [36] and it is amplified by turbulence effects in forced convection [37]. Nevertheless, such high heat transfer performance in the pseudoboiling might be hindered due to a pseudofilm boiling phenomenon similar to film boiling under subcritical pressures [38]. Experimental studies on forced convection in supercritical water flow by Yamagata *et al.* [39] showed that at high heat fluxes relatively to the flow rate, the deterioration in heat transfer occurs with the sharply increased wall temperature that the reason is not explained clearly, but is presumed to be due to the pseudofilm boiling. On the other hand, Shiralkar & Griffith [40] found that conditions of the high ratio of heat flux to flow rate, low

inlet enthalpy, and nearcritical pressure make the heat transfer deterioration larger. Also, Liao & Zhao [41] discerned that buoyancy affects heat transfer coefficients significantly even in forced convection, from their experiments through comparison between the flow orientations (horizontal and vertical) of supercritical carbon dioxide. Bae *et al.* [42] reported that high turbulence level in the upward flow improves the heat transfer impairment related to the buoyancy effect. Especially, stong temperature fluctuation near the wall (i.e., a thin thermal boundary layer) promotes heat transfer to the supercritical pressure flows [43, 44].

1.3 Relevance to Gas Turbine Engine Applications

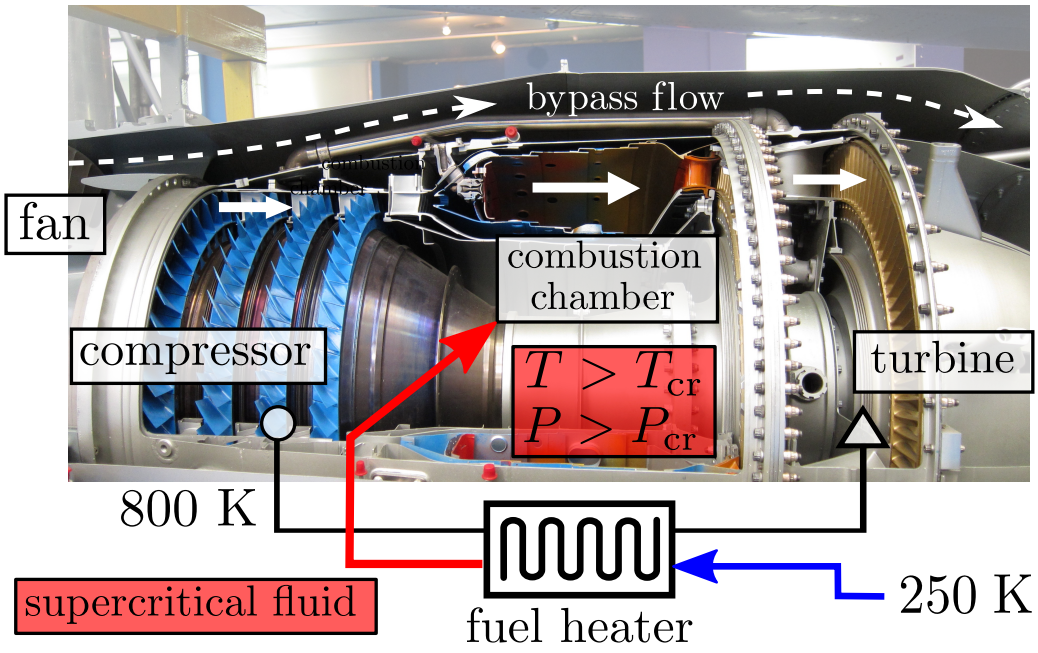

Figure 1.3. Core section of a Rolls-Royce Turboméca Adour turbofan displayed at the Musée de l'Air in Paris, France with air flow from left to right (Credit: Olivier Cleynen).

Fuel in aeronautical applications is typically stored in subcritical temperature conditions (e.g. in the wings of an airplane at cruising conditions where outside air temperatures reach −40 °C) under high pressures, due to the pumping power necessary

to allow fuel to be delivered to the engines. Fuel gets heated to improve combustion efficiency before it reaches the combustion chamber by oil and other fluids that, in turn, need to be cooled (see Figure 1.3). Hot lubricant oil, for example, exiting the gear box of the new Ultrafan engine by Rolls-Royce, carries approximately 500 W of heat to be dissipated.

Fluid dynamic instabilities commonly occur in highly pressurized systems. These instabilities typically occur in fluids that are: (1) pressurized slightly above their critical point ($p > p_{cr}$); and (2) heated at or above their critical temperature T_{cr} (hence *transcritical*), where the pseudoboiling occurs. Also, heightened coupling among pressure, temperature, and density in the transcritical or near-critical regime, $p \simeq p_{cr}$ and $T \simeq T_{cr}$, accentuates the unwanted instabilities, similar to thermoacoustic oscillations, in the injection systems leading to the combustion chamber [45] as well as fuel heat exchangers, also illustrated in Figure 1.3 [46–48]; the intense flow oscillations often lead to catastrophic hardware failure, if uncontrolled. These so-called real fluid effects have already been reproduced in recent experiments at Purdue and are under investigation in other efforts carried out in Dr. Scalo's lab.

One example of where a usable temperature difference to drive cooling devices can be found is between the bypass flow duct and the combustion chamber. Also, results from a recent review meeting held in Rolls-Royce Indianapolis yielded the following

Table 1.1. Operating temperature conditions in the gas turbine engine.

	Type	T (°C)		Type	T (°C)
1	Fan air	40	A	Turbine casing	430
2	Fuel	20–120	B	CDT	650
3	Ambient air	−40	C	Turbine exhaust air	430
4	Aircraft skin	50	D	Oil	200
5	CDT air	–	E	Turbine flow	1500
6	Oil	65	F	Electric generator	200

possible cold (left) and hot (right) pairing options within the gas turbine engine (see Table 1.1) and possible cold/hot sink pairings are 1-A, 6-F, 5-E,1-C, 2-B, 3-F which could drive a supercritical boiling device.

1.4 Research Objectives and Dissertation Outline

The objectives of this study are to develop high-quality numerical simulation tools which can model the pseudophase change in supercritical fluids and investigate its turbulent heat transfer dynamics. Setups explored here (Setups A and B) study natural and forced convection in supercritical fluids between two isothermal boundaries at a given temperature difference, ΔT. The novelty of the proposed approach is to operate working fluids at supercritical pressures, and specifically along the PBL, achieving transcritical or pseudophase changing conditions.

Chapter 2 presents the governing equations for a fully compressible flow (Section §2.1) and the thermodynamic models (Section §2.2) which account for the real fluid effects (e.g. supercritical conditions) and were implemented into the high-order compressible Navier–Stokes solver, *Hybrid* (Section §2.3). The computational setups for the natural convection pseudoboiling and the turbulent forced convection study are outlined in Section §2.4.

In Chapter 3, the effects of pseudoboiling on natural convection dynamics are analyzed via comparisons between two-dimensional and three-dimensional simulations (Section §3.1); instantaneous flow field and wall heat flux analysis, heat transfer correlation, and probability density functions (PDF). Also, turbulent statistics of mean and fluctuating quantities and its structures are presented (Section §3.2).

Chapter 4 presents the turbulent mean and fluctuating hydro- and thermodynamic quantities with grid convergence study in turbulent forced convection (Section §4.2) followed by analysis on PDF and turbulent energy spectra (Section §4.3). Instantaneous turbulent structures are investigated and compared with the correlation

statistics to infer their role in the heat transfer near the walls of the turbulent channel flow (Section §4.4).

2 PROBLEM FORMULATION

2.1 Governing Equations for Compressible Flow

The governing equations of mass, momentum, and total energy for a fully compressible flow in the turbulent forced convection study are solved in conservative form, which reads

$$\frac{\partial \rho}{\partial t} + \frac{\partial \rho u_j}{\partial x_j} = 0 \tag{2.1}$$

$$\frac{\partial \rho u_i}{\partial t} + \frac{\partial \rho u_i u_j}{\partial x_j} = -\frac{\partial p}{\partial x_j} + \frac{\partial \tau_{ij}}{\partial x_j} \tag{2.2}$$

$$\frac{\partial \rho E}{\partial t} + \frac{\partial}{\partial x_j}\left[u_j\left(\rho E + p\right)\right] = \frac{\partial}{\partial x_j}\left(u_i \tau_{ij} - q_j\right) \tag{2.3}$$

where t is time, x_j $(j = 1, 2, 3)$ the coordinates in x, y, and z direction, u_j the velocity component in each direction, ρ the density, p the pressure, and E the total energy per unit mass. Unless otherwise stated, all symbols refer to dimensional quantities.

In order to solve the spurious pressure oscillation issue observed more conspicuously in the natural convection pseudoboiling, we implemented the pressure evolution equation derived by Kawai *et al.* [49] instead of using the total energy equation and it reads

$$\frac{\partial p}{\partial t} + \frac{\partial p u_j}{\partial x_j} + \left(\rho c^2 - p\right)\frac{\partial u_j}{\partial x_j} = \frac{\alpha_p}{\rho c_v \kappa_T}\left(\tau_{ij}\frac{\partial u_i}{\partial x_j} - \frac{\partial q_j}{\partial x_j} + u_i f_i\right) \tag{2.4}$$

where $f_i(= \rho g)$ is the body force, g the gravitational acceleration, c the speed of sound, $\alpha_p(= \left(\partial p/\partial T\right)_\rho / \left[\rho\left(\partial p/\partial \rho\right)_T\right])$ the isobaric thermal expansion coefficient, c_v the heat capacity at constant volume, $\kappa_T\left(= 1/\left[\rho\left(\partial p/\partial \rho\right)_T\right]\right)$ the isothermal compressibility coefficient, and T the temperature.

The viscous and conductive heat fluxes in Equations (2.2) and (2.3) are, respectively

$$\tau_{ij} = 2\mu\left[S_{ij} - \frac{1}{3}\frac{\partial u_k}{\partial x_k}\delta_{ij}\right] \tag{2.5}$$

$$q_j = -\lambda\frac{\partial T}{\partial x_j} = -\frac{c_p\mu}{Pr}\frac{\partial T}{\partial x_j} \tag{2.6}$$

where μ is the dynamic viscosity, λ the thermal conductivity, S_{ij} the strain rate tensor given by $S_{ij} = \left(\partial u_j/\partial x_i + \partial u_i/\partial x_j\right)/2$, c_p the heat capacity at constant pressure, and Pr the Prandtl number.

2.2 Modeling of Thermodynamic and Transport Properties for Real Fluids

The Peng–Robinson (PR) equation of state (EOS) [50] is implemented to model the working fluids of choice for this study, R-134a (1,1,1,2-tetrafluoroethane, CH_2FCF_3), carbon dioxide (CO_2), and methanol (CH_3OH) for the natural convection pseudoboiling and R-134a for the turbulent forced convection. Departure functions guaranteeing full thermodynamic consistency with the chosen EoS have been derived following Ewing & Peters [51]. Transport properties such as viscosity and thermal conductivity are estimated via the Chung's method [52], which predicts experimental values within 5% error [53]. The choice of an accurate and simple equation of state such as the PR EoS provides a consistent thermodynamic model, computationally less expensive than interpolating tabulated values.

The PR EoS reads

$$p = \frac{R_u T}{v_m - b} - \frac{a\alpha}{v_m^2 + 2bv_m - b^2} \tag{2.7}$$

$$a = \frac{0.45724 R_u^2 T_{cr}^2}{p_{cr}} \qquad b = \frac{0.07780 R_u T_{cr}}{p_{cr}}$$

$$\alpha = \left[1 + \left(0.37464 + 1.54226\omega - 0.26992\omega^2\right)\left(1 - T_r^{0.5}\right)\right]^2$$

where R_u is the universal gas constant, v_m the molar volume, ω the acentric factor, and $T_r = T/T_{cr}$ the reduced temperature. The terms, a, b, and α account for intermolecular attractive and repulsive effect and nonspherical shape of molecules.

The thermodynamic relations based on the PR EoS that incorporate departure functions are

$$e\left(T,\ \rho\right) = e^0\left(T\right) + \frac{1}{\sqrt{8}bM_w}\left[T\left(\frac{\partial a\alpha}{\partial T}\right) - a\alpha\right]\ln\left(\frac{M_w + \left(1+\sqrt{2}\right)b\rho}{M_w + \left(1-\sqrt{2}\right)b\rho}\right) \tag{2.8}$$

$$h\left(T,\ \rho\right) = e\left(T,\ \rho\right) + \frac{p}{\rho} \tag{2.9}$$

$$c_v\left(T,\ \rho\right) = c_v^0\left(T\right) + \frac{T}{\sqrt{8}bM_w}\left(\frac{\partial^2 a\alpha}{\partial T^2}\right)\ln\left(\frac{M_w + \left(1+\sqrt{2}\right)b\rho}{M_w + \left(1-\sqrt{2}\right)b\rho}\right) \tag{2.10}$$

$$c_p\left(T,\ \rho\right) = c_v\left(T,\ \rho\right) + \frac{T}{\rho^2}\left(\frac{\partial p}{\partial T}\right)_\rho^2 \Bigg/ \left(\frac{\partial p}{\partial \rho}\right)_T \tag{2.11}$$

$$\gamma\left(T,\ \rho\right) = \frac{c_p\left(T,\ \rho\right)}{c_v\left(T,\ \rho\right)} \tag{2.12}$$

$$c\left(T,\ \rho\right) = \sqrt{\gamma\left(T,\ \rho\right)\left(\frac{\partial p}{\partial \rho}\right)_T} \tag{2.13}$$

where e is the internal energy, h the enthalpy, c_v the heat capacity at constant volume, c_p the heat capacity at constant pressure, γ the specific heat ratio, c the speed of sound, and M_w the molecular weight. The superscript, 0, denotes the thermodynamic property of the equivalent ideal gas state.

Departure functions derived from the selected equation of state (partial derivatives in the relations for c_p and c) are given by

$$\left(\frac{\partial p}{\partial T}\right)_\rho = \frac{\rho R_u}{M_w - b\rho} - \left(\frac{\partial a\alpha}{\partial T}\right)\frac{\rho^2}{\left[M_w + \left(1+\sqrt{2}\right)b\rho\right]\left[M_w + \left(1-\sqrt{2}\right)b\rho\right]} \tag{2.14}$$

$$\left(\frac{\partial p}{\partial \rho}\right)_T = \frac{M_w R_u T}{\left(M_w - b\rho\right)^2} - \frac{2a\alpha\rho M_w\left(M_w + b\rho\right)}{\left[M_w + \left(1+\sqrt{2}\right)b\rho\right]^2\left[M_w + \left(1-\sqrt{2}\right)b\rho\right]^2} \tag{2.15}$$

The viscosity via the Chung's method is given by

$$\mu = \mu^* \frac{36.344\left(M_w T_{cr}\right)^{1/2}}{v_{m,c}^{2/3}} \tag{2.16}$$

where $v_{m,c}$ is the critical molar volume and μ^* is

$$\mu^* = \frac{(T^*)^{1/2}}{\Omega_v} F_c \left[(G_2)^{-1} + A_6 y\right] + \mu^{**} \tag{2.17}$$

T^*, Ω_v, and F_c are given as

$$T^* = 1.2593 T_r \tag{2.18}$$

$$\Omega_v = \left[A\left(T^*\right)^{-B}\right] + C\left[\exp\left(-DT^*\right)\right] + E\left[\exp\left(-FT^*\right)\right] + GT^{*B}\sin\left(ST^{*W} - H\right) \tag{2.19}$$

$$F_c = 1 - 0.2756\omega + 0.059035\mu_r^4 + \kappa_a \tag{2.20}$$

where κ_a is the association factor for hydrogen bonding effect of highly polar substances such as alcohols and acids, Ω_v and F_c mean the viscosity collision integral and consideration for the shape and polarity of molecules for dilute gases, respectively. The dimensionless dipole moment, μ_r, is given by

$$\mu_r = 131.3 \frac{\chi}{\left(v_{m,c} T_{cr}\right)^{1/2}} \tag{2.21}$$

where χ is the dipole moment of molecule.

The other terms appearing in the relationships above are as follows

$$y = \frac{\rho v_{m,c}}{6} \tag{2.22}$$

$$G_1 = \frac{1 - 0.5y}{(1-y)^3} \tag{2.23}$$

$$G_2 = \frac{A_1\left[\left[1 - exp\left(-A_4 y\right)\right]/y\right] + A_2 G_1 exp\left(A_5 y\right) + A_3 G_1}{A_1 A_4 + A_2 + A_3} \tag{2.24}$$

$$\mu^{**} = A_7 y^2 G_2 exp\left[A_8 + A_9\left(T^*\right)^{-1} + A_{10}\left(T^*\right)^{-2}\right] \tag{2.25}$$

$$A_i = a_0(i) + a_1(i)\,\omega + a_2(i)\,\mu_r^4 + a_3(i)\,\kappa_a \tag{2.26}$$

The thermal conductivity was developed by following a similar approach to viscosity.

$$\lambda = \frac{31.2\mu^0 \Psi}{M_w'}\left(G_2^{-1} + B_6 y\right) + qB_7 y^2 T_r^{1/2} G_2 \tag{2.27}$$

where

$$\mu^0 = 40.785 \frac{F_c\left(M_w T\right)^{1/2}}{v_{m,c}^{2/3}\Omega_v} \tag{2.28}$$

$$\Psi = 1 + \alpha \left(\frac{0.215 + 0.28288\alpha - 1.061\beta + 0.26665Z}{0.6366 + \beta Z + 1.061\alpha\beta} \right) \tag{2.29}$$

$$\alpha = \frac{c_v}{R_u} - 1.5 \tag{2.30}$$

$$\beta = 0.7862 - 0.7109\omega + 1.3168\omega^2 \tag{2.31}$$

$$Z = 2.0 + 10.5T_r^2 \tag{2.32}$$

$$M'_w = M_w/10^3 \tag{2.33}$$

$$q = 3.586 \times 10^{-3} \frac{(T_{cr}/M'_w)^{1/2}}{v_{m,c}^{2/3}} \tag{2.34}$$

For the term, G_2, the form is identical to the one of viscosity, but A_i is replaced with B_i which has the different values. All the other terms that are not defined and the empirical coefficients are found in Poling *et al.* [53]. In order to prove adequacy and accuracy of implementation of the equations, comparisons against the NIST database [54] and among the working fluids are included in Appendix A (Figures A.1–A.3).

2.3 High-Order Structured Compressible Navier–Stokes Solver: *Hybrid*

The proposed numerical simulations have been carried out with *Hybrid*, a fully compressible Navier–Stokes solver originally written by Prof. Johan Larsson. This code utilizes a finite central difference scheme with a fourth order accuracy by summation-by-parts (SBP) operators for the inviscid terms and a second order accuracy for the viscous terms. The time advancement is achieved by a fourth order accurate Runge–Kutta method. This code has been used in several canonical numerical investigations such as shock-vortex interaction, compressible homogeneous isotropic turbulence [55], and shock/turbulence interaction [56, 57]. *Hybrid* has also been recently scaled up to 2 million CPU cores [58]. The code solves single component fluid, which is a suitable modeling approach for a supercritical flow since for supercritical pressures, $p > p_{cr}$, surface tension becomes negligible and numerical techniques typical of multi-phase simulations, such as interface tracking or reconstruction, are not required. New

features that have been added to the code include parallel HDF5 [59] input/output capabilities as well as the PR EoS and the Chung's method.

2.4 Computational Setup

Two classic heat transfer problems extended to supercritical fluids will be tackled with the use of direct numerical simulations (DNS).

- Setup A: Pseudoboiling between two differentially heated plates with heat transfer driven by natural convection, with R-134a, carbon dioxide, and methanol as the working fluids
- Setup B: Pseudoboiling between two differentially heated plates with heat transfer driven by turbulent forced convection, with only R-134a as the working fluid

In both cases, the working fluid is kept in transcritical temperature conditions at supercritical pressure.

2.4.1 Setup A: Natural Convection Pseudoboiling

To simulate heat transfer in the natural convection pseudoboiling, a setup as shown in Figure 2.1 is employed. In the present study, the computational domain consists of bottom and top isothermal walls with a periodic boundary condition in the x and z directions. The assigned wall temperature conditions maintain the transcritical temperature regime with the hot bottom wall and the cold top wall by taking $T_{bot/top}$ as

$$T_{bot/top} = T_{pb} \pm \Delta T/2, \qquad \Delta T = T_{bot} - T_{top} \tag{2.35}$$

where T_{pb} is the pseudoboiling temperature. Gravity acts along the y direction as the body force which enables natural convection by the difference in density distribution near each wall, namely buoyancy.

Table 2.1. Simulation parameters of the natural convection pseudoboiling achieving the transcritical temperature regimes for R-134a, carbon dioxide, and methanol with box sizes, 4 mm × 2 mm for the two-dimension and 4 mm × 2 mm × 2 mm for the three-dimension. The subcripts '*b*', '*pb*', and '*cr*' indicate bulk, pseudoboiling, and critical properties.

Fluid	p_b	T_{pb} (K)	ΔT (K)	T_{bot} (K)	T_{top} (K)
R-134a (○)			1	379.6	378.6
CH_2FCF_3	$1.1\,p_{cr}$	379.1	5	381.6	376.6
p_{cr} = 40.59 bar			20	389.1	369.1
T_{cr} = 374.26 K			40	399.1	359.1
Carbon dioxide (△)			1	308.9	307.9
CO_2	$1.1\,p_{cr}$	308.4	5	310.9	305.9
p_{cr} = 73.74 bar			20	318.4	298.4
T_{cr} = 304.13 K			40	328.4	288.4
Methanol (□)			1	518.9	517.9
CH_3OH	$1.1\,p_{cr}$	518.4	5	520.9	515.9
p_{cr} = 80.97 bar			20	528.4	508.4
T_{cr} = 512.64 K			40	538.4	498.4

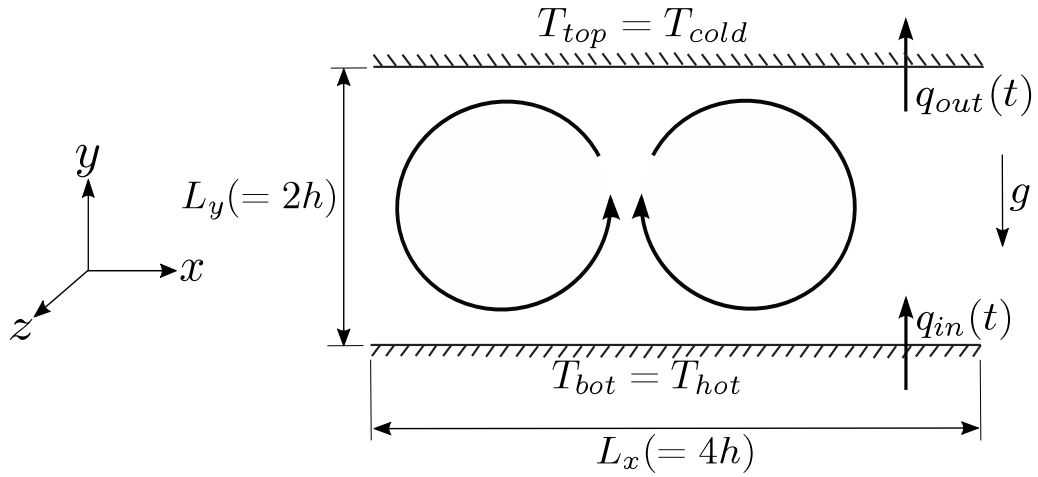

Figure 2.1. Schematic of the natural convection pseudoboiling in the transcritical temperature regime. Simulation parameters are given in Table 2.1.

The working fluids investigated are R-134a (CH_2FCF_3), carbon dioxide (CO_2), and methanol (CH_3OH) and their ΔT conditions are 1 K, 5 K, 20 K, and 40 K. The bulk pressure is set to 44.649 bar for R-134a, 81.114 bar for carbon dioxide, and 89.067 bar for methanol corresponding to 1.1 times the critical pressure of each fluid (see Table 2.1 for more details). Also, the accumulated dataset information in terms of the boiling cycle corresponding to each fluid and ΔT condition is shown in Tables 2.2 and 2.3

2.4.2 Setup B: Turbulent Forced Convection

The computational setup is a three-dimensional compressible turbulent channel flow for studying the turbulent forced convection (Figure 2.2) kept at a nominal bulk pressure of $p_b \simeq 1.1p_{cr}$, corresponding to the pseudoboiling temperature of $T_{pb} = 379.1$ K defined based on the maximum isobaric thermal expansion coefficient (Figure 2.3a). The assigned isothermal top and bottom wall boundary conditions bracket the pseudoboiling temperature, $T_{top/bot} = T_{pb} \pm \Delta T/2$, maintaining transcritical tem-

Table 2.2. Boiling cycle of the two-dimensional pseudoboiling for R-134a, carbon dioxide, and methanol at $p_b = 1.1p_{cr}$ and $\Delta T = 1$ K, 5 K, 20 K, and 40 K.

ΔT (K)	1	5	20	40
Fluid	R-134a			
$N_x \times N_y \times N_z$	128×128×1	256×256×1	512×512×1	128×128×1
Boiling cycle	6.000	6.071	2.900	7.222
(1 boiling cycle (s))	(0.500)	(0.280)	(0.130)	(0.090)
Fluid	Carbon dioxide			
$N_x \times N_y \times N_z$	128×128×1	256×256×1	512×512×1	128×128×1
Boiling cycle	5.571	2.653	4.917	6.325
(1 boiling cycle (s))	(0.350)	(0.170)	(0.120)	(0.080)
Fluid	Methanol			
$N_x \times N_y \times N_z$	128×128×1	256×256×1	256×256×1	64×64×1
Boiling cycle	4.615	4.952	6.667	33.333
(1 boiling cycle (s))	(0.650)	(0.250)	(0.120)	(0.090)

Table 2.3. Boiling cycle of the three-dimensional pseudoboiling for carbon dioxide at $p_b = 1.1p_{cr}$ and $\Delta T = 1$ K, 5 K, 20 K, and 40 K.

ΔT (K)	1	5	20	40
Fluid	Carbon dioxide			
$N_x \times N_y \times N_z$	128×128×64	256×256×128	256×256×128	128×128×64
Boiling cycle	5.571	0.788	1.375	6.988
(1 boiling cycle (s))	(0.350)	(0.170)	(0.120)	(0.080)

perature conditions in common with the natural convection pseudoboiling (Figure 2.3*b*), yet with the hot top wall and the cold bottom wall.

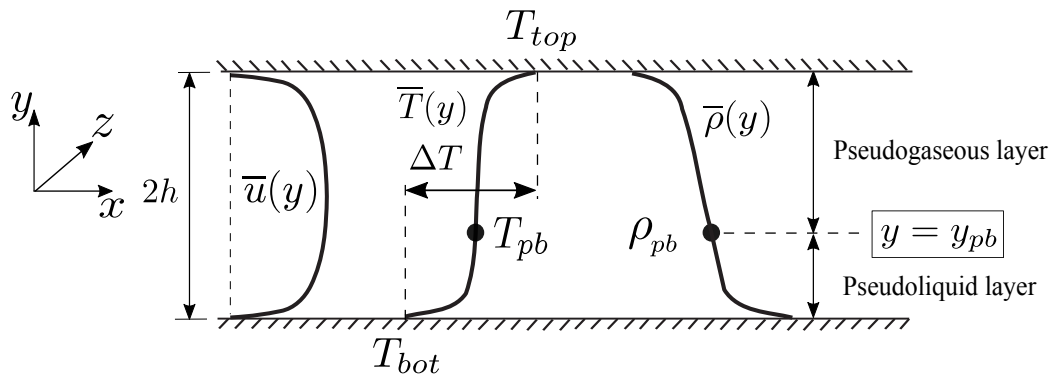

Figure 2.2. Schematic of the turbulent forced convection in the transcritical temperature regime. Simulation parameters are given in Tables 2.4 and 4.4.

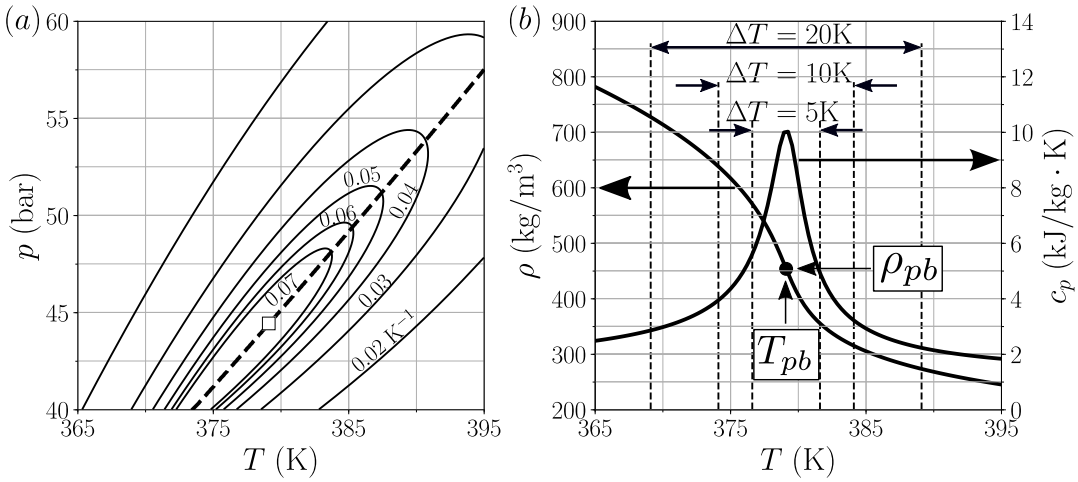

Figure 2.3. Phase diagram for R-134a showing the critical point (p_{cr} = 40.59 bar, T_{cr} = 374.26 K) (□), the pseudoboiling line (- - -), and the isolines of isobaric thermal expansion coefficient, α_p (——, K^{-1}) (a); density and isobaric heat capacity versus temperature for $p = 1.1p_{cr}$ with the pseudoboiling point (●) and top-to-bottom temperature differences, ΔT, bracketing T_{pb} = 379.1 K (b).

Top-to-bottom wall temperature differences investigated are $\Delta T = T_{top} - T_{bot}$ = 5 K, 10 K, and 20 K, with bulk density set to ρ_b = 450 kg/m^3, 474 kg/m^3, and 520 kg/m^3, respectively, determined via trial and error to obtain the desired bulk pressure for all cases (see Tables 2.4 and 4.4). Periodic boundary conditions are applied in

Table 2.4. Simulation parameters of the turbulent forced convection achieving the transcritical temperature regimes for R-134a with box sizes, 12 mm × 2 mm × 4 mm. The subcripts 'b', 'pb', and 'cr' indicate bulk, pseudoboiling, and critical properties.

Fluid	p_b	ρ_{pb} (kg/m^3)	T_{pb} (K)	ΔT (K)	T_{bot} (K)	T_{top} (K)	ρ_b (kg/m^3)	U_b (m/s)
R-134a (CH_2FCF_3)	$1.1p_{cr}$	453.5	379.1	5	376.6	381.6	450	36
				10	374.1	384.1	474	
				20	369.1	389.1	520	

the streamwise and spanwise directions and the grid is stretched in the wall-normal direction with a hyperbolic tangent law. To guarantee feasibility of the simulations on the finest grid and the highest temperature difference considered, where the time step is acoustically limited to $\Delta t = 1.4\times10^{-8}$, the bulk velocity has been set for all cases to the relatively high value (for typical heat transfer applications) of $U_b = 36$ m/s corresponding to a Mach number in the low-subsonic range of $M_b = 0.26$ with a range of turbulent Mach number, $M_t = 0.015$ (center region) ~ 0.051 (near-wall peak). Given the large density variation near the pseudoboiling point, buoyancy effects may be important in the mean as well as in the turbulent quantities. In this study, buoyancy effects are neglected in order to focus on structural changes in compressible channel flow turbulence due to wall heat transfer in the presence of real fluid effects.

A reference ideal gas (IG) simulation is carried out with the following nondimensional parameters: $\rho_{b,*}^{(IG)} = 1.0$, $p_{b,*}^{(IG)} = 0.71$, $T_{bot,*}^{(IG)} = 0.8$, $T_{top,*}^{(IG)} = 1.2$, $\Delta T_*^{(IG)} = 0.4$, $U_{b,*}^{(IG)} = M_b = 0.26$, $Pr = 0.7$, $Re_\tau = 367$, and box size of 8×2×4. The subscript "$*$" indicates nondimensional quantities scaled with the bulk density and speed of sound based on the centerplane temperature. Results from the IG reference case are hereafter only presented in dimensional form, rescaled based on the flow parameters of the $\Delta T = 20$ K transcritical case, which read $\rho_{b,20\mathrm{K}} = 520$ kg/m^3, $T_{pb} = 379.1$ K and

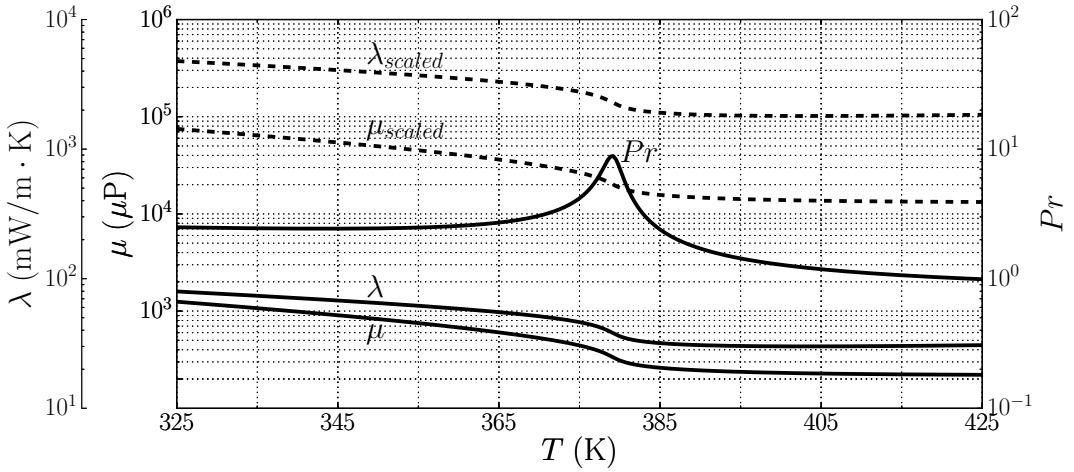

Figure 2.4. Dynamic viscosity, μ, thermal conductivity, λ and Prandtl number Pr for R-134a taken from the Chung's model (——) (see Section §2.2); scaled dynamic viscosity and conductivity (- - -), augmented by a factor of 60, used in the computations, yielding the same Prandtl number.

$U_b = 36$m/s, the last two being common to all cases. The rescaling relations for the IG data therefore read $\rho_b^{(IG)} = \rho_{b,*}^{(IG)} \times \rho_{b,20\mathrm{K}}$, $T^{(IG)} = T_{pb} + (T_*^{(IG)} - 1) \times (20\mathrm{K}/\Delta T_*^{(IG)})$, $U_b^{(IG)} = U_{b,*}^{(IG)} \times (U_b/M_b)$.

To ensure the proper spatial resolution of all relevant hydro- and thermodynamic scales, a systematic grid refinement study has been carried out (see Section §4.2.3 and Table 4.4); this is especially important in simulations of supercritical flows in near-critical or pseudophase transitioning conditions. The relevant metric of the degree of spectral broadening for channel flow turbulence is the friction Reynolds number,

$$Re_\tau = \frac{u_\tau h}{\nu_w} \tag{2.36}$$

based on the friction velocity, u_τ, the channel half-height, h, and the kinematic viscosity at the wall ν_w of the fluid. It can be viewed as the channel half-height normalized by the viscous length scale, $\nu_w/u_\tau = \nu_w/\left(\partial u/\partial x_2\right)_{x_2=0}$, hence $Re_\tau = h^+$. Therefore, Re_τ is the ratio of an integral length scale, $\sim h$, to a viscous scale evaluated at the wall. Typical practice in DNS is to adopt relatively low values of friction

Reynolds number to enable full resolution of the relevant scales. For the present simulations, this is achieved by augmenting dynamic viscosity and thermal conductivity by the same multiplicative factor (Figure 2.4) resulting in Re_τ in the range of 342–394 (Table 4.4). This choice leaves the Prandtl number unaltered, and reproduces the correct trend of transport properties in the transcritical regime. The IG simulations have been carried out at: $Re_\tau = 462$, $\Delta x^+ = 14.44$, $\Delta y^+ = 0.48$–9.10, $\Delta z^+ = 9.62$ for the bottom wall and $Re_\tau = 271$, $\Delta x^+ = 8.47$, $\Delta y^+ = 0.28$–5.36, $\Delta z^+ = 5.64$ for the top wall.

3 NATURAL CONVECTION PSEUDOBOILING (SETUP A)

3.1 Comparison Between Two-Dimensional and Three-Dimensional Pseudoboiling

In this section, an analysis on flow fields, wall heat flux, and probability distribution functions (PDF) is studied by comparing the two-dimensional pseudoboiling with the three-dimensional one.

3.1.1 Density Field and Wall Heat Flux

As a driving force of natural convection, the density difference is induced by the wall heat flux at the bottom (or hot) and top (or cold) wall. The different temperature condition at the walls shown in Table 2.1 stratifies the distribution of fluid properties and increasing the difference sufficiently leads to a convection phenomenon called the Rayleigh–Bénard convection as shown in Figure 3.1. At the relatively small temperature difference such as $\Delta T = 1$ K and 5 K, the heavy pseudoliquid layer near the top wall is pulled down, while the light pseudogas one near the bottom wall moves upwards by the buoyancy effect. The pseudoliquid plume departed from the top wall is transitted to the pseudogas phase at the bottom wall by the released wall heat flux and vice versa at the top wall. The vertical motion of plumes is interrupted by both the horizontal walls and therefore, a sweeping flow along the walls occurs continuously so that global recirculation zones are formed in the two- and three-dimensional pseudoboiling identically. Increasing ΔT results in more accelerated recirculation by the heavier and stronger strikes of pseudoliquid flow onto the bottom wall and the lighter and faster movement of pseudogas plume, namely the decreased characteristic time scale of natural convection process and the active mixing between the bottom and top near-wall fluid. The Rayleigh number, defined as $Ra = g\alpha_p \Delta T (2h)^3 \rho^2 c_p / \mu\lambda$

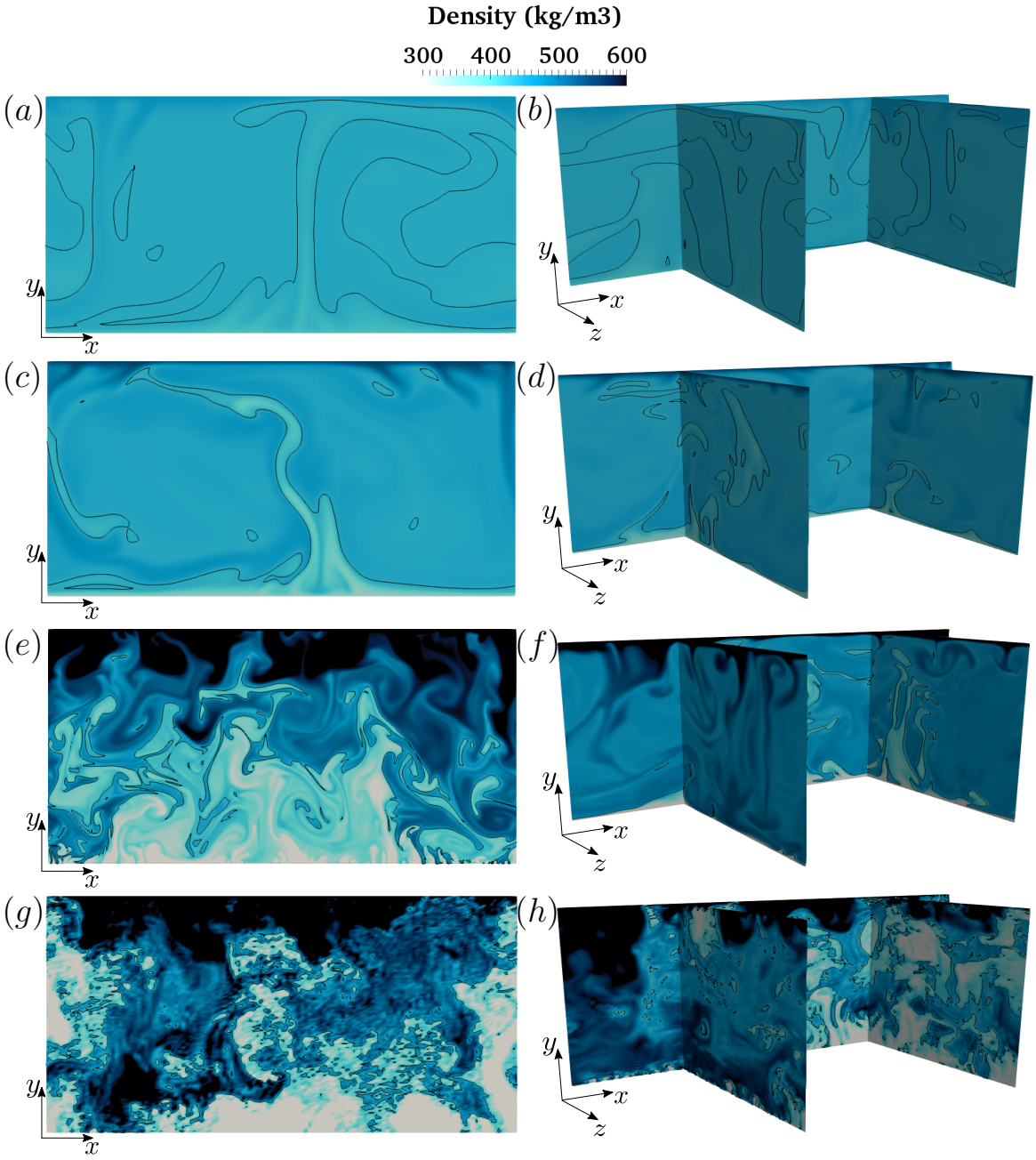

Figure 3.1. Density contours of the two (left)- and three (right)-dimensional pseudoboiling for carbon dioxide at $p_b = 1.1p_{cr}$ and ΔT = 1 K ((*a*), (*b*)), 5 K ((*c*), (*d*)), 20 K ((*e*), (*f*)), and 40 K ((*g*), (*h*)). Isoline in black indicates the pseudoboiling interface at ρ_{pb} = 433 kg/m^3.

where h is the channel half-width, is dependent on the temperature difference between the walls and more local convective rolls and turbulent effect are observed as the ΔT condition increases, without transition boiling which is one of typical pool boiling stages, because of surface tension approaching zero in supercritical fluids (see the two-dimensional pseudoboiling cases at $\Delta T = 20$ K and 40 K in Figure 3.1). Such local phenomena cause the breakup of global recirculation and strengthen the thermal energy transfer. However, comparing to the two-dimensional pseudoboiling, the three-dimensional case at $\Delta T = 20$ K enables to keep the global motion relatively due to the momentum diffusion by the fluid flow along the z direction.

In order to compare and analyze the fluctuating energy intensity and the characteristic time scale of natural convection pseudoboiling in the two- and three-dimensional simulations, energy spectra of fluctuating heat flux at both walls are shown in Figures 3.2 and 3.3 (Here, Hann function is used as the window function to minimize spectral leakage which might be caused by discontinuity in the period of original signal before the discrete Fourier transform). As expected, the fluctuating intensity increases in both the two- and three-dimensional simulations for all the fluids with ΔT. Also, the energy spectra decays at higher frequency as ΔT increases meaning that the period of primary energy-containing motion shortens. However, the two-dimensional case for carbon dioxide at $\Delta T = 20$ K shows anomalous behavior compared to the other cases. Its fluctuating intensity at both walls exceeds the case at $\Delta T = 40$ K, expecially at the top wall, and does not decay much at high frequency in contrast with R-134a and methanol at $\Delta T = 20$ K. Flow fields transitional with physical time give insight into such behavior (Figure 3.4). As time goes on, initial convection cells (also known as Bénard cells) from both walls penetrate the recirculation zone and shear force between the pseudoliquid and pseudogas results in locally small circulations. The pseudoliquid flow exhibits a mode change in an even number (10 at $t = 0.35$ s, 6 at $t = 0.37$ s, and 4 at $t = 0.47$ s) and eventually, the flow field is halved (top-half pseudoliquid and bottom-half pseudogas) retaining 4 mode as observed at $t = 0.52$

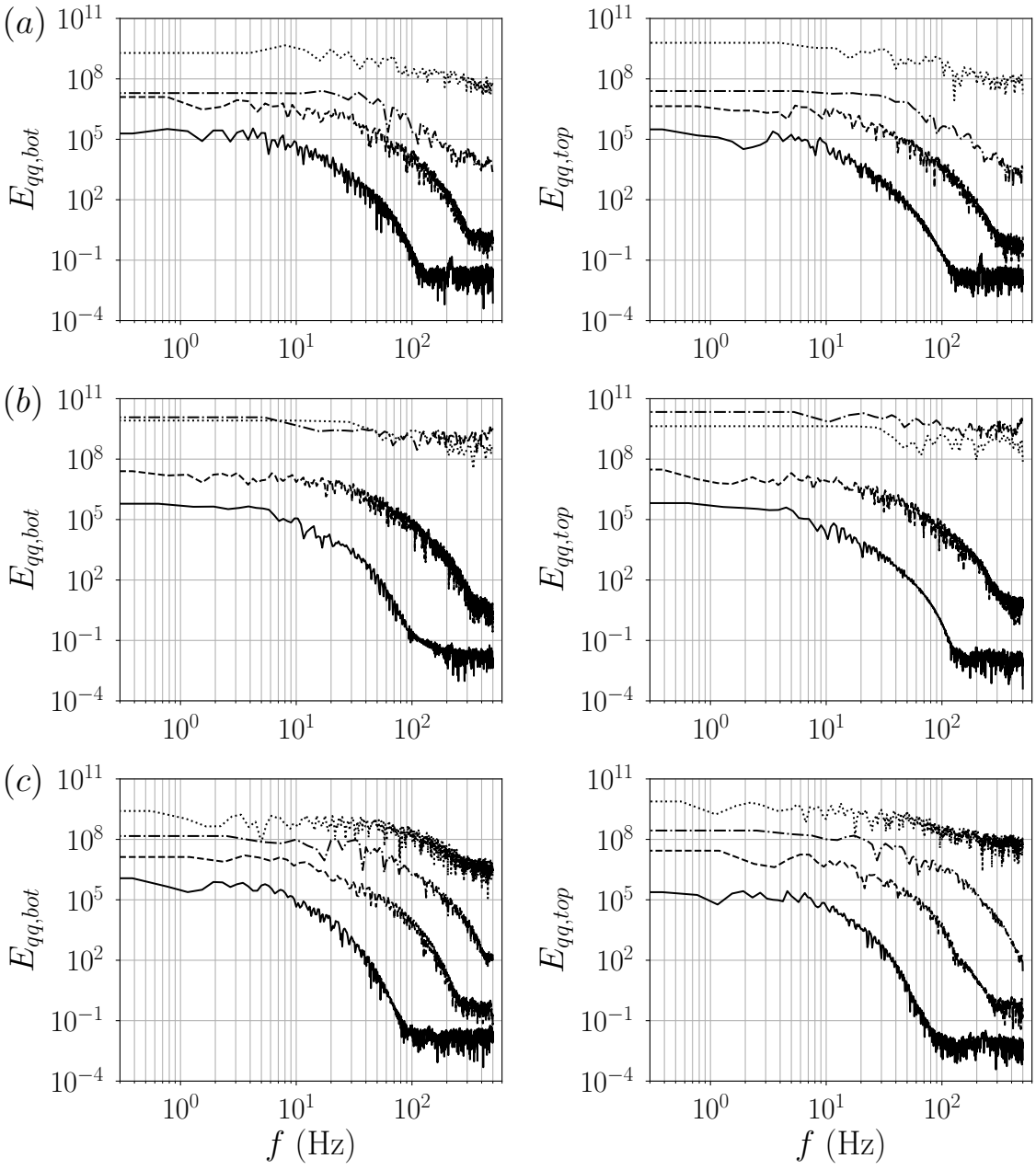

Figure 3.2. Energy spectra of fluctuating heat flux at the bottom (left) and top (right) wall of the two-dimensional pseudoboiling of R-134a (a), carbon dioxide (b), and methanol (c) at $p_b = 1.1p_{cr}$ and ΔT = 1 K (——), 5 K (- - -), 20 K (- · -), and 40 K (· · ·).

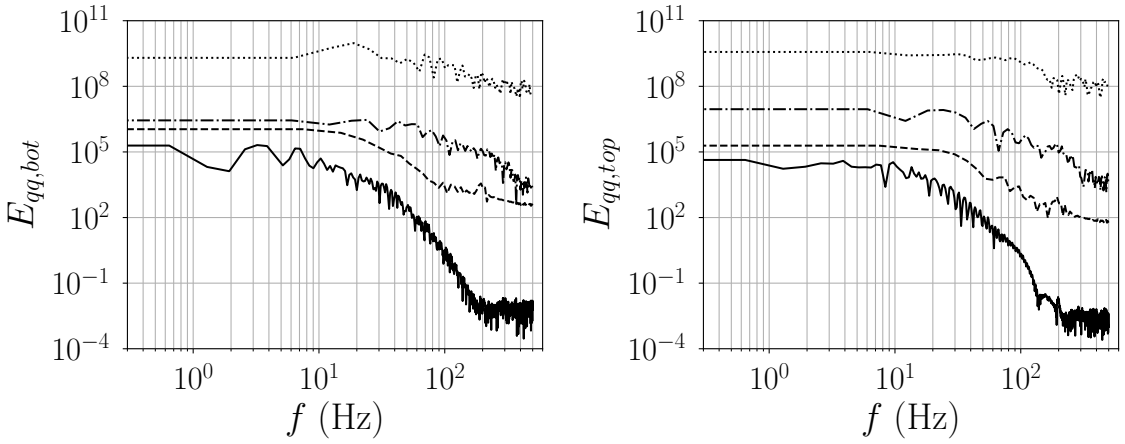

Figure 3.3. Energy spectra of fluctuating heat flux at the bottom (left) and top (right) wall of the three-dimensional pseudoboiling of carbon dioxide at $p_b = 1.1p_{cr}$ and $\Delta T = 1$ K (——), 5 K (- - -), 20 K (- · -), and 40 K (· · ·).

s. This phenomenon is observed only in the two-dimensional simulation for carbon dioxide which might affect the heat transfer characteristics.

Since the thermodynamic properties change rapidly across the PBL (represented as a solid isoline in black in Figure 3.1), the temperature gradient, which affects density and wall heat flux dominantly, is maximum at the line so that the heat transfer is concentrated in the region between the wall and the PBL (called a thermal conductive sublayer later). Accordingly, equivalent wall heat flux can be read as

$$\begin{aligned} q_{w,eq} &= \frac{|q_{w,bot}| + |q_{w,top}|}{2} \\ &\simeq \frac{\left[\left(\lambda_{w,bot}\frac{T_{w,bot}-T_{pb}}{\delta_{\lambda,bot}}\right) + \left(\lambda_{w,top}\frac{T_{pb}-T_{w,top}}{\delta_{\lambda,top}}\right)\right]}{2} \\ &\simeq \left(\frac{\lambda_{w,bot}}{\delta_{\lambda,bot}} + \frac{\lambda_{w,top}}{\delta_{\lambda,top}}\right)\frac{\Delta T}{4} \end{aligned} \tag{3.1}$$

where δ_λ is a thickness of the thermal conductive sublayer determined by a distance from the wall where the root-mean-square of temperature fluctuation is maximum

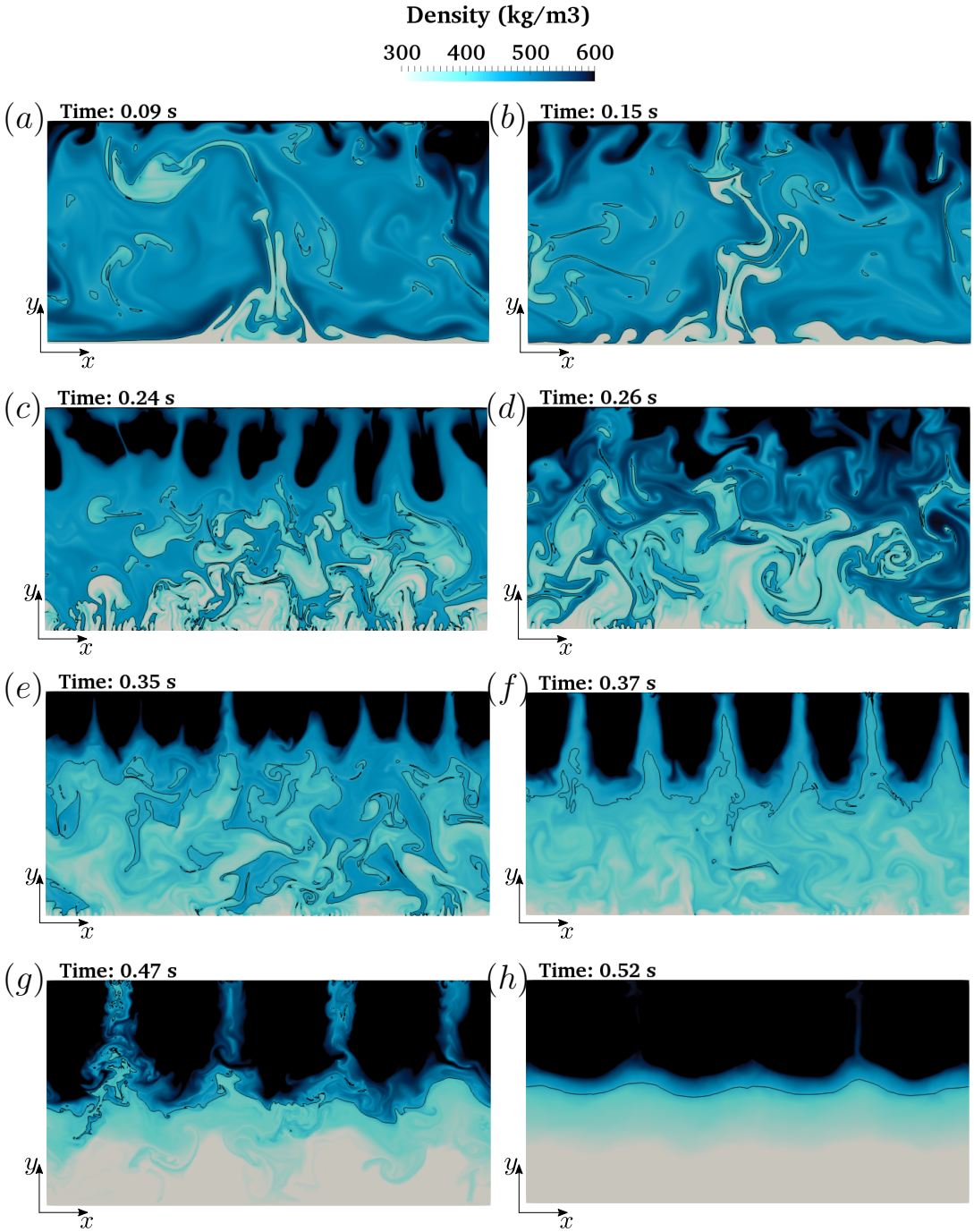

Figure 3.4. Density contours of the two-dimensional pseudoboiling for carbon dioxide at $p_b = 1.1p_{cr}$ and $\Delta T = 20$ K ($t = 0.09$ s (a), 0.15 s (b), 0.24 s (c), 0.26 s (d), 0.35 s (e), 0.37 s (f), 0.47 s (g), and 0.52 s (h)). Isoline in black indicates the pseudoboiling interface at $\rho_{pb} = 433$ kg/m^3.

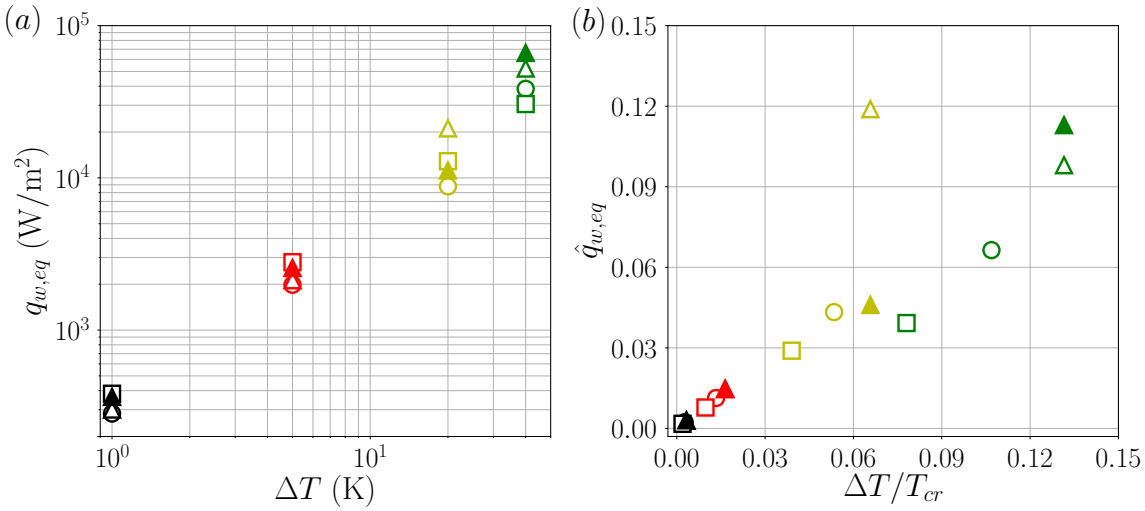

Figure 3.5. Nonscaled (a) and scaled (b) equivalent wall heat flux of the two (open symbol)- and three (closed symbol)-dimensional pseudoboiling of R-134a (○), carbon dioxide (△), and methanol (□) at $p_b = 1.1p_{cr}$ and ΔT = 1 K (black), 5 K (red), 20 K (yellow), and 40 K (green).

and the subcripts 'w' and 'eq' indicate wall and equivalent quantities. Reorganizing Equation (3.1) yields

$$\Delta T \simeq \frac{4q_{w,eq}}{\frac{\lambda_{w,bot}}{\delta_{\lambda,bot}} + \frac{\lambda_{w,top}}{\delta_{\lambda,top}}} \tag{3.2}$$

If ΔT is scaled by T_{cr} and then it is represented by $\hat{q}_{w,eq}$, the scaled equivalent wall heat flux reads

$$\hat{q}_{w,eq} = \frac{\Delta T}{T_{cr}} \simeq \frac{4q_{w,eq}}{T_{cr}\left(\frac{\lambda_{w,bot}}{\delta_{\lambda,bot}} + \frac{\lambda_{w,top}}{\delta_{\lambda,top}}\right)} \tag{3.3}$$

The equivalent wall heat flux using thermodynamic properties averaged on the xz plane (along the x direction for the two-dimensional cases) and its scaled quantity at the different ΔT conditions for R-134a, carbon dioxide, and methanol are shown in Figure 3.5. Except for the two-dimensional case of carbon dioxide at ΔT = 20 K, the equivalent wall heat flux increases monotonically (in a logarithmic scale) as ΔT increases for all the fluids and the three-dimensional carbon dioxide case exhibits

higher heat flux compared to the two-dimensional one. From the viewpoint of the fluid type, heat flux of methanol keeps the highest value until $\Delta T = 20$ K, whereas carbon dioxide surpasses at $\Delta T = 40$ K. The distribution of scaled equivalent wall heat flux shows good agreement, and hence meaning that the scaling by Equation (3.3) is proper in this natural convection pseudoboiling. However, the two-dimensional carbon dioxide simulation at $\Delta T = 20$ K does not follow the equation and show the exceptional high value due to its high heat flux in the nonscaled equivalent wall heat flux and broadened thermal conductive sublayer observed in Figure 3.4(h) (recall that δ_λ is included in Equation (3.3)).

3.1.2 Heat Transfer Correlation

While various heat transfer correlation models have been proposed for forced/natural convection circulation systems in supercritical fluids, one for the present type of natural convection pseudoboiling has not been studied thoroughly. In order to investigate the heat transfer correlation in natural convection, considering the buoyancy effect is essential so that the Nusselt number is represented as a function of the Rayleigh number (or the product of the Grashof number and the Prandtl number, $GrPr$) [31]. Also, recent studies on supercritical forced convection by Bae & Kim [28] and Mokry *et al.* [29] included the density-induced effect in their correlation model. In this study, transport properties are considered as well as density, since dynamic viscosity and thermal conductivity affect the thermodynamic behavior significantly in the transcritical temperature regime and consequently, the heat transfer correlation reads

$$\overline{Nu} = a\overline{Gr}^{b}\overline{Pr}^{c}\left(\frac{\rho_w}{\overline{\rho}}\right)^{d}\left(\frac{\mu_w}{\overline{\mu}}\right)^{e}\left(\frac{\lambda_w}{\overline{\lambda}}\right)^{f} = \left(\overline{GrPr}\right)^{*} \tag{3.4}$$

where a, b, c, d, e, and f are coefficients satisfying the heat transfer characteristics at the bottom and top walls respectively. The mean quantities are evaluated by

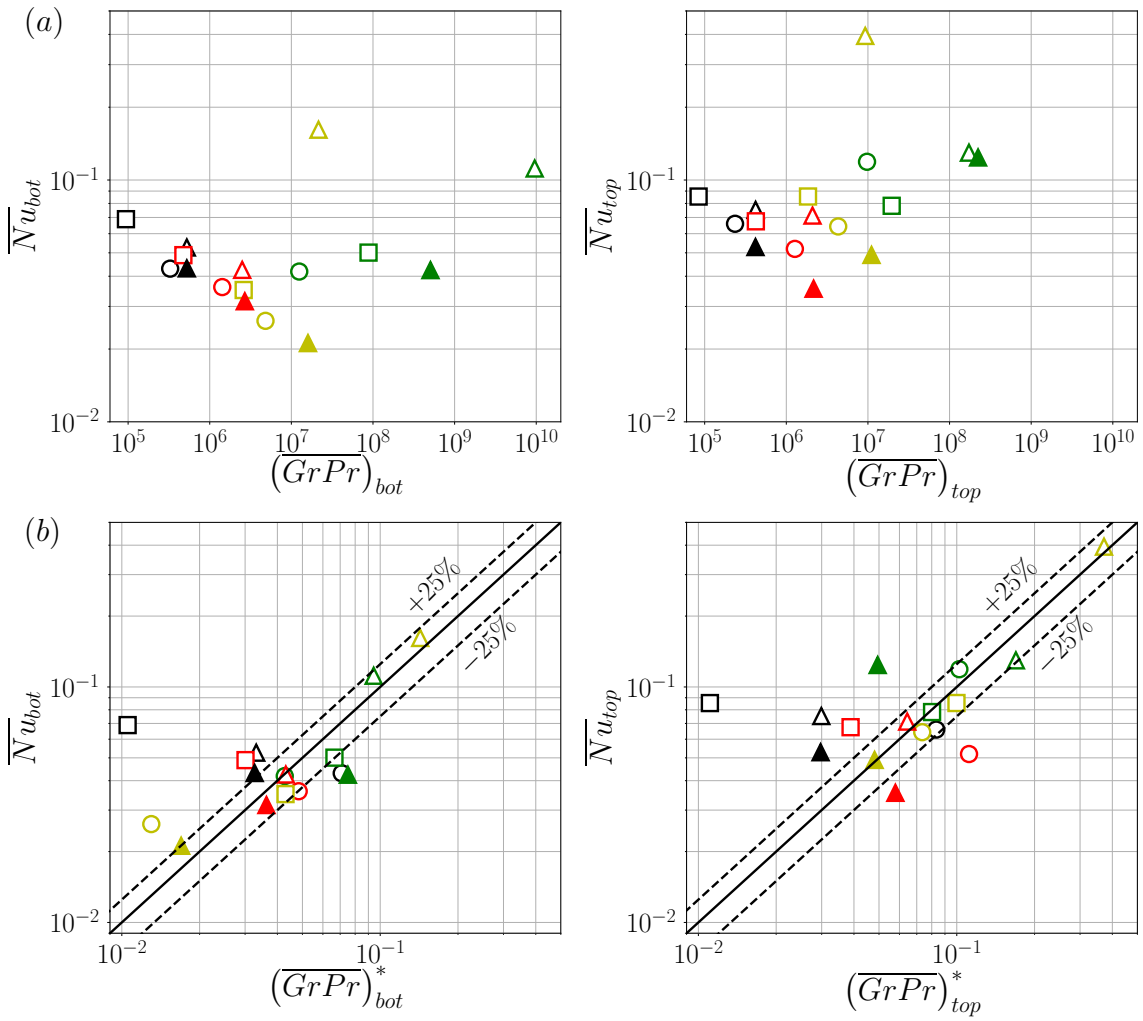

Figure 3.6. Mean Nu versus $GrPr$ (a) and their heat transfer correlation (b) at the bottom (left) and top (right) wall of the two (open symbol)- and three (closed symbol)-dimensional pseudoboiling of R-134a (○), carbon dioxide (△), and methanol (□) at $p_b = 1.1p_{cr}$ and $\Delta T = 1$ K (black), 5 K (red), 20 K (yellow), and 40 K (green).

$\overline{Q} = \int_0^h Q(y)dy/h$ where Q is an arbitrary quantity. The local Nusselt, Grashof, and Prandtl numbers are defined as

$$Nu(y) = \frac{q(y)y}{(T_w - T_b)\lambda(y)} \tag{3.5}$$

$$Gr(y) = \frac{g\alpha_p(y)(T_w - T_b)y^3\rho(y)^2}{\mu(y)^2} \tag{3.6}$$

Table 3.1. Coefficients for the heat transfer correlation at the bottom and top wall.

	a	b	c	d	e	f
Bot	8.273×10^{-4}	8.811×10^{-1}	-1.871	-1.709	2.673×10^{1}	-1.436×10^{1}
Top	2.734×10^{-2}	7.353×10^{-1}	-2.679	-3.897	-1.199×10^{1}	1.216×10^{1}

$$Pr(y) = \frac{c_p(y)\mu(y)}{\lambda(y)} \tag{3.7}$$

where T_b is the surrounding bulk flow temperature, $T_b = \int_A \rho v c_p T dA / \int_A \rho v c_p dA$.

In Figure 3.6, the values of $\overline{GrPr}$ (or $\overline{Ra}$) for all the fluids are scattered in a significantly wide range ($10^5 \sim 10^{10}$ at the bottom wall and $10^5 \sim 2 \times 10^8$ at the top wall, approximately), especially at the bottom wall where the pseudogas phase is dominant. Such a wide distribution clusters by using Equation (3.4) with the coefficients, a–f, proposed by nonlinear least squares curve fitting (see Table 3.1) and the model shows good agreement with $\overline{Nu}$ at both walls, although several data deviate from the ±25% reference lines.

3.1.3 Probability Distribution Functions

Figure 3.7 presents the PDF of the two- and three-dimensional cases for carbon dioxide conditional to a density range centered about its PBP. At $\Delta T = 1$ K, both the two- and three-dimensional simulations show a flat distribution meaning that the pseudotransition occurs in most of the region between the walls since the ΔT range is very narrow. As ΔT increases, while the two-dimensional case exhibits the center-dominant pseudotransition ($y \simeq 0$, namely the plume-based transition), the three-dimensional one inclines towards the top wall and it forms two peaks near the walls at $\Delta T = 20$ K. Those two peaks imply the active near-wall heat transfer. Such trend is broken at $\Delta T = 40$ K having a bottom wall inclined distribution which results in its distortion, yet not the near-wall region. This breakup occurs at the lower ΔT

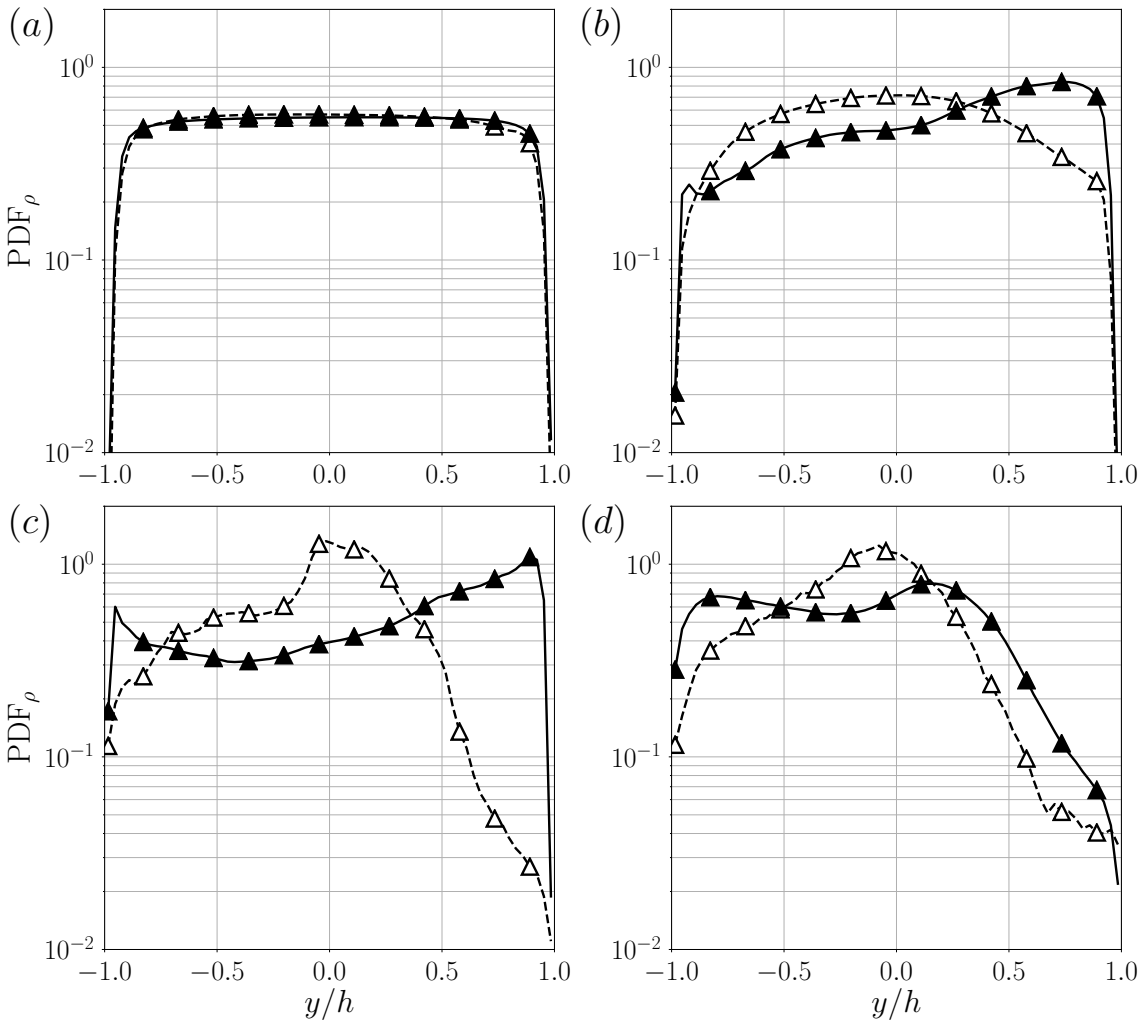

Figure 3.7. Conditional PDF of y/h values of the two (- - -, △)- and three (——, ▲)-dimensional pseudoboiling of carbon dioxide at $p_b = 1.1p_{cr}$ and $\Delta T = 1$ K (a), 5 K (b), 20 K (c), and 40 K (d). The PDF is extracted in the conditional density range of $|\rho - \rho_{pb}| \leq 6.6$ kg/m^3 where $\rho_{pb} = 432.8$ kg/m^3 corresponding to $T_{pb} \pm 0.1$ K.

condition ($\Delta T = 20$ K) in the two-dimensional case which proves the phenomena observed in Figure 3.1.

3.2 Turbulent Statistics

In this section, a statistical analysis on the mean and fluctuation quantities and energy spectra is carried out for the three-dimensional pseudoboiling of carbon dioxide.

3.2.1 Semi-Local Scaled Mean and Fluctuating Quantities

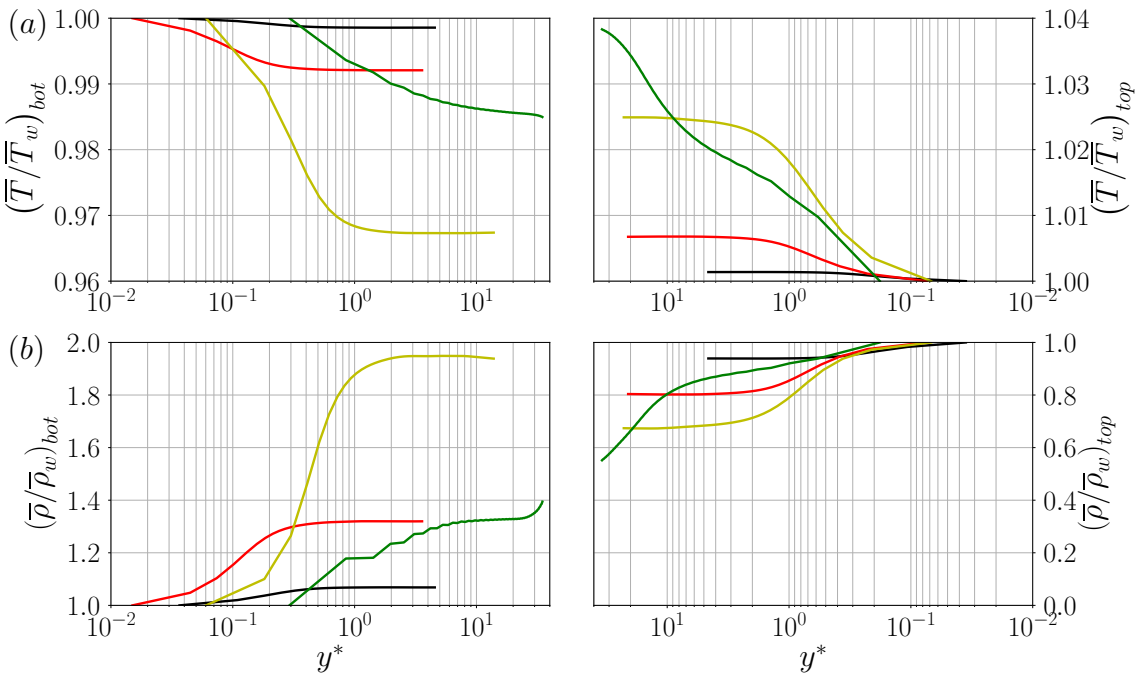

Figure 3.8. Reynolds-averaged temperature (a) and density (b) scaled by the wall quantity at the bottom (left) and top (right) wall of the three-dimensional pseudoboiling for carbon dioxide at $p_b = 1.1p_{cr}$ and ΔT = 1 K (black), 5 K (red), 20 K (yellow), and 40 K (green). A semi-local scaling factor for y is shown in Table B.1 in Appendix B.

Reynolds-averaged temperature and density profiles in the bottom and top near-wall region are shown in Figure 3.8. The profiles are scaled by each wall quantities and the wall-normal distance, y, is done semi-locally by $\delta_v^* = \overline{\mu}(y)/(\overline{\rho}(y)\overline{u}_\tau^*(y))$ where $\overline{u}_\tau^*(y) = \sqrt{\overline{\tau}_w/\overline{\rho}(y)}$ using local quantities (see Table B.1 for the semi-local scaling

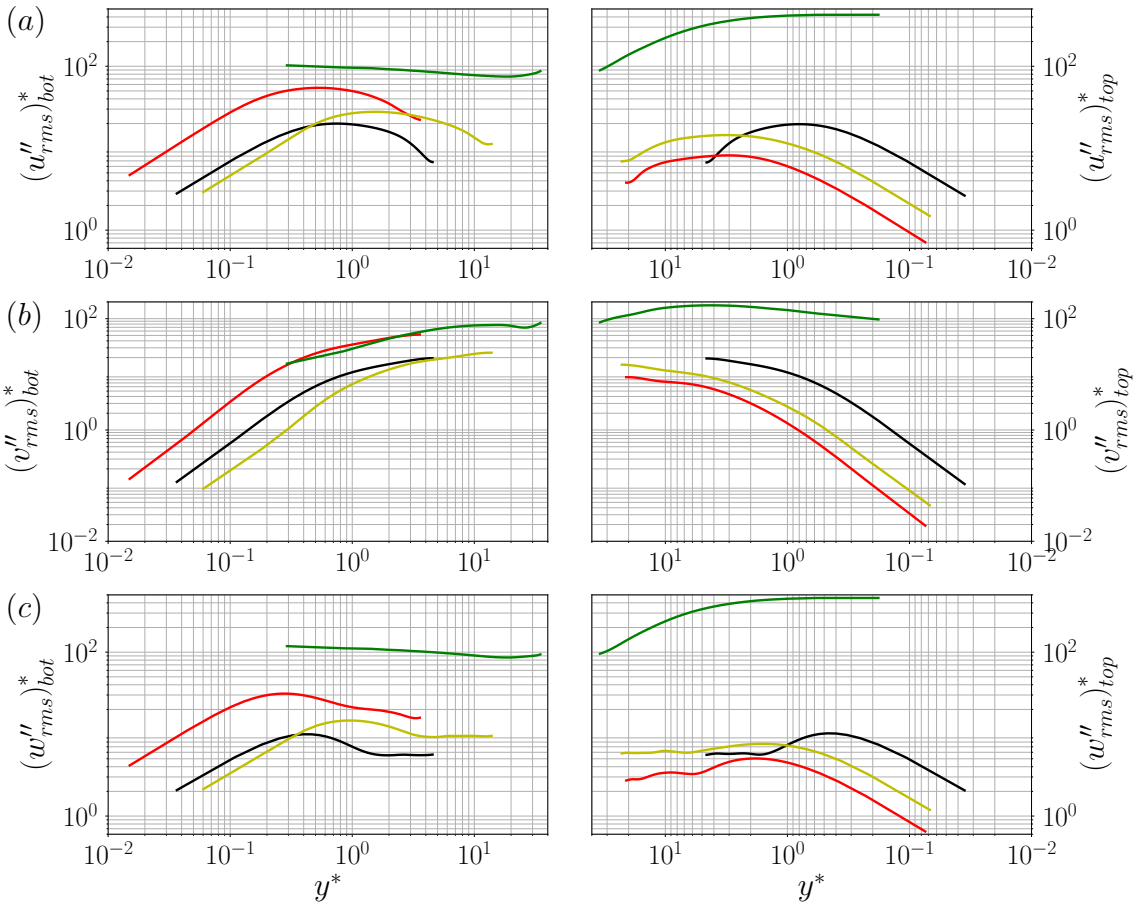

Figure 3.9. Semi-local scaled root-mean-square of Favre fluctuating velocity component in the x (a), y (b), and z (c) direction at the bottom (left) and top (right) wall of the three-dimensional pseudoboiling for carbon dioxide at $p_b = 1.1p_{cr}$ and $\Delta T = 1$ K (black), 5 K (red), 20 K (yellow), and 40 K (green). Semi-local scaling factors are shown in Table B.1 in Appendix B.

factors) [60] (discussed in more detail in Section §4.2). As ΔT increases, large density gradient is observed near the walls which follows the temperature profiles except for $\Delta T = 40$ K. Although the $\Delta T = 40$ K case reflects well the breakup of recirculation zone shown in Figure 3.1, its profile, especially in the bottom wall region (pseudogas phase), wiggles meaning that the thermodynamic length scale is not fully resolved in the present grid resolution (Table 2.3). The real fluid effects induce the rapid density change by small temperature of variation across the channel (the ratio of maximum

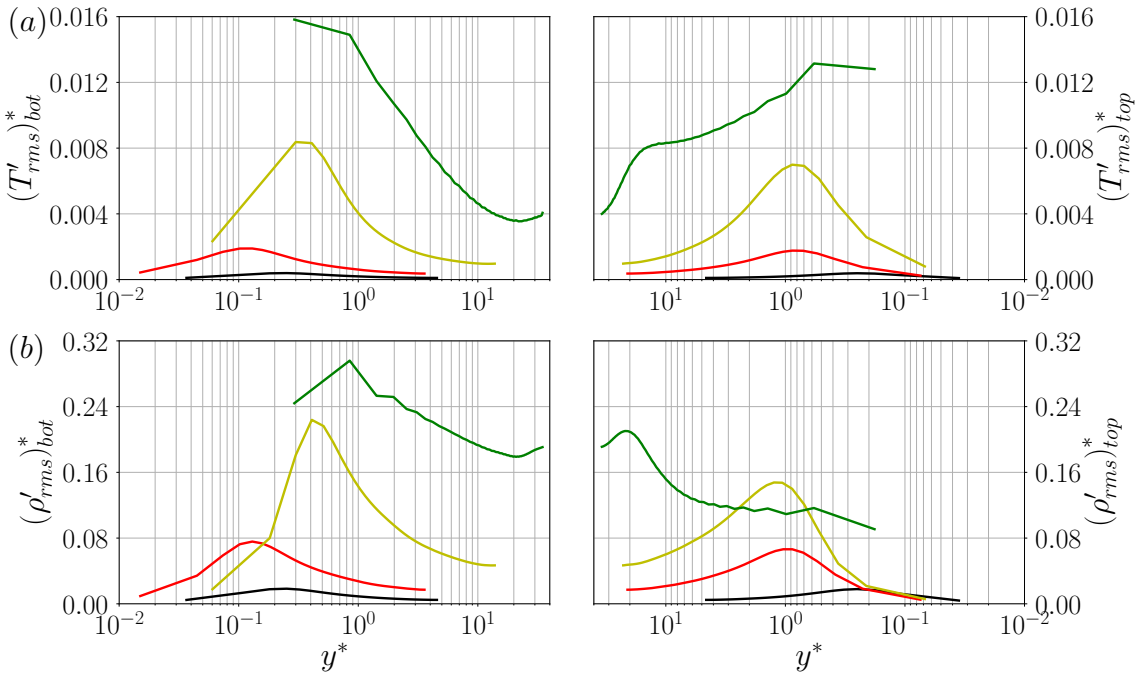

Figure 3.10. Semi-local scaled root-mean-square of Reynolds fluctuating temperature (a) and density (b) at the bottom (left) and top (right) wall of the three-dimensional pseudoboiling for carbon dioxide at $p_b = 1.1p_{cr}$ and $\Delta T = 1$ K (black), 5 K (red), 20 K (yellow), and 40 K (green). Semi-local scaling factors are shown in Table B.1 in Appendix B.

rate of change in the bottom wall region at $\Delta T = 20$ K, $\Delta\left(\overline{T}/\overline{T}_w\right)_{bot} : \Delta\left(\overline{\rho}/\overline{\rho}_w\right)_{bot} = 1 : 28.758$). Also, in spite of high performance of the semi-local scaling in terms of collapsing the profiles [61–63], it does not show good agreement in this transcritical temperature regime at supercritical pressure.

Figures 3.9 and 3.10 present the semi-local scaled root-mean-square (rms) profiles of fluctuating hydro- and thermodynamic quantities. For three ΔT conditions, 1 K, 5 K, and 20 K, the y^* coordinates of peaks for the x and z velocity components, temperature, and density are located at which the gradient of mean quantities shown in Figure 3.8 is maximum, namely occurring the pseudophase change (based on the wall unit, y^*, the peak moves towards the channel centerplane in order of $\Delta T = 5$ K $\rightarrow$ 1 K $\rightarrow$ 20 K in the bottom near-wall region and 1 K $\rightarrow$ 5 K $\rightarrow$ 20 K in the

top near-wall region). The y velocity component does not show the peak, however, it becomes maximum on the centerplane. The fluctuation of all the velocity components increases in order of $\Delta T = 1$ K $\rightarrow$ 20 K $\rightarrow$ 5 K in the bottom wall region and vice versa in the top wall region. On the other hand, The fluctuation intensity of density and temperature increases with ΔT.

3.2.2 Turbulent Structures and Energy Spectra

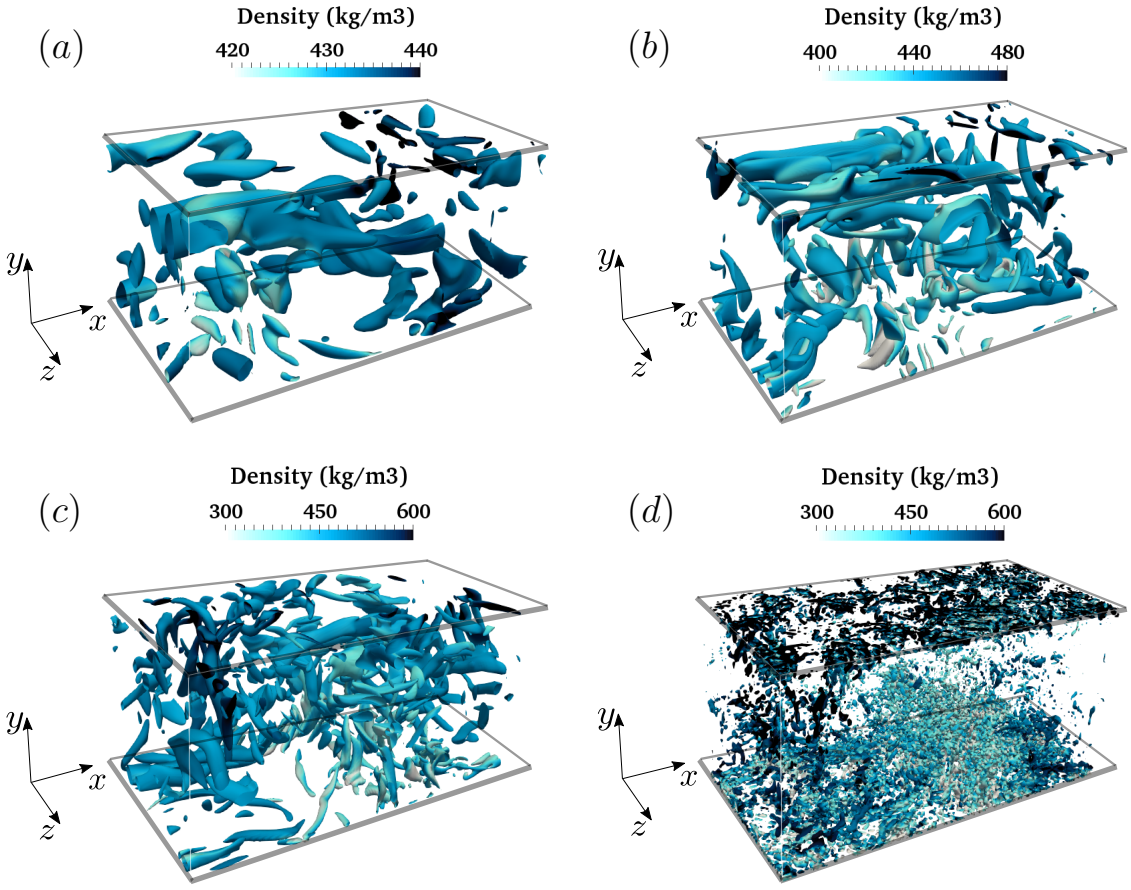

Figure 3.11. Q-criterion isosurfaces of the three-dimensional pseudoboiling for carbon dioxide at $p_b = 1.1p_{cr}$ and $\Delta T = 1$ K ($Q = 6\times10^2$ 1/s^2) (a), 5 K ($Q = 5\times10^3$ 1/s^2) (b), 20 K ($Q = 3\times10^4$ 1/s^2) (c), and 40 K ($Q = 7\times10^5$ 1/s^2) (d). The isosurfaces are colored by density.

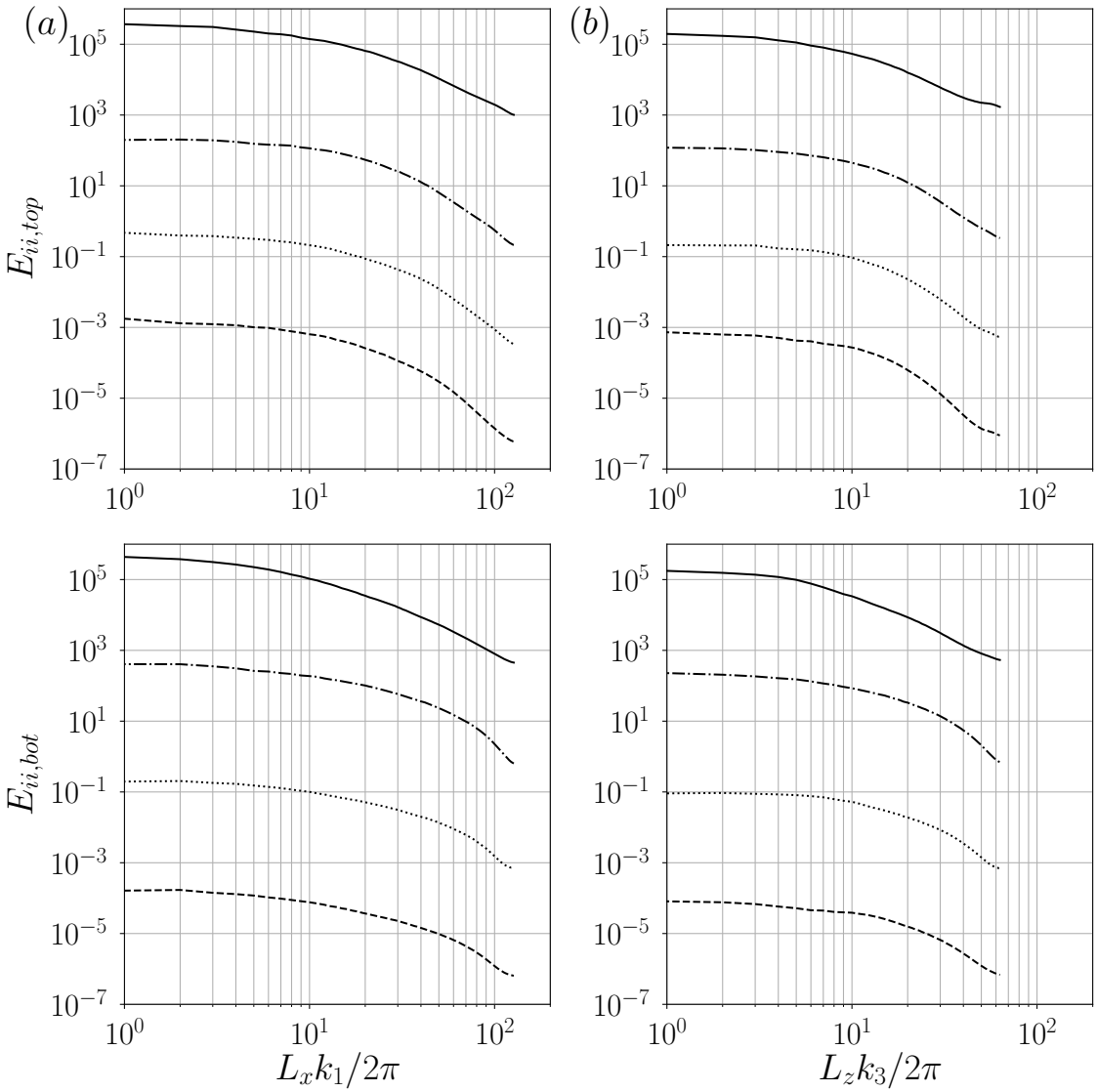

Figure 3.12. One-dimensional energy spectra of Reynolds averaged fluctuating density ($E_{\rho\rho}$, ——), wall-normal velocity (E_{vv}, - - -), and temperature (E_{TT}, - · -) and one-dimensional cospectra between the Reynolds averaged fluctuating wall-normal velocity and temperature (E_{vT}, · · ·) in the x (a) and z (b) direction extracted at the top and bottom near-wall peak of temperature fluctuation intensity of the three-dimensional pseudoboiling for carbon dioxide at $p_b = 1.1p_{cr}$ and $\Delta T = 20$ K.

In order to investigate the turbulent structures (identification of vortices), the isosurfaces of Q-criterion are presented in Figure 3.11. As ΔT increases, the rotational motion is split into smaller vortex structures which accelerate the strong local circulation in the channel as shown in Figure 3.1. However, the $\Delta T = 40$ K case has a numerical error due to the unresolved turbulence/thermal length scales which require finer grid resolution than the present one.

Figure 3.12 shows one-dimensional energy spectra of fluctuating density, wall-normal velocity, and temperature and cospectra between fluctuating wall-normal velocity and temperature extracted at both temperature rms peaks for the $\Delta T = 20$ K case showing the physical turbulent statistics. Decaying rapidly of the energy spectra at high wave numbers implies the suitability of the grid resolution for $\Delta T = 20$ K. As expected, all the spectra in both wall regions are higher in the x direction than the z direction since the primary motion of flow is in the x and y direction.

4 TURBULENT FORCED CONVECTION (SETUP B)

The contents of this chapter were published in the Journal of Fluid Mechanics, titled "Pseudophase Change Effects in Turbulent Channel Flow under Transcritical Temperature Conditions."

4.1 Wall-Bounded Turbulent Flow and Real Fluid Effects

Transcritical temperature conditions at supercritical pressure have been found to enhance heat transfer fluctuations and alter turbulence production rates in wall-bounded flows [4]. Such deviations from ideal gas behavior are not to be confused with real fluid effects, which refers to molecularly disassociated gases occurring in hypersonic flows. Real fluid effects in a flat-plate turbulent boundary layer (TBL) over a heated wall were studied by Kawai [64]; he found that the Morkovin's hypothesis [65] is not applicable in pseudophase changing conditions due to the presence of significant density fluctuations yielding nonclassical effects in the mass flux, turbulent diffusion, and pressure dilatation distributions. Patel *et al.* [62] numerically and theoretically investigated the near-wall scaling laws in a turbulent channel flow with large thermophysical property variations. They confirmed that the turbulent flow statistics exhibit quasi-similarity based on a semi-local friction Reynolds number, $Re_\tau^* \equiv Re_\tau \sqrt{(\bar{\rho}/\bar{\rho}_w)}/\,(\bar{\mu}/\bar{\mu}_w)$, where the overbar refers to the Reynolds averaging and the subscript w to the averaged wall quantity. Their investigation was, however, limited to a density ratio of $\bar{\rho}/\bar{\rho}_w = 0.4$ to 1.0. From direct numerical simulations (DNS) of a dense gas, supersonic turbulent channel flows by Sciacovelli *et al.* [63], it was investigated that the transport properties are dependent on density and temperature of the fluid and the speed of sound varies nonmonotonically due to dense gas effects (or real fluid effects in this study). The dense gas effects caused that max-

imum levels of the fluctuating density root-mean-square are located in the viscous sublayer which is different from the ideal gas case locating in the buffer layer so that the density fluctuations do not change the turbulent structures significantly in the channel and the Morkovin's hypothesis holds. Nemati *et al.* [66] performed DNS of a heated turbulent pipe flow at supercritical pressure, where thermal expansion due to a constant wall heat flux in the presence of low buoyancy effects was found to attenuate turbulent kinetic energy (TKE); turbulence enhancement was observed for high buoyancy cases. Pizzarelli *et al.* [67] studied turbulent rectangular channel flow at supercritical pressure with high wall heat flux, finding that real fluid effects attenuate heat transfer significantly at the channel corners. Compressible channel flow simulations at supercritical pressures and transcritical temperatures by Sengupta *et al.* [68] show that the cold wall region has higher density and temperature fluctuations as well as higher coherence than the hot near-wall region. Also, the liquid-like flow region is characterized by decreased streamwise and increased spanwise anisotropy and vice versa in the region of gas-like behavior.

4.2 First and Second Order Statistics

In this section, a statistical analysis limited to first and second-order moments of turbulent fluctuations in the transcritical channel flow setup of Figure 2.2 is carried out in comparison with the IG simulations.

4.2.1 Mean Flow Quantities

Figure 4.1 shows Reynolds-averaged profiles of density, temperature, and compressibility factor,

$$Z = \frac{p}{\rho\, R_{gas}\, T} \tag{4.1}$$

where $R_{gas} = 81.49$ J/kg K is the gas constant for R-134a. The top-to-bottom density difference (Table 4.1) of $\Delta\rho = 447.5$ kg/m^3 achieved under transcritical conditions for $\Delta T = 20$ K is more than twice the IG value of $\Delta\rho_{IG} = 213.5$ kg/m^3 obtained

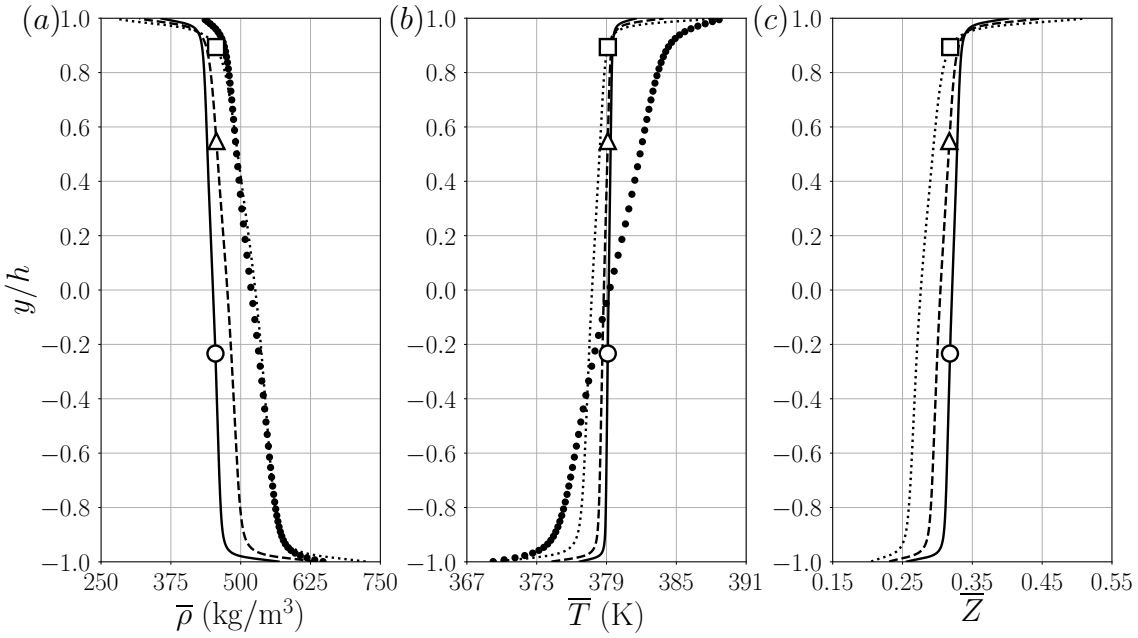

Figure 4.1. Reynolds-averaged density (a), temperature (b), and compressibility factor (c) for $p_b = 1.1p_{cr}$ and $\Delta T = 5$ K (——), 10 K (- - -), and 20 K ($\cdots$) and rescaled ideal gas data (•) (in Section §2.4.2). Average location of pseudotransition for $\Delta T = 5$ K (○), 10 K (△), and 20 K (□).

Table 4.1. Top and bottom-wall values of mean density and compressibility factor and average location of pseudophase transition y_{pb} for various temperature conditions. With the exception of ΔT, all values reported are a result of the calculations. $\Delta\rho_{IG}$ is obtained by rescaling the output of the (dimensionless) reference ideal gas simulation to match the flow settings of the $\Delta T = 20$ K transcritical case (in Section §2.4.2).

ΔT (K)	$\overline{\rho}_{top}$ (kg/m^3)	$\overline{\rho}_{bot}$ (kg/m^3)	$\Delta\rho$ (kg/m^3)	$\Delta\rho_{IG}$ (kg/m^3)	$\overline{Z}_{top}$	$\overline{Z}_{bot}$	y_{pb}
5	358.3	567.7	209.4	–	0.40	0.26	$-0.23h$
10	318.6	635.0	316.4	–	0.45	0.23	$+0.55h$
20	276.1	723.6	447.5	213.5	0.51	0.21	$+0.89h$

for the same ΔT. Departure from the ideal gas behavior is, in fact, present in the entire channel, with $\overline{Z}_{max} \simeq 0.51$ achieved at the top wall in the pseudogaseous layer

for $\Delta T = 20$ K. As ΔT is increased, the average location of pseudotransition y_{pb}, where real fluid effects are expected to be the most accentuated, moves from a near-centerplane location to the upper wall. In all cases, the transition from a seemingly fully thermally mixed region in channel core (i.e. $\overline{T}(y)$ is relatively uniform and close to the pseudoboiling value to a conductive sublayer region at the walls is more defined than in the reference IG simulation. Such steep mean flow gradients sustain significant density and enthalpy fluctuations, up to $\rho_{rms,max} = 44.1$ kg/m^3 and $h_{rms,max} = 8.9$ kJ/kg, respectively (as discussed later in Figures 4.8 and 4.9) for the $\Delta T = 20$ K case. The very high heat capacity of the fluid undergoing pseudophase transition, on the other hand, limits the temperature fluctuations to $T_{rms,max} < 2$ K.

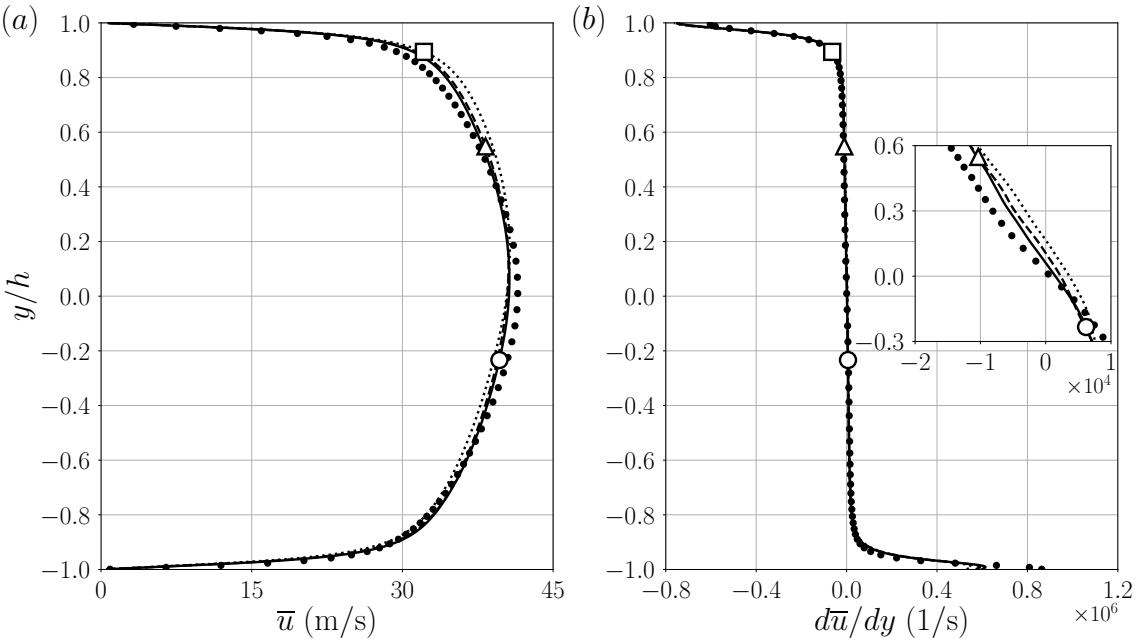

Figure 4.2. Reynolds-averaged streamwise velocity component (a) and its wall-normal gradient (b) for $p_b = 1.1p_{cr}$ and $\Delta T = 5$ K (——), 10 K (- - -), and 20 K ($\cdots$) and rescaled ideal gas data (•) (in Section §2.4.2). Average location of pseudotransition for $\Delta T = 5$ K (○), 10 K (△), and 20 K (□).

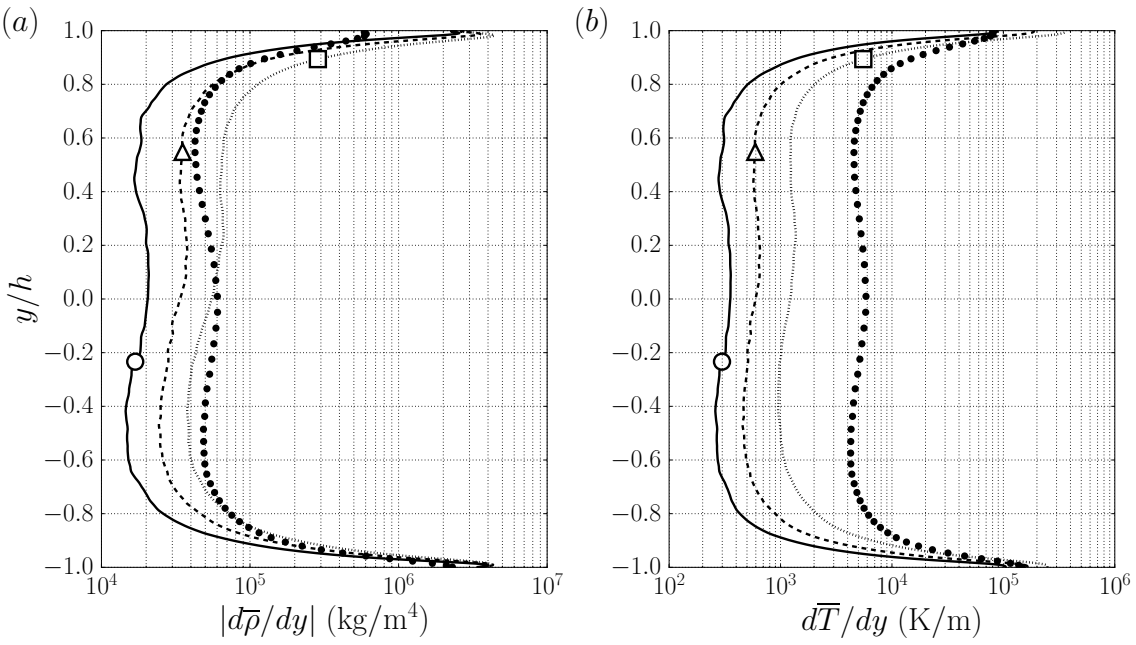

Figure 4.3. Wall-normal gradient of Reynolds-averaged mean density (a) and temperature (b) for $p_b = 1.1p_{cr}$ and $\Delta T = 5$ K (——), 10 K (- - -), and 20 K ($\cdots$) and rescaled ideal gas data (•) (in Section §2.4.2). Average location of pseudotransition for $\Delta T = 5$ K (○), 10 K (△), and 20 K (□).

The mean turbulent streamwise velocity profile (Figure 4.2a) becomes more asymmetric (with a slight acceleration of the pseudogaseous layer) for increasing ΔT, with an upwards shift in the maximum velocity location, $y/h = 0.06$ for $\Delta T = 5$ K, 0.11 for $\Delta T = 10$ K, and 0.17 for $\Delta T = 20$ K (see inset in Figure 4.2b), following the same trend of the pseudotransition location y_{pb}. As a result, a larger velocity gradient magnitude is found near the top wall (the magnitude ratio of top-to-bottom velocity gradient is 1.24 for $\Delta T = 5$ K, 1.32 for $\Delta T = 10$ K, 1.44 for $\Delta T = 20$ K in Figure 4.2b). In Figure 4.3, while top-down asymmetries in the temperature gradient are confined to the sublayer regions, the mean density gradient profile is more visibly affected by the location of pseudotransition. A logarithmic increment of the centerplane of the temperature gradient is observed as ΔT is also increased logarith-

mically (i.e. $d(\Delta T)/\Delta T = \text{const}$), suggesting a linear relation between the overall top-to-bottom equilibrium heat flux and ΔT. The latter is a surprising result given the degree of thermodynamic and hydrodynamic nonlinearity of the problem. These results also suggest that transcritical heat flux rates are amenable to straightforward dimensionless scaling in similar canonical setups. This analysis, however, is out of the scope of the current study. While the velocity gradient increase (decrease) in the pseudogaseous (pseudoliquid) region as ΔT is increased is not as significant as the corresponding variations in density and temperature gradients, real fluid effects are very apparent when attempting to scale the mean velocity profiles with commonly used scaling laws.

For all ΔT values, the mean streamwise velocity profiles are scaled following the recently proposed approach by Trettel & Larsson [69], which accounts for the wall heat transfer effects, with the van Driest transformation [70] and the semi-local scaling [60] (Figure 4.4). The expressions of the three transformations considered are reported here for convenience and completeness.

The van Driest transformation [70] is given by

$$\overline{u}^+_{VD} = \int_0^{\overline{u}^+} \left(\frac{\overline{\rho}(y)}{\overline{\rho}_w}\right)^{\frac{1}{2}} d\overline{u}^+ \tag{4.2}$$

where $\overline{u}^+ = \overline{u}(y)/\overline{u}_\tau$ and the conventional set of scaling parameters reads

$$y^+ = \frac{y}{\delta_v} = \frac{y}{\overline{\mu}_w/(\overline{\rho}_w \overline{u}_\tau)}, \quad \overline{u}_\tau = \sqrt{\overline{\tau}_w/\overline{\rho}_w} \tag{4.3}$$

whereas, for the semi-local scaling [60], it reads

$$y^* = \frac{y}{\delta^*_v} = \frac{y}{\overline{\mu}(y)/(\overline{\rho}(y)\overline{u}^*_\tau(y))}, \quad \overline{u}^*_\tau(y) = \sqrt{\overline{\tau}_w/\overline{\rho}(y)} \tag{4.4}$$

Finally, the transformation by Trettel & Larsson [69] reads

$$\overline{u}^+_{TL} = \int_0^{\overline{u}^+} \left(\frac{\overline{\rho}(y)}{\overline{\rho}_w}\right)^{\frac{1}{2}} \left[1 + \frac{1}{2}\frac{1}{\overline{\rho}(y)}\frac{d\overline{\rho}(y)}{dy}y - \frac{1}{\overline{\mu}(y)}\frac{d\overline{\mu}(y)}{dy}y\right] d\overline{u}^+ \tag{4.5}$$

In the log-law region, the ideal gas results collapse onto the classic incompressible law of the wall with Trettel & Larsson [69]'s transformation, for both top and bottom walls; the widest spread for the ideal gas data is observed with the van Driest transformation plotted against the semi-locally scaled wall-normal coordinate y^*.

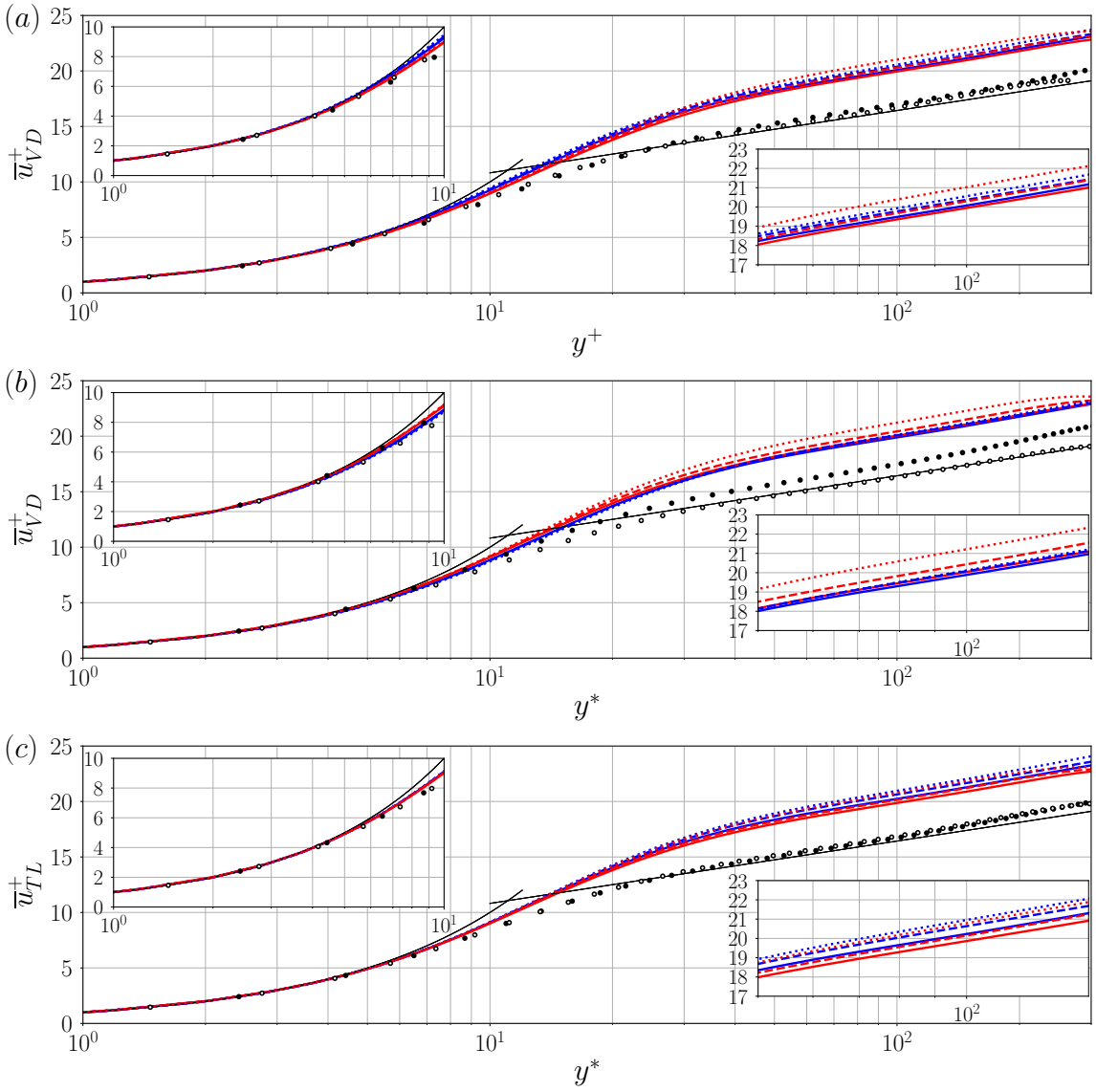

Figure 4.4. Mean streamwise velocity versus wall-normal coordinate in wall units scaled based on the conventional van Driest transformation plotted against wall-normal distance in classic wall units (a) and semi-locally scaled [60] (b), transformed based on Trettel & Larsson [69] (c) for $p_b = 1.1p_{cr}$ and $\Delta T = 5$ K (——, thickened), 10 K (- - -), and 20 K ($\cdots$); reference ideal gas data (circles); bottom wall (blue, •) and top wall (red, ○). Profiles of the law of the wall ($\overline{u}^+ = y^+$ for the viscous sublayer; $\overline{u}^+ = 1/\kappa \ln y^+ + C$ where $\kappa = 0.41$ and $C = 5.2$ for the log-law region) are shown with a thin solid black line for reference.

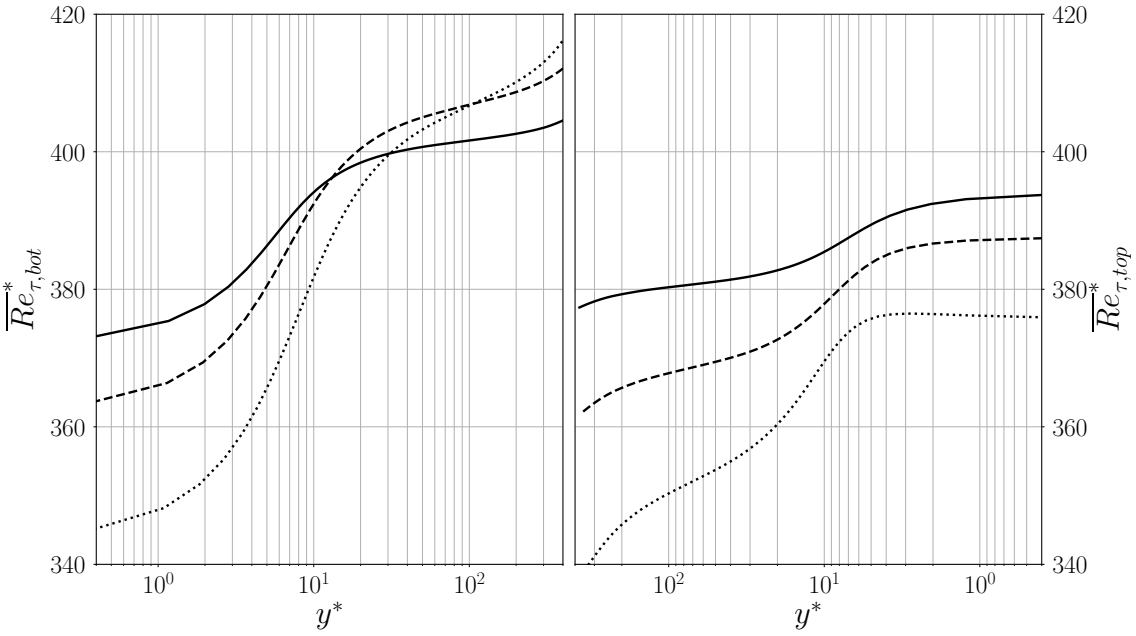

Figure 4.5. Semi-local friction Reynolds number at the bottom (left) and top (right) wall for $p_b = 1.1p_{cr}$ and $\Delta T = 5$ K (——), 10 K (- - -), and 20 K ($\cdots$).

For the transcritical cases, the transformed top and bottom wall streamwise velocity profile results in higher intercepts than the classic incompressible log-law. In recent publications by Ma *et al.* [71], very large values of the transformed velocity $\overline{u}^+_{TL}$ were observed, suggesting inadequacy of this transformation for this flow. This issue is analyzed in more detail in Appendix B also in light of the previous communication [72]. Effects of varying ΔT are visible (hence not collapsed perfectly) in all adopted transformations. Increasing ΔT results in an enhancement of real fluids effects (at the present conditions), yielding significant variations of the state of turbulence in the wall-normal direction, analyzed below via extraction of the semi-local friction Reynolds number, and density fluctuation intensity profiles.

Figure 4.5 shows the semi-local friction Reynolds number

$$\overline{Re}^*_\tau = \overline{Re}_\tau \sqrt{\overline{\rho}(y)/\overline{\rho}_w} / \left(\overline{\mu}(y)/\overline{\mu}_w\right) \tag{4.6}$$

where $\overline{Re}_\tau = \overline{\rho}_w \overline{u}_\tau h / \overline{\mu}_w$. The wall-normal y is here intended as relative to the wall (bottom or top) under consideration. The values of $\overline{Re}^*_\tau$ in the bottom-wall viscous sublayer are lower than those near the top wall; the opposite occurs in the respective log-law regions. However, values of $\overline{Re}^*_{\tau,bot}$ in the log region are comparable across the different ΔT considered, while $\overline{Re}^*_{\tau,top}$ systematically decreases in the respective log region as ΔT increases (and as the pseudophase transitioning region of the flow approaches the top-wall buffer layer). The overall higher sensitivity of the $\overline{Re}^*_\tau$ to the ΔT on the heated top wall is manifest in the van Driest transform velocity (Figures 4.4(a) and (b)), systematically increasing in value with ΔT for the top wall more than the bottom wall. On the other hand, the varying ΔT cases are collapsed by the TL transform in equal manners on both walls, despite real fluid effects being more pronounced at the top wall (as also discussed later and illustrated in Figures 4.9 and 4.10).

4.2.2 Turbulent Fluctuation Intensities

Table 4.2. Top-to-bottom difference in root-mean-square peak values of streamwise, wall-normal and spanwise velocity components, density, temperature, and pressure in percentage of the bottom peak rms value.

ΔT	5 K	10 K	20 K
$\Delta(u''_{rms,peak})$	−2.60 %	−4.65 %	−5.77 %
$\Delta(v''_{rms,peak})$	−6.69 %	−11.31 %	−19.74 %
$\Delta(w''_{rms,peak})$	−3.69 %	−10.36 %	−12.72 %
$\Delta(\rho''_{rms,peak})$	−31.71 %	3.90 %	31.84 %
$\Delta(T''_{rms,peak})$	−7.27 %	13.37 %	27.47 %
$\Delta(p''_{rms,peak})$	−18.83 %	−35.44 %	−25.30 %

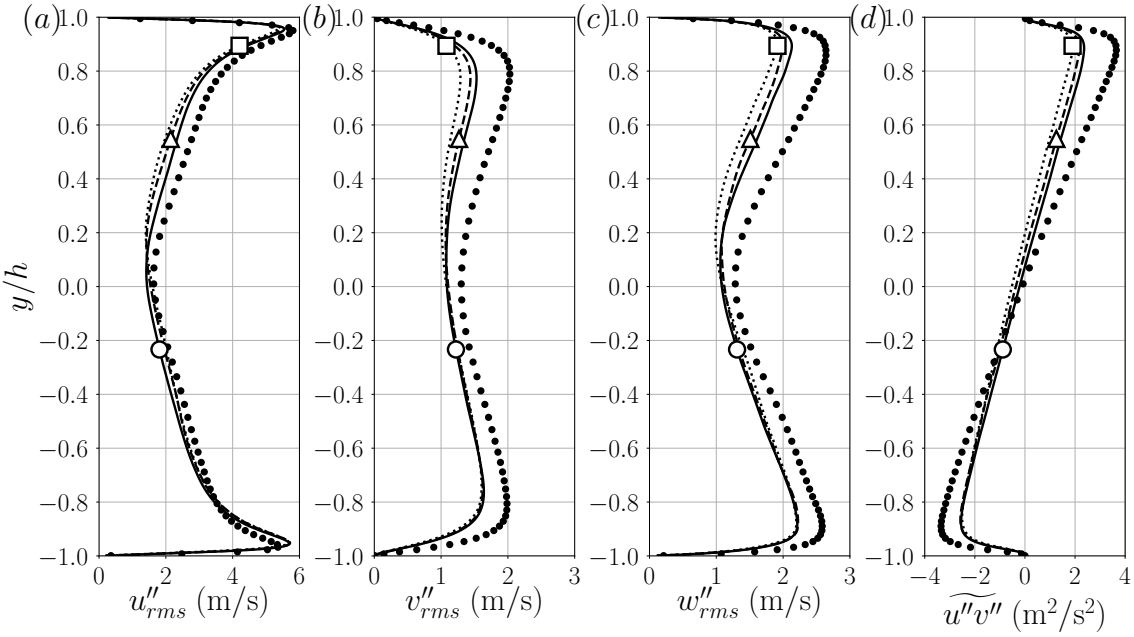

Figure 4.6. Root-mean-square of streamwise (a), wall-normal (b), and spanwise (c) Favre fluctuating velocity component and Reynolds shear stress (d) for $p_b = 1.1p_{cr}$ and $\Delta T = 5$ K (——), 10 K (- - -), and 20 K ($\cdots$) and rescaled ideal gas data (●) (in Section §2.4.2). Average location of pseudotransition for $\Delta T = 5$ K (○), 10 K (△), and 20 K (□).

Table 4.3. Peak ranges of the root-mean-square of streamwise, wall-normal, and spanwise Favre fluctuating velocity component and Reynolds shear stress at the bottom and top wall and their wall-normal location using the semi-local scaling.

	$(u''_{rms,peak})^*$	$(v''_{rms,peak})^*$	$(w''_{rms,peak})^*$	$\left\lvert\left(\widetilde{u''v''}_{peak}\right)^*\right\rvert$
Bot	3.25–3.34	0.91–0.92	1.25–1.27	0.81–0.83
	(y^* = 17.45–18.77)	(y^* = 93.51–103.24)	(y^* = 46.07–46.55)	(y^* = 47.91–54.06)
Top	3.19–3.23	0.83–0.89	1.20–1.24	0.77–0.80
	(y^* = 16.82–17.53)	(y^* = 84.18–86.04)	(y^* = 37.70–42.14)	(y^* = 42.41–45.94)

Other real fluid effects associated with transcritical thermal conditions are observable in the variance of the hydrodynamic turbulent fluctuations, as shown in Fig-

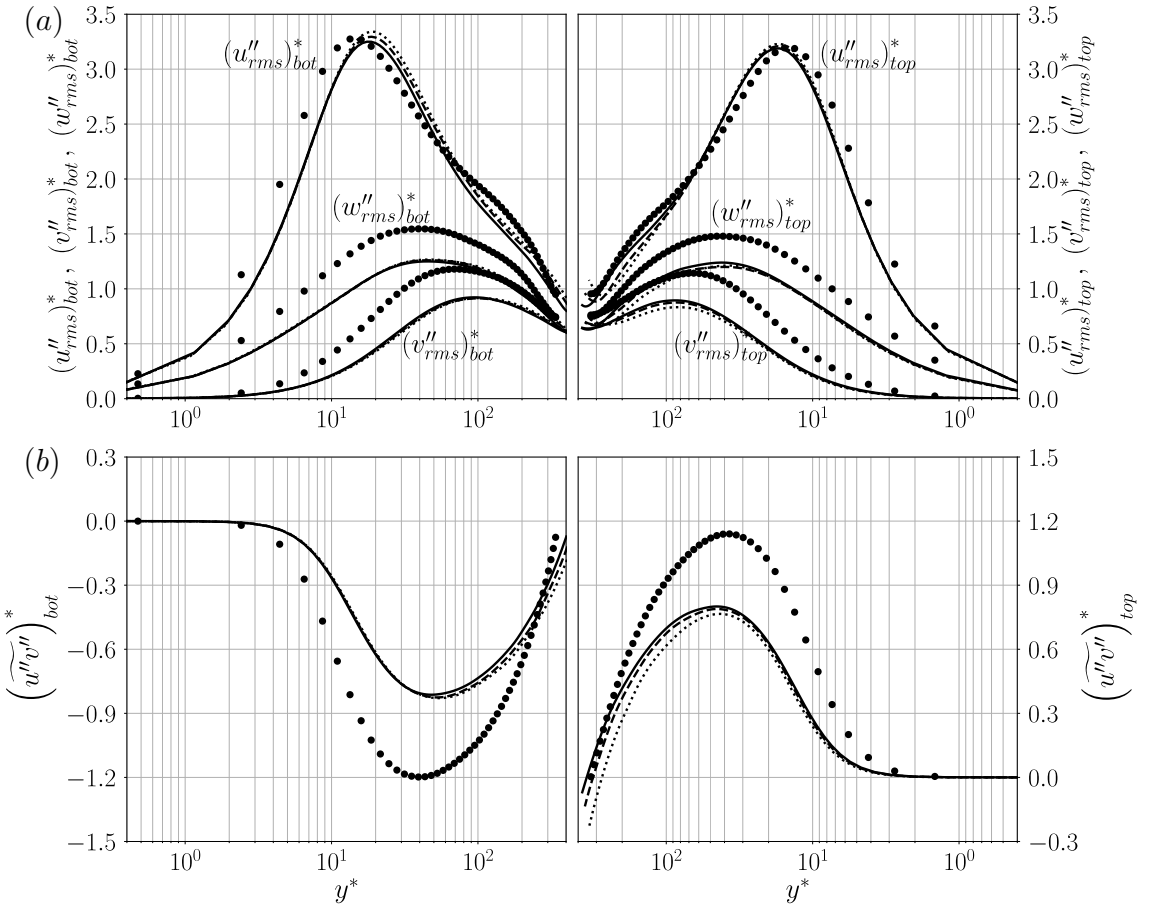

Figure 4.7. Semi-local scaled root-mean-square of streamwise, wall-normal, and spanwise Favre fluctuating velocity component (a) and Reynolds shear stress (b) at the bottom (left column) and top (right column) wall for $p_b = 1.1p_{cr}$ and $\Delta T = 5$ K (——), 10 K (- - -), and 20 K ($\cdots$) and rescaled ideal gas data (•) (in Section §2.4.2). Semi-local scaling factors are shown in Table B.1 in Appendix B.

ure 4.6. As ΔT increases, the asymmetries with respect to the channel centerplane grow, with peak fluctuation intensity values at the top wall (pseudogaseous region, towards which the pseudotransition location migrates) are attenuated with respect to the corresponding values in the pseudoliquid flow (see Table 4.2). This suggests the occurrence of damping of hydrodynamic turbulence due to the proximity to the region of pseudophase change. Such attenuation is noted in all Reynolds stress terms but is strongest in the wall-normal velocity component, directly involved in the turbulent

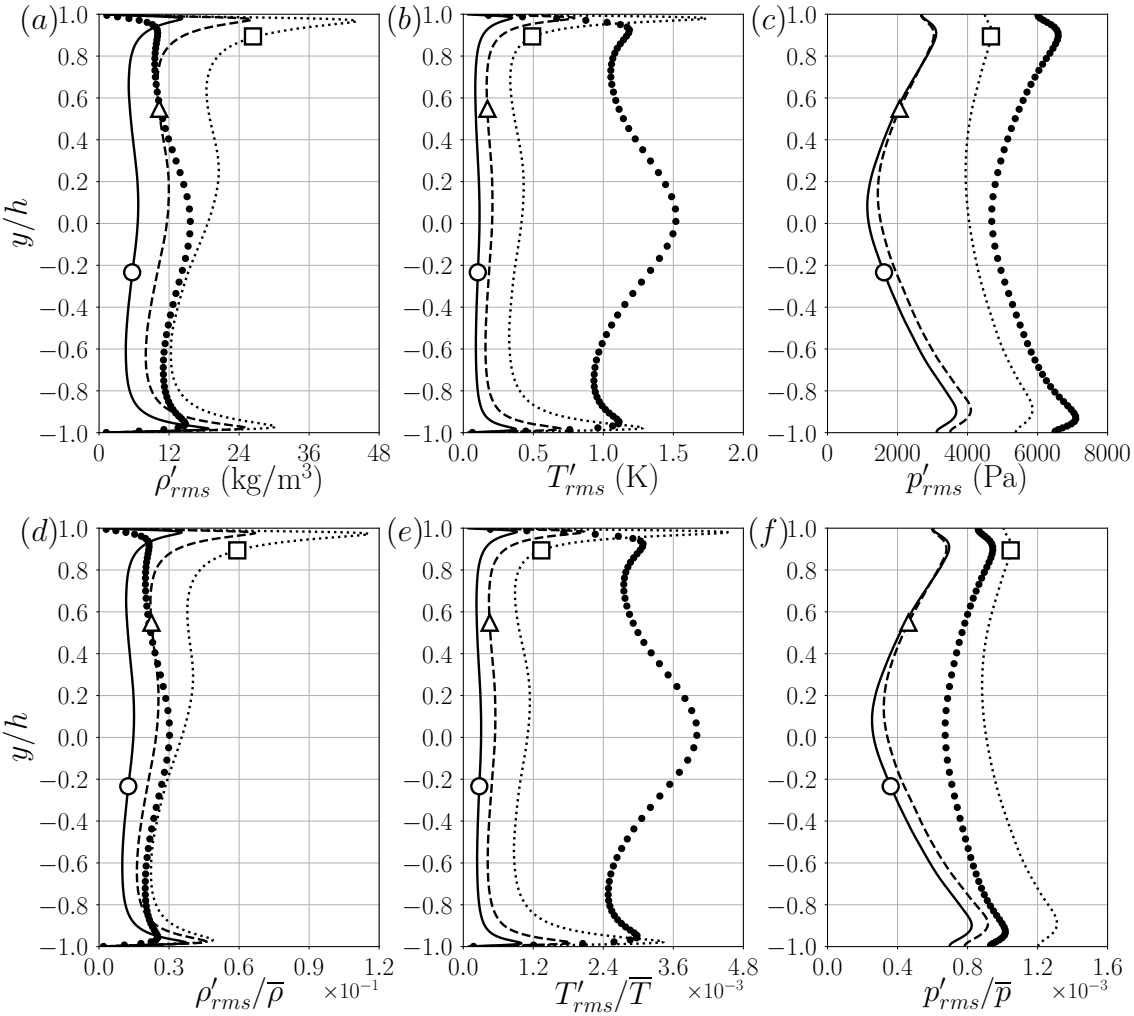

Figure 4.8. Root-mean-square of Reynolds fluctuations ((*a*)–(*c*)) and their normalized quantities ((*d*)–(*f*)) with respect to the local mean values for density ((*a*), (*d*)), temperature ((*b*), (*e*)), and pressure ((*c*), (*f*)) for $p_b = 1.1p_{cr}$ and $\Delta T = 5$ K (——), 10 K (- - -), and 20 K ($\cdots$) and rescaled ideal gas data (•) (in Section §2.4.2). Average location of pseudotransition for $\Delta T = 5$ K (○), 10 K (△), and 20 K (□).

heat and mass transport transport working against the steep mean temperature and density gradient. Following Morinishi *et al.* [61], in Figure 4.7, we show the semi-local scaled profiles of hydrodynamic turbulent fluctuations (see Table B.1 in Appendix B for the semi-local scaling factors). The semi-local scaling represents well the relative difference among the ideal gas and the real fluid cases and shows good collapse for the

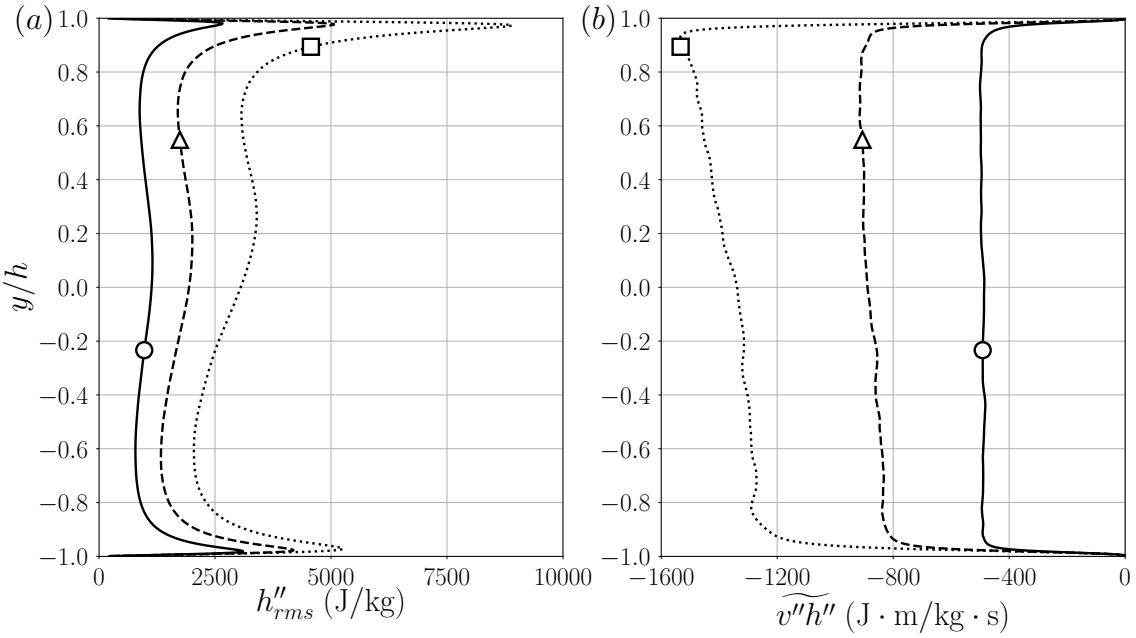

Figure 4.9. Root-mean-square of Favre fluctuations for enthalpy (a) and wall-normal turbulent enthalpy flux (b) for $p_b = 1.1p_{cr}$ and ΔT = 5 K (——), 10 K (- - -), and 20 K ($\cdots$). Average location of pseudotransition for $\Delta T = 5$ K (○), 10 K (△), and 20 K (□).

three ΔT conditions in terms of the peak value level and its location in the semi-local wall unit, y^* (see Table 4.3).

On the contrary, the proximity to the pseudophase change location y_{pb} (locally) and the increasing top-to-bottom temperature difference ΔT (globally) enhances the intensity of all thermodynamic fluctuations (Figures 4.8 and 4.9a). In spite of the damping in the wall-normal velocity fluctuations, the wall-normal turbulent enthalpy flux is enhanced (Figure 4.9b) by the increasing ΔT, as expected by the statistical steadiness of the flow, implying equilibrium conditions for the turbulent heat transfer.

For any given ΔT, the rms peak of density, temperature, and enthalpy closer to the location of pseudophase transition y_{pb} has a higher value than the other one farther away. Such asymmetry is quantified in Table 4.2. As y_{pb} moves upwards for increasing ΔT, it approaches the peak of the shear Reynolds stress and enthalpy flux (Figure 4.9b), only significantly increasing the latter roughly proportionally to ΔT.

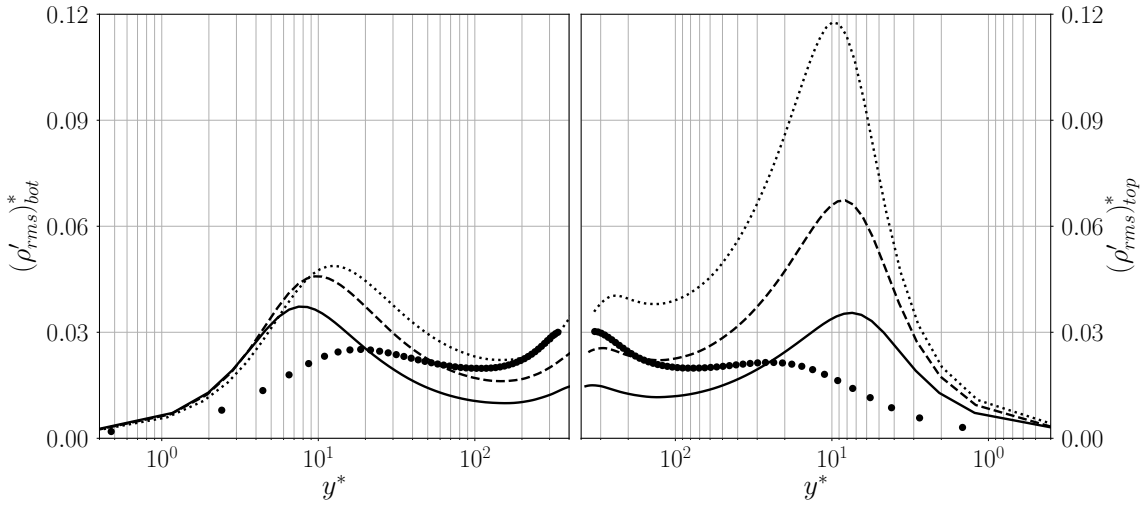

Figure 4.10. Semi-local scaled root-mean-square of Reynolds fluctuating density at the bottom (left) and top (right) wall for $p_b = 1.1p_{cr}$ and $\Delta T = 5$ K (——), 10 K (- - -), and 20 K ($\cdots$) and rescaled ideal gas data (•) (in Section §2.4.2). Semi-local scaling factors are shown in Table B.1 in Appendix B.

The density fluctuation intensity normalized by its mean local value shown in Figure 4.8 is significantly higher than the temperature fluctuation (for the $\Delta T = 20$ K, $(\rho'_{rms}/\overline{\rho})_{max} \simeq 26 \times (T'_{rms}/\overline{T})_{max}$). These real fluid effects have a direct impact on the structure of near-wall turbulence. In ideal gas cases, such as Coleman *et al.* [73]'s compressible isothermal wall channel flow, density and temperature fluctuations, scaled by their mean values, are almost identical to each other (see Figure 10 in Coleman *et al.* [73]). Previous calculations involving dense gases in a supersonic channel flow by Sciacovelli *et al.* [63] observed the maximum density fluctuation intensity located in the viscous sublayer and, as such, it was argued that it did not alter the turbulence structure significantly while satisfying Morkovin's hypothesis. In the present results, the ρ'_{rms} peak is located in the buffer layer, and much more pronounced at the top wall (where real fluid effects become more concentrated as ΔT increases) therein contributing to the inhomogeneity of the state of turbulence, as discussed earlier in the

analysis of the semi-local friction Reynolds number (Figure 4.5). The bottom and top near-wall peaks of ρ'_{rms} based on the semi-local scaling for the ΔT conditions in this study are located in $y^* = 7$–13 approximately corresponding to the buffer layer and the location moves slightly towards the channel centerplane with increasing ΔT (see Figure 4.10).

4.2.3 Grid Convergence Study

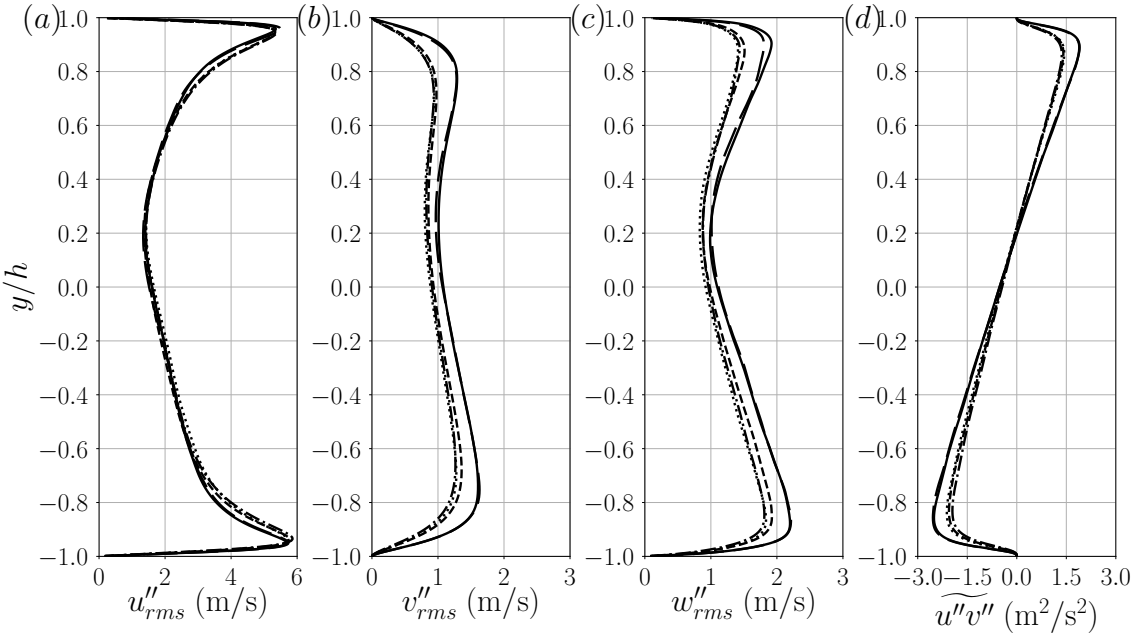

Figure 4.11. Root-mean-square of streamwise (a), wall-normal (b), and spanwise (c) Favre fluctuating velocity component and Reynolds shear stress (d) for $p_b = 1.1p_{cr}$ and $\Delta T = 20$ K at grid resolution of 64×96×64 ($\cdots$), 128×128×96 (- · -), 192×128×128 (- - -), 384×256×256 (– –), and 512×256×256 (——).

Grid convergence of transcritical flows is essential to determine the adequacy of a DNS as we recall that the minimal thermodynamic length scale to be resolved in transcritical flows is typically smaller than the Kolmogorov length scale. Insufficient spatial resolution is typically evidenced by a large spectral pile-up in the thermody-

Table 4.4. Friction Reynolds number and grid resolution in wall units $(u_\tau/\nu)^{-1}$ for the bottom and top portion of the channel evaluated with respective wall quantities. See also Table 2.4.

$N_x \times N_y \times N_z$		64×96×64	128×128×96	192×128×128	384×256×256	512×256×256
$\Delta T = 5$ K, $\rho_b = 450$ kg/m^3						
p_b		44.64 bar	44.65 bar	44.67 bar	44.66 bar	44.67 bar
Bottom	Re_τ	360	340	345	370	372
	Δx^+	67.50	31.88	21.56	11.56	8.72
	Δy^+	0.41–16.75	0.40–11.03	0.40–11.15	0.39–5.09	0.38–5.06
	Δz^+	22.50	14.17	10.78	5.78	5.81
Top	Re_τ	375	355	360	390	394
	Δx^+	70.31	33.28	22.50	12.19	9.23
	Δy^+	0.43–17.43	0.41–11.50	0.42–11.68	0.41–5.36	0.40–5.34
	Δz^+	23.44	14.79	11.25	6.09	6.16
$\Delta T = 10$ K, $\rho_b = 474$ kg/m^3						
p_b		44.58 bar	44.65 bar	44.65 bar	44.67 bar	44.69 bar
Bottom	Re_τ	345	325	335	365	364
	Δx^+	64.69	30.47	20.94	11.41	8.53
	Δy^+	0.40–16.13	0.38–10.65	0.39–10.87	0.38–4.96	0.37–4.93
	Δz^+	21.56	13.54	10.47	5.70	5.69
Top	Re_τ	365	345	355	385	387
	Δx^+	68.44	32.34	22.19	12.03	9.07
	Δy^+	0.42–16.98	0.40–11.24	0.41–11.48	0.40–5.28	0.40–5.25
	Δz^+	22.81	14.38	11.09	6.02	6.05
$\Delta T = 20$ K, $\rho_b = 520$ kg/m^3						
p_b		44.37 bar	44.43 bar	44.42 bar	44.55 bar	44.67 bar
Bottom	Re_τ	320	310	315	345	342
	Δx^+	60.00	29.06	19.69	10.78	8.02
	Δy^+	0.37–15.06	0.36–10.03	0.37–10.26	0.36–4.72	0.35–4.68
	Δz^+	20.00	12.92	9.84	5.39	5.34
Top	Re_τ	340	330	335	375	377
	Δx^+	63.75	30.94	20.94	11.72	8.84
	Δy^+	0.39–15.89	0.39–10.75	0.39–10.91	0.39–5.10	0.39–5.10
	Δz^+	21.25	13.75	10.47	5.86	5.89

namic quantities; in which case, the obtained results should be considered erroneous. In order to resolve the numerical error, we have used the top-hat filter with filtering factors as shown in Table 4.5. Here, the grid sensitivity is investigated for the most critical case of $\Delta T = 20$ K. Figure 4.11 shows the grid sensitivity of the velocity rms.

Table 4.5. Filtering factors used in the top-hat filter.

$N_x \times N_y \times N_z$	Index		
	i, j, or $k-1$	i, j, or k	i, j, or $k+1$
64×96×64	0.00005	0.99990	0.00005
128×128×96	0.00015	0.99970	0.00015
192×128×128	0.00025	0.99950	0.00025
384×256×256	0.00045	0.99910	0.00045
512×256×256	0.00055	0.99890	0.00055

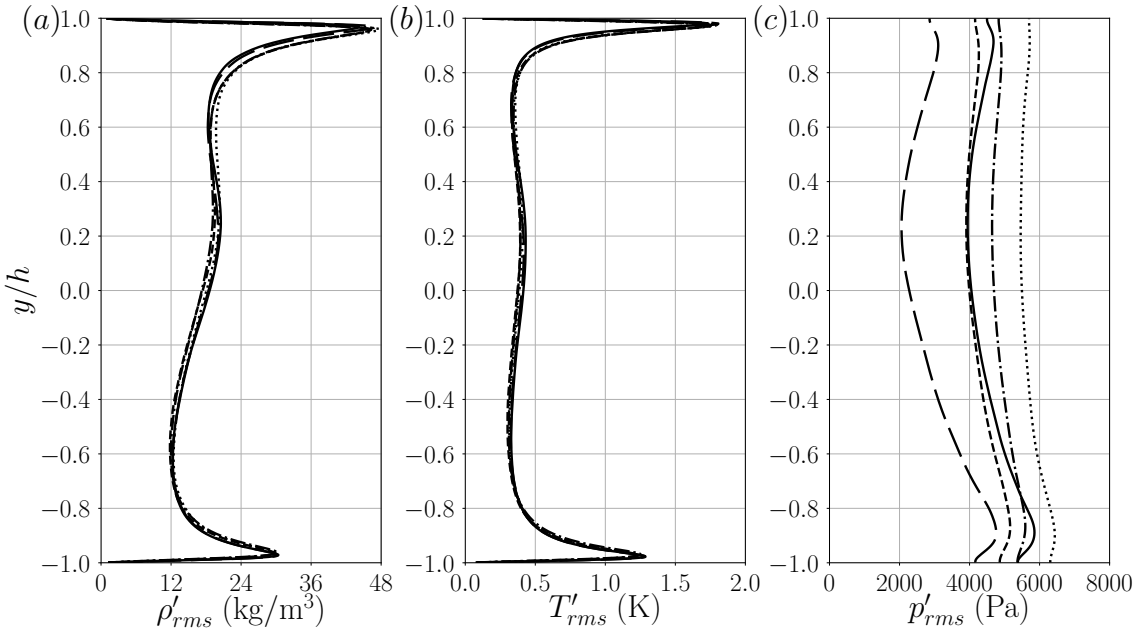

Figure 4.12. Root-mean-square of Reynolds fluctuations for density (a), temperature (b), and pressure (c) for $p_b = 1.1p_{cr}$ and $\Delta T = 20$ K at grid resolution of 64×96×64 ($\cdots$), 128×128×96 (- · -), 192×128×128 (- - -), 384×256×256 (– –), and 512×256×256 (——).

We highlight the insensitivity of the streamwise fluctuations to the grid resolution, whereas an unresolved simulation underestimates the peak fluctuations in the span-

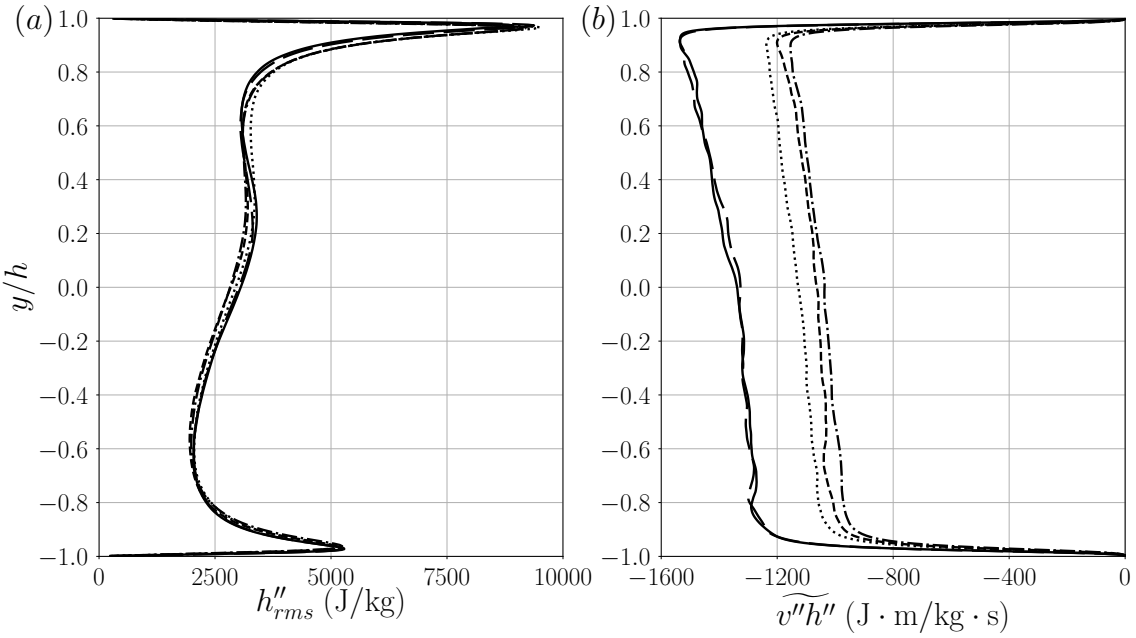

Figure 4.13. Root-mean-square of Favre fluctuations for enthalpy (a) and wall-normal turbulent enthalpy flux (b) for $p_b = 1.1p_{cr}$ and $\Delta T = 20$ K at grid resolution of 64×96×64 ($\cdots$), 128×128×96 (- · -), 192×128×128 (- - -), 384×256×256 (– –), and 512×256×256 (——).

wise and wall normal velocity components. The overall trends of the rms profiles (asymmetry, relative peak height etc.) are independent of the grid resolution.

The grid sensitivity of thermodynamic fluctuations is shown in Figures 4.12 and 4.13. We note a slow convergence of the thermodynamic quantities, particularly for the pressure. Figure 4.13 shows that the fluctuating enthalpy rms is well captured on a coarse mesh. But the turbulent enthalpy flux, an important quantity for the characterization of the convective heat transfer, requires a large grid count for a correct estimation. An insufficient grid resolution will underestimate the magnitude of the turbulence effect on the heat transfer in this transcritical system.

The one-dimensional energy spectra of fluctuating density, wall-normal velocity, and temperature in the streamwise and spanwise directions are presented in Figure 4.14. The profiles are extracted at $y/h = -0.97$, 0, and 0.97 which correspond to the location of the thermodynamic rms peaks (bottom and top wall) and the

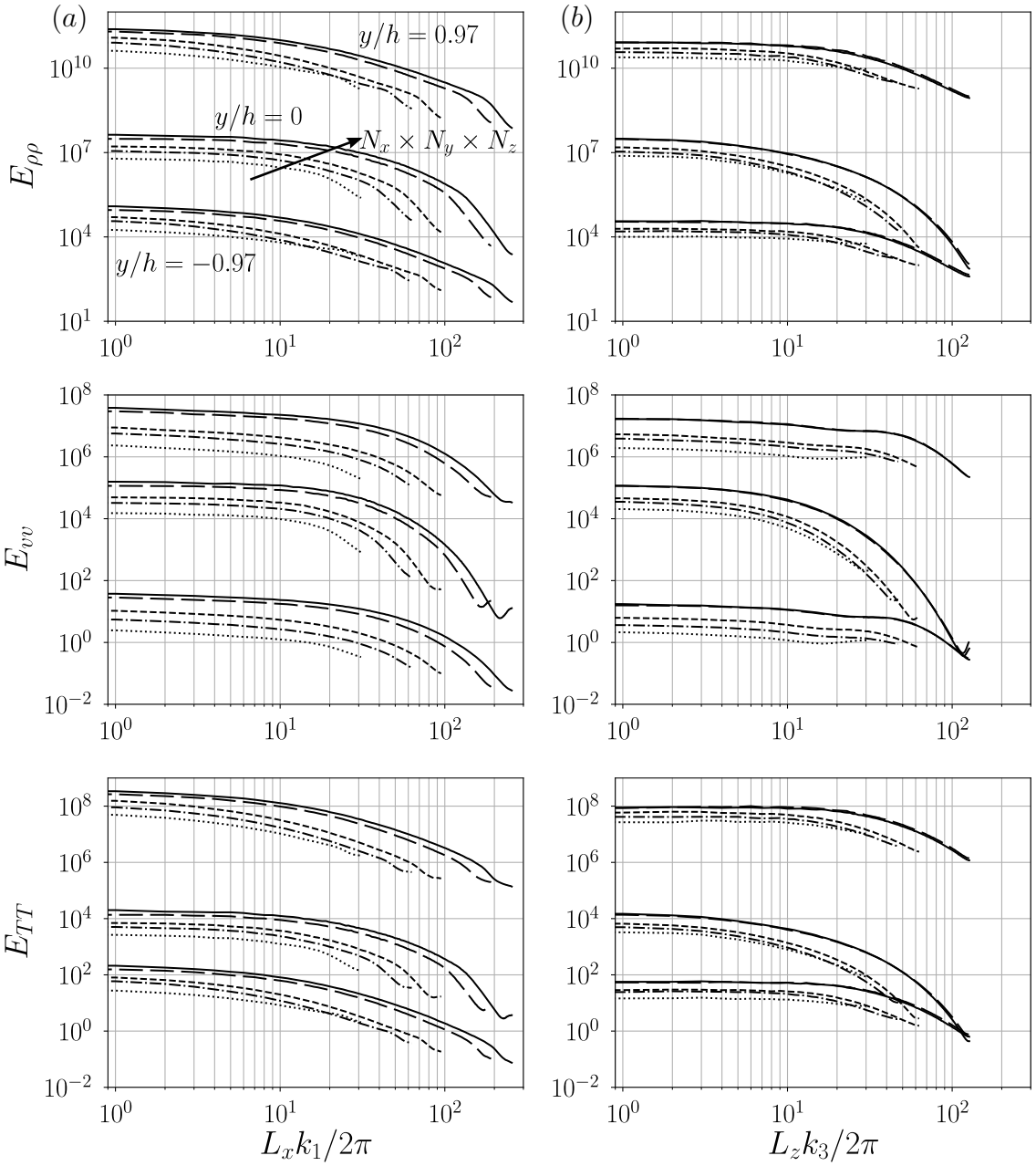

Figure 4.14. One-dimensional energy spectra of Reynolds averaged fluctuating density (top), wall-normal velocity (middle), and temperature (bottom) in the streamwise (a) and spanwise (b) directions extracted at the two near-wall peaks of density fluctuation intensity ($y/h = \pm 0.97$) and the centerplane ($y/h = 0$) for $p_b = 1.1 p_{cr}$ and $\Delta T = 20$ K at grid resolution of 64×96×64 ($\cdots$), 128×128×96 (- · -), 192×128×128 (- - -), 384×256×256 (– –), and 512×256×256 (——). Spectra for the centerplane and the top wall data have been shifted vertically by 3 decades and 6 decades respectively for clarity.

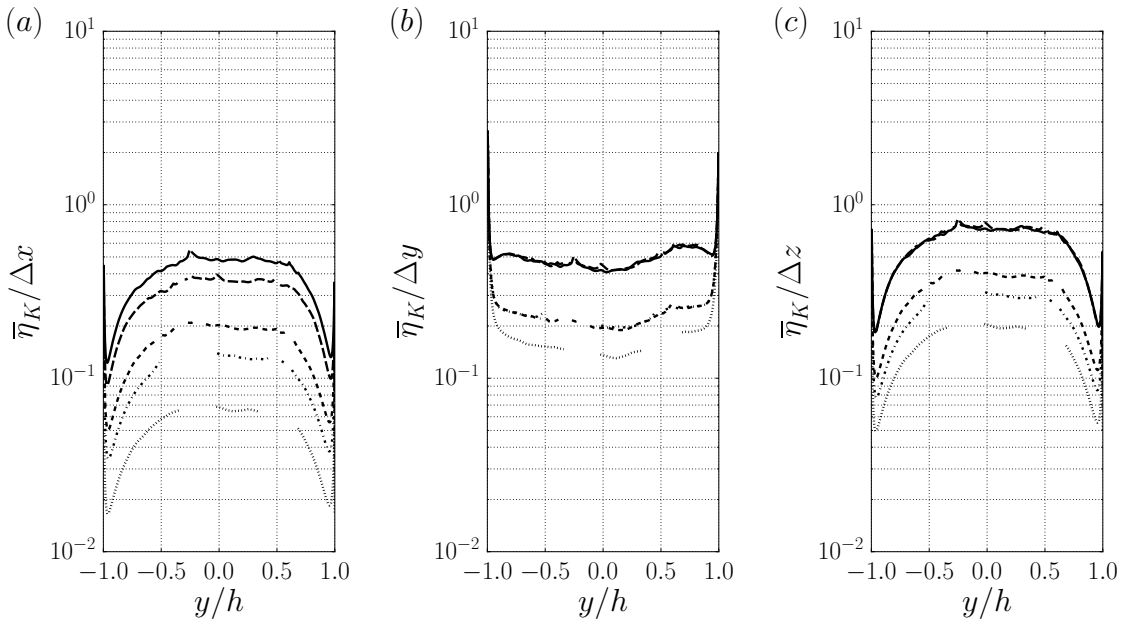

Figure 4.15. Normalized average Kolmogorov length scales, $\overline{\eta}_K/\Delta x$ (a), $\overline{\eta}_K/\Delta y$ (b), and $\overline{\eta}_K/\Delta z$ (c), at $p_b = 1.1p_{cr}$ and $\Delta T = 20$ K at grid resolution of 64×96×64 ($\cdots$), 128×128×96 (- ·-), 192×128×128 (- - -), 384×256×256 (– –), and 512×256×256 (——).

centerplane. As the grid resolution increases, the spectral broadening is observed with a slight increase at the high wavenumbers. Also, as expected, a build-up at high wavenumbers in the energy spectra is observed due to the higher sensitivity to inadequate spatial resolution due to the coupling of conservative compressible methods with cubic equations of state. The latter were mitigated by adopting a higher numerical resolution than what normally required for the given Reynolds number.

Figure 4.15 presents the average profiles of the normalized Kolmogorov length scale in the streamwise, wall-normal, and spanwise directions. The Kolmogorov scale, η_K, which quantifies the smallest turbulence length scale, is defined as

$$\eta_K \equiv \left(\frac{\nu^3}{\epsilon}\right)^{1/4} \tag{4.7}$$

where ϵ represents the dissipation rate of TKE per unit mass. For compressible flows, ϵ is defined as

$$\epsilon \equiv \frac{1}{\overline{\rho}} \overline{\tau_{ij} \frac{\partial u_i''}{\partial x_j}} \tag{4.8}$$

The profiles of the normalized Kolmogorov length scale approach unity as the grid resolution increases. It is observed that the flow in liquid-like phase needs a finer grid than that in the gas-like phase to resolve the turbulence length scale, which is a result of the larger density at the cooled wall. These figures show adequate grid resolution in the wall-normal direction, especially near the walls. This study also highlights the importance of a sufficient resolution in the streamwise direction as well.

4.3 High-Order Statistics, Probability Distribution Functions, and Turbulent Spectra

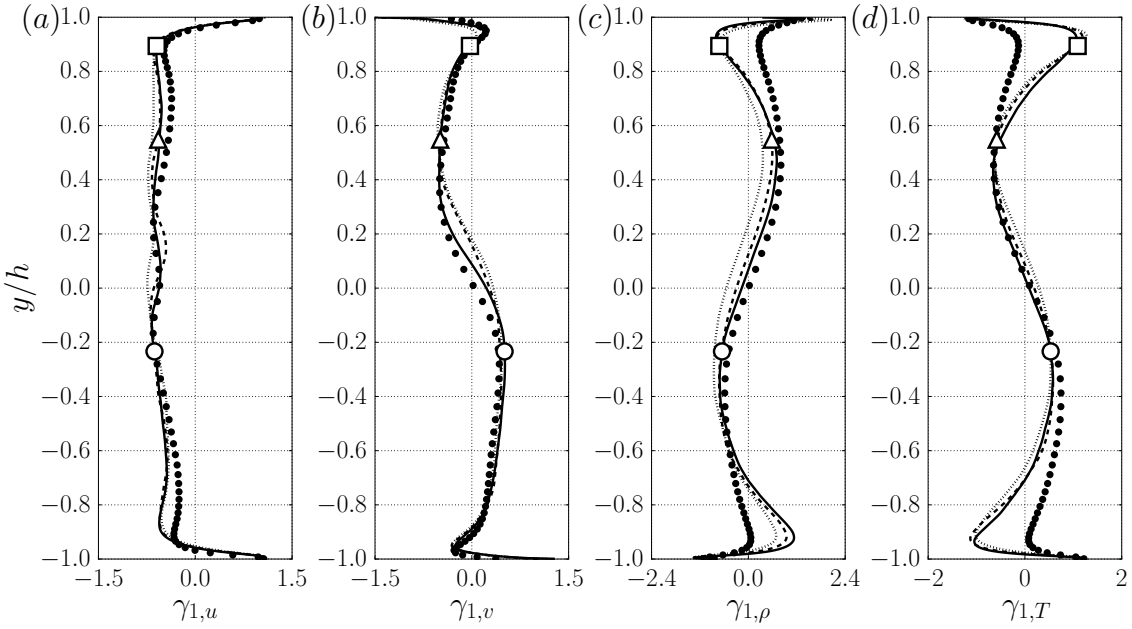

Figure 4.16. Skewness of the streamwise (a) and wall-normal (b) velocity component, density (c), and temperature (d) for $p_b = 1.1p_{cr}$ and $\Delta T = 5$ K (——), 10 K (- - -), and 20 K ($\cdots$) and rescaled ideal gas data (•) (in Section §2.4.2). Average location of pseudotransition for $\Delta T = 5$ K (○), 10 K (△), and 20 K (□).

The skewness of the fluctuating turbulent and thermodynamic quantities are presented in Figure 4.16. The high-order moments of the velocity fluctuations are, for the most part, unaffected by real fluid effects, although a more negative skewness of the streamwise velocity fluctuations is observed compared to ideal gas computations. The more noticeable difference is in the magnitude and sign of the skewness of density and temperature in the buffer layer regions; here the skewness of ideal gas density fluctuations approaches near zero values, while for the real fluid case it reaches an absolute maximum and with opposite sign with respect to the ideal gas case.

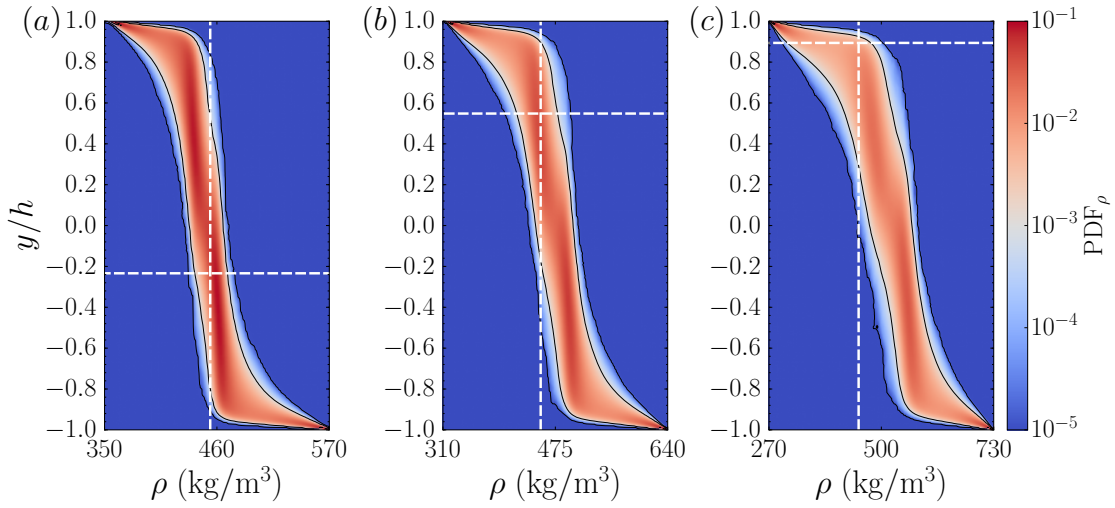

Figure 4.17. Contour of PDF of total density and the average location of pseudotransition, $y = y_{pb}$, pseudoboiling density value $\rho = \rho_{pb}$ $(- -)$ for $p_b = 1.1p_{cr}$ and $\Delta T = 5$ K (a), 10 K (b), and 20 K (c). The solid black line corresponds to the isocontour level $\mathrm{PDF}_\rho = 10^{-3}$. Note that the plot extremes on the horizontal axis are increased for increasing ΔT.

The positive peak in density skewness at the bottom wall is the result of intermittent events (discussed in more detail in Section §4.4), which eject dense fluid from the pseudoliquid sublayer into the channel core kept in pseudoboiling conditions. Same considerations hold for the top wall, but in reverse, justifying the negative skewness peak of density observed there. No similar structure is observed in the skewness profiles of the ideal gas case. The skewness of temperature follows a specular pattern with respect to density, suggesting that fluctuations in pressure might not play a dominant role in the mass and momentum transport.

To gain more insight into the structure of thermodynamic fluctuations, the PDF of density and temperature have been extracted at all locations (Figures 4.17 and 4.18). The PDFs widen as ΔT increases, as expected. Confirming previous observations, the largest variance is observed when pseudotransition takes place in the turbulent buffer layer, occurring at the top wall buffer layer for $\Delta T = 20$ K. While the variance of the turbulent velocity fluctuations decreases with increasing ΔT, the broader PDF

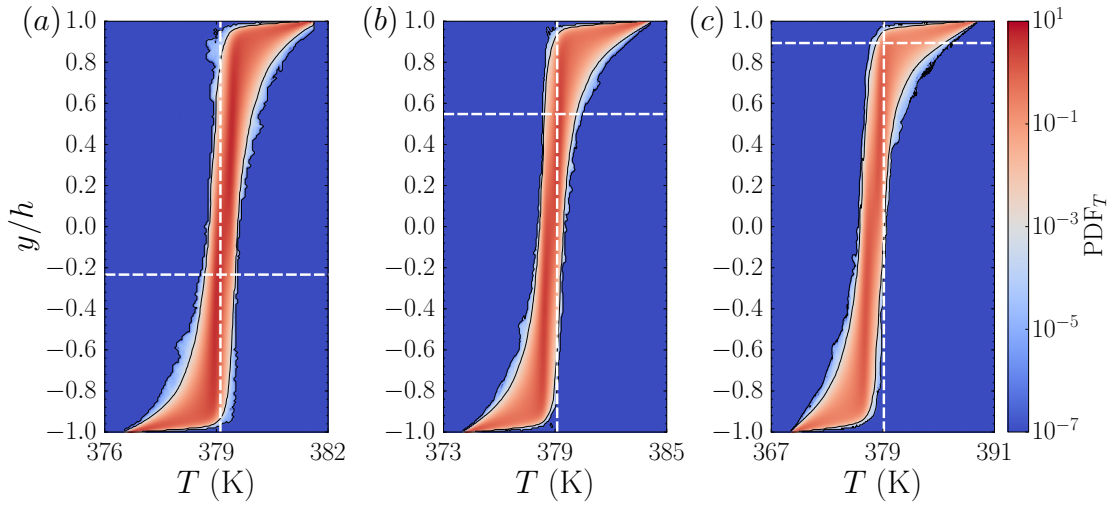

Figure 4.18. Contour of PDF of total temperature and the average location of pseudotransition, $y = y_{pb}$, pseudoboiling density value $\rho = \rho_{pb}$ $(--)$ for $p_b = 1.1p_{cr}$ and $\Delta T = 5$ K (a), 10 K (b), and 20 K (c). The solid black line corresponds to the isocontour level $\mathrm{PDF}_\rho = 10^{-3}$. Note that the plot extremes on the horizontal axis are increased for increasing ΔT.

of thermodynamic fluctuations is associated with the steepening of the corresponding gradients (Figure 4.3).

The analysis in Figures 4.19 and 4.20 focuses on three locations: the two buffer layers and the pseudophase transitioning location and includes a comparison with the ideal gas data. For both density and temperature, it is observed that the pseudophase transitioning region exhibits are much narrower distribution of the PDFs, whereas the buffer layers display a very pronounced kurtosis, with very rapid roll off at the tails of the distribution. Such PDF with very high kurtosis is not observed in the density PDF of the ideal gas case, while it is for the temperature PDF (see Table 4.6 for details).

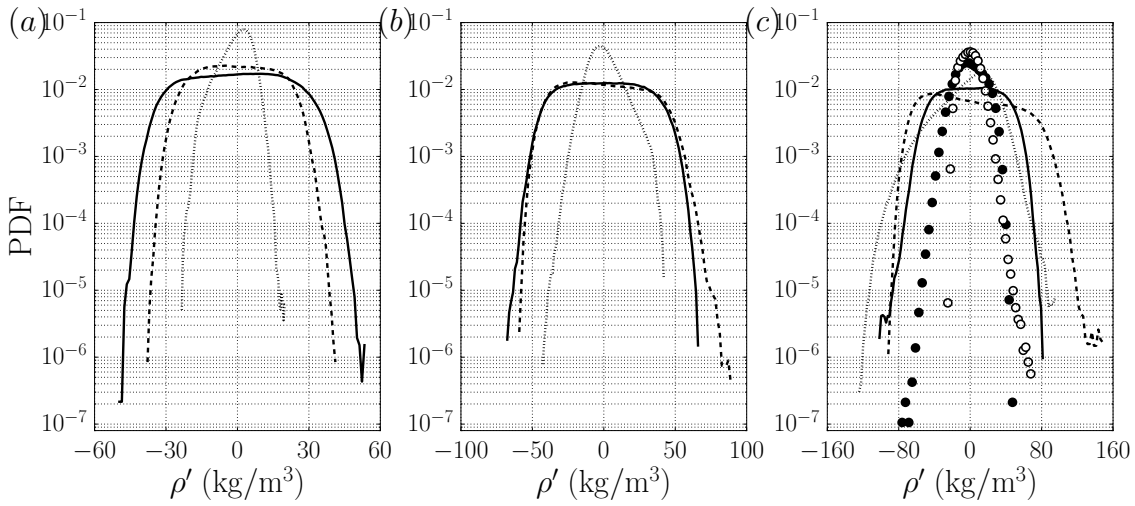

Figure 4.19. Probability distribution function (PDF) of fluctuating density at the bottom (——, •) and top (- - -, ∘) locations of peak ρ_{rms} and at the average location of pseudotransition $y = y_{pb}$ ($\cdots$) for $p_b = 1.1p_{cr}$ and $\Delta T = 5$ K (a), 10 K (b), and 20 K (c) and rescaled ideal gas data (circles) (in Section §2.4.2). Note that the plot extremes on the horizontal axis are increased for increasing ΔT.

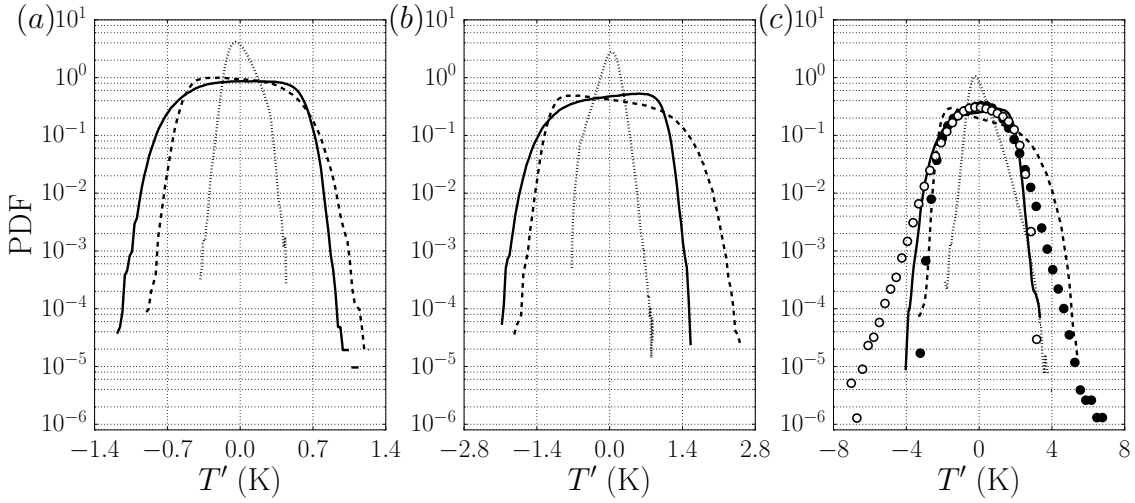

Figure 4.20. Probability distribution function (PDF) of fluctuating temperature at the bottom (——, •) and top (- - -, ∘) locations of peak T_{rms} and at the average location of pseudotransition $y = y_{pb}$ ($\cdots$) for $p_b = 1.1p_{cr}$ and $\Delta T = 5$ K (a), 10 K (b), and 20 K (c) and rescaled ideal gas data (circles) (in Section §2.4.2). Note that the plot extremes on the horizontal axis are increased for increasing ΔT.

Table 4.6. Minimum and maximum values of fluctuating density and temperature at the approximate bottom wall ($y \simeq -0.97h$) and top wall ($y \simeq 0.97h$) rms peak locations and at the average location of pseudotransition, $y = y_{pb}$.

ΔT (K)		5	10	20
$y = -0.97h$	ρ'_{min} (kg/m^3)	−49.58	−67.58	−101.55
	ρ'_{max} (kg/m^3)	53.33	65.93	81.23
	T'_{min} (K)	−1.18	−2.07	−4.03
	T'_{max} (K)	1.13	1.56	3.34
$y = 0.97h$	ρ'_{min} (kg/m^3)	−37.76	−59.18	−91.68
	ρ'_{max} (kg/m^3)	41.11	90.18	148.37
	T'_{min} (K)	−1.04	−1.83	−3.35
	T'_{max} (K)	1.24	2.51	5.39
$y = y_{pb}$	ρ'_{min} (kg/m^3)	−23.36	−42.69	−124.41
	ρ'_{max} (kg/m^3)	20.26	41.93	94.67
	T'_{min} (K)	−0.38	−0.73	−1.88
	T'_{max} (K)	0.44	0.83	4.06

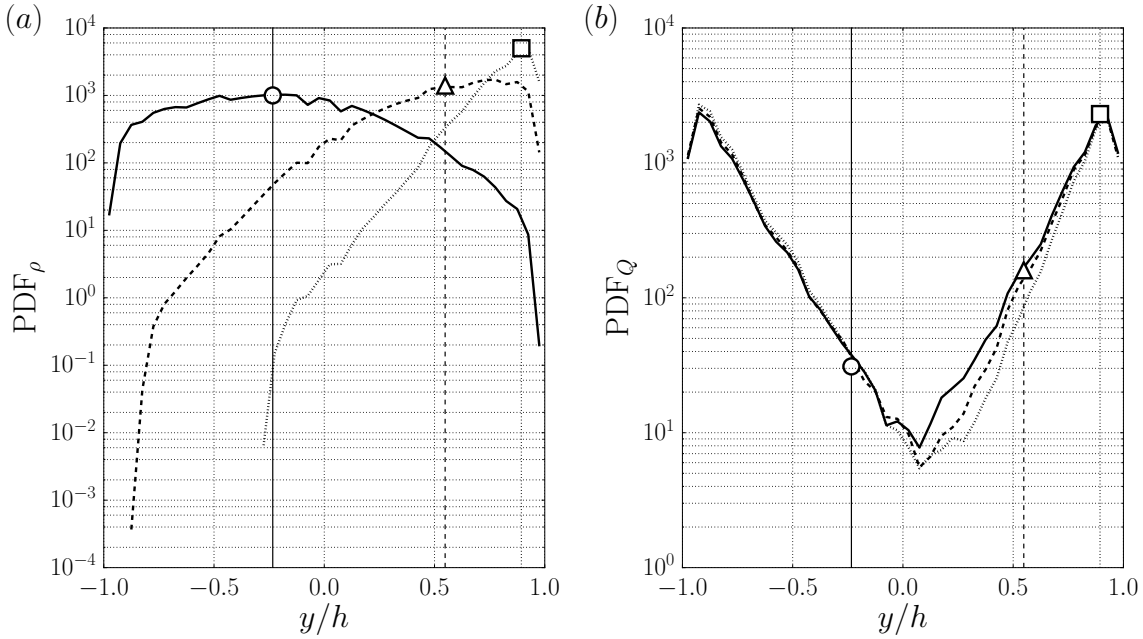

Figure 4.21. PDF of y/h values conditional to $|\rho - \rho_{pb}| \leq 5.9$ kg/m^3 where $\rho_{pb} = 453.5$ kg/m^3 corresponding to $T_{pb} \pm 0.1$ K (a) and $Q = 2.49 \times 10^9$–2.51×10^9 1/s^2 (b) with average locations of the pseudo-transition for $p_b = 1.1p_{cr}$ and $\Delta T = 5$ K (——, ○), 10 K (- - -, △), and 20 K ($\cdots$, □).

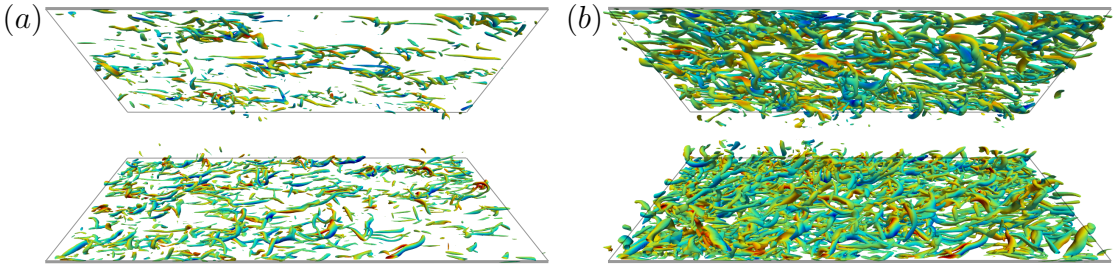

Figure 4.22. Isosurfaces of Q-criterion at $Q = 2.5 \times 10^9$ 1/s^2 (a) and 0.5×10^9 1/s^2 (b) colored by the wall-normal velocity for $p_b = 1.1p_{cr}$ and $\Delta T = 20$ K.

Figure 4.21a presents the PDF conditioned to a density range centered about its pseudotransitioning value. These results provide the probability of an instantaneous pseudophase change event at a given y location, or equivalently, the probability of the pseudointerface being instantaneously located at a given y location. The location corresponding to the highest event count moves upwards in the channel as ΔT increases and the distribution is narrowed; $y/h = -0.17$ for $\Delta T = 5$ K, 0.78 for $\Delta T = 10$ K, and 0.93 for $\Delta T = 20$ K. However, these values do not exactly match the average pseudotransition locations determined by the mean quantities (shown in Figure 4.1 and indicated with symbols in Figure 4.21), especially for $\Delta T = 10$ K. As a result, despite having a mean pseudotransition location at $y_{pb}/h = 0.55$ in the $\Delta T = 10$ K case, the greatest probability is much closer to the top wall, at about $y/h = 0.8 - 0.9$.

A coherent-structure-based probability distribution is also extracted (Figure 4.21b). Conditioning the PDF on a selected Q-criteria value ($Q = 2.49 \times 10^9$–2.51×10^9 1/s^2 as used in Figures 4.22a and 4.25b), allows to identify the effects of increasing ΔT on the structural make-up of turbulence under transcritical conditions. In line with the observed turbulence damping in the vicinity of pseudotransition conditions, a reduction of the population density of turbulent structures in the top half of the channel is observed with increasing ΔT. As quantitatively shown by the reduction in the number of observed events in the conditional statistics in Figure 4.21b. This effect is observed for several values of the Q-criterion (Figure 4.22) and is consistent with the increasing asymmetry in the turbulent velocity profiles for increasing ΔT as shown in Figure 4.6.

Figure 4.23 shows one-dimensional energy spectra of fluctuating density, wall-normal velocity, and temperature and cospectra of fluctuating wall-normal velocity and temperature in the near-wall regions, which are heavily affected by the wall-generated turbulence. All the profiles roll off rapidly at high wavenumbers; providing further evidence of the adequacy of the resolution of both the hydrodynamic and thermodynamic quantities. The cospectrum of the wall-normal velocity and temperature fluctuations, E_{vT}, is also analyzed here to gain insight into the fundamental nature

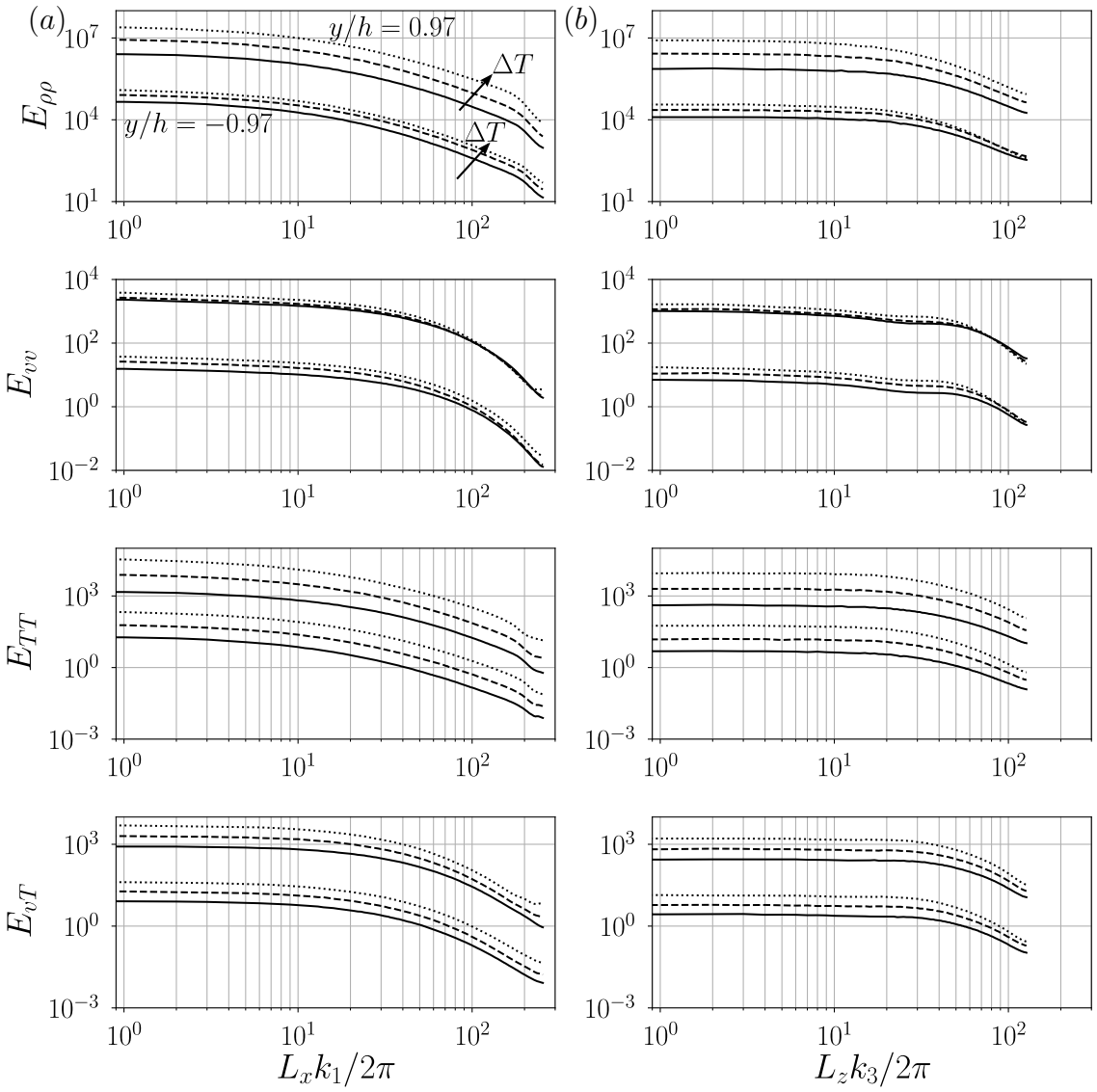

Figure 4.23. One-dimensional energy spectra of Reynolds averaged fluctuating density (first row), wall-normal velocity (second row), and temperature (third row) and one-dimensional cospectra between the Reynolds averaged fluctuating wall-normal velocity and temperature (fourth row) in the streamwise (a) and spanwise (b) direction extracted at the two near-wall peaks of density fluctuation intensity ($y/h = \pm 0.97$) for $p_b = 1.1 p_{cr}$ and $\Delta T = 5$ K (——), 10 K (- - -), and 20 K ($\cdots$). Spectra for the top wall data have been shifted vertically by 2 decades for clarity.

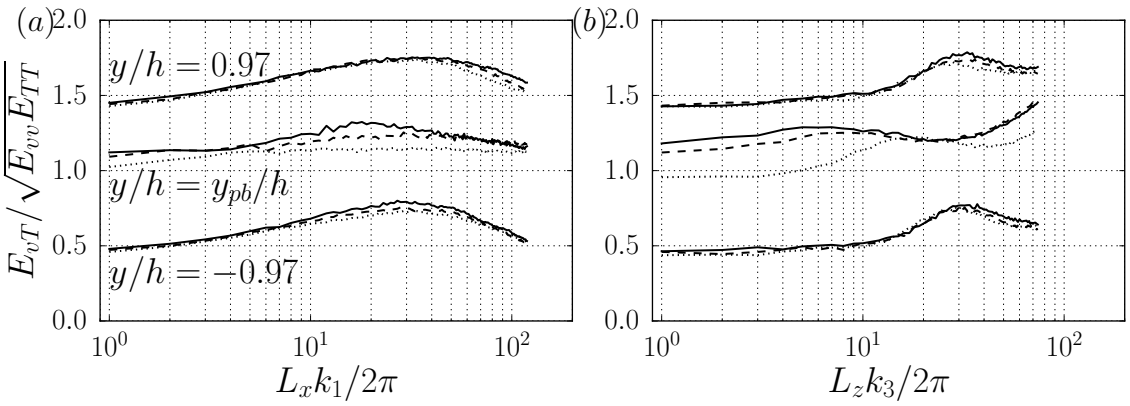

Figure 4.24. One-dimensional coherence between the Reynolds averaged fluctuating wall-normal velocity and temperature in the streamwise (a) and spanwise (b) direction extracted at the two near-wall peaks of density fluctuation intensity ($y/h = \pm 0.97$) and the average location of the pseudotransition based on the mean quantities for $p_b = 1.1p_{cr}$ and $\Delta T = 5$ K (——), 10 K (- - -), and 20 K ($\cdots$). Coherence for the pseudotransition and the top near-wall peak data have been shifted vertically by 0.5 and 1.0 respectively for clarity.

of their interaction. Its value increases with ΔT, as expected, given the increase of the wall-to-wall heat flux. Normalizing the cospectrum based on the single-variable spectra (Figure 4.24) reveals an unexpected loss of transport efficiency, or coherence, at the pseudophase changing location for intermediate wave numbers as ΔT is increased; this is observed for both the streamwise and spanwise directions. Overall, the hydrodynamic and thermodynamic effects are highly correlated at or around the energy-containing turbulent length scale.

4.4 Coherent Structures and Thermodynamics

Instantaneous isosurfaces of density and Q-criterion as well as corresponding flooded contours of wall heat flux are shown in Figure 4.25, for the bottom-wall only, to investigate the coupling between heat and mass transfer effects and the role coherent turbulent structures in the transport. The density isosurface at $\rho = 468$

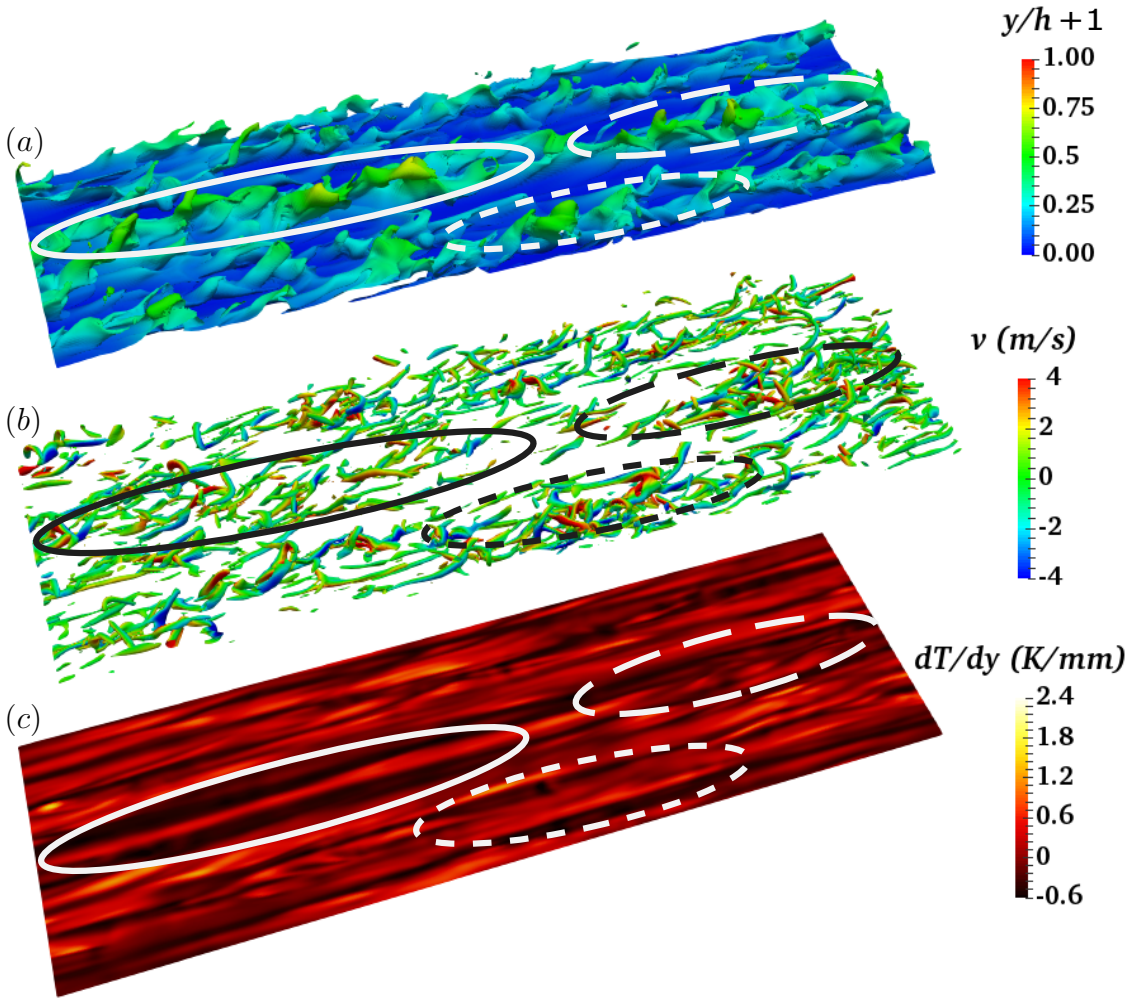

Figure 4.25. Isosurfaces of density ($\rho = 468$ kg/m^3) colored by the distance from the bottom wall (a), Q-criterion ($Q = 2.5 \times 10^9$ 1/s^2) colored by the wall-normal velocity (b), and temperature gradient (c) for $p_b = 1.1p_{cr}$ and $\Delta T = 5$ K (*enhanced online* – `https://www.youtube.com/embed/JqF_ZrucSqs`).

kg/m^3 (value which corresponds to $y/h = -0.9$ in the mean density profile shown in Figure 4.1) exhibits clear ejection events from the pseudoliquid region (near the cold, bottom wall) as the near-wall turbulence lifts-up the dense fluid into the lighter core of the channel. As the ejected fluid has more inertia than its lighter surrounding, and no gravitational effects are accounted for in these simulations, it reaches the core of the

channel ($y/h = 0$, see red-colored surfaces) where the fluid undergoes a pseudophase change, effectively achieving mass transport. Naturally, the gravitational forces (in a stably stratified flow setup) would play a mitigating role in the observed mixing dynamics. This pseudophase change and the concomitant effects on the thermodynamics are a unique characteristic of transcritical flows and explain the high positive values of skewness of density (Figure 4.16) in the bottom-half of the channel.

The Q-criterion isosurface identifies the turbulent structures based on the velocity gradients alone. Interestingly, large-scale streamwise aligned structures are observed near the wall (see the circles), leading to the choice of a long computational domain length in the streamwise direction, 12 times the half-channel width, approximately twice the typical length required by the current friction Reynolds number (see Table 4.4). Figure 4.25*c* shows the corresponding elongated streaks in the wall-heat flux, spatially correlated with the ejection locations caused by the streamwise-elongated turbulent structures.

Two-point velocity correlations in the streamwise and spanwise direction (Figure 4.26) are extracted to confirm that, indeed, the computational box size has been adequately picked. A large streamwise and small spanwise coherence is observed near the top and bottom wall, confirming the visual observation of the narrow elongated streaks from Figure 4.25. We note a much longer streamwise correlation length in the u velocity (correlation reaches zero at about 0.15 r_x/L_x) than in w (reaches zero at about 0.05 r_x/L_x). The lateral two-point correlation are consistent with the longitudinal ones and the three-dimensional visualizations. The signature of streamwise aligned streaks result in a short spanwise correlation length near the walls.

In the center of the channel, turbulence is nearly isotropic, a fact observed from the integral length scale analysis. The integral length scale (not shown) at the channel center is about 9% of the width. The integral length scales relative to the local Kolmogorov scale are presented in Figure 4.27, once again, revealing the remarkably extended correlation length of the near wall structures.

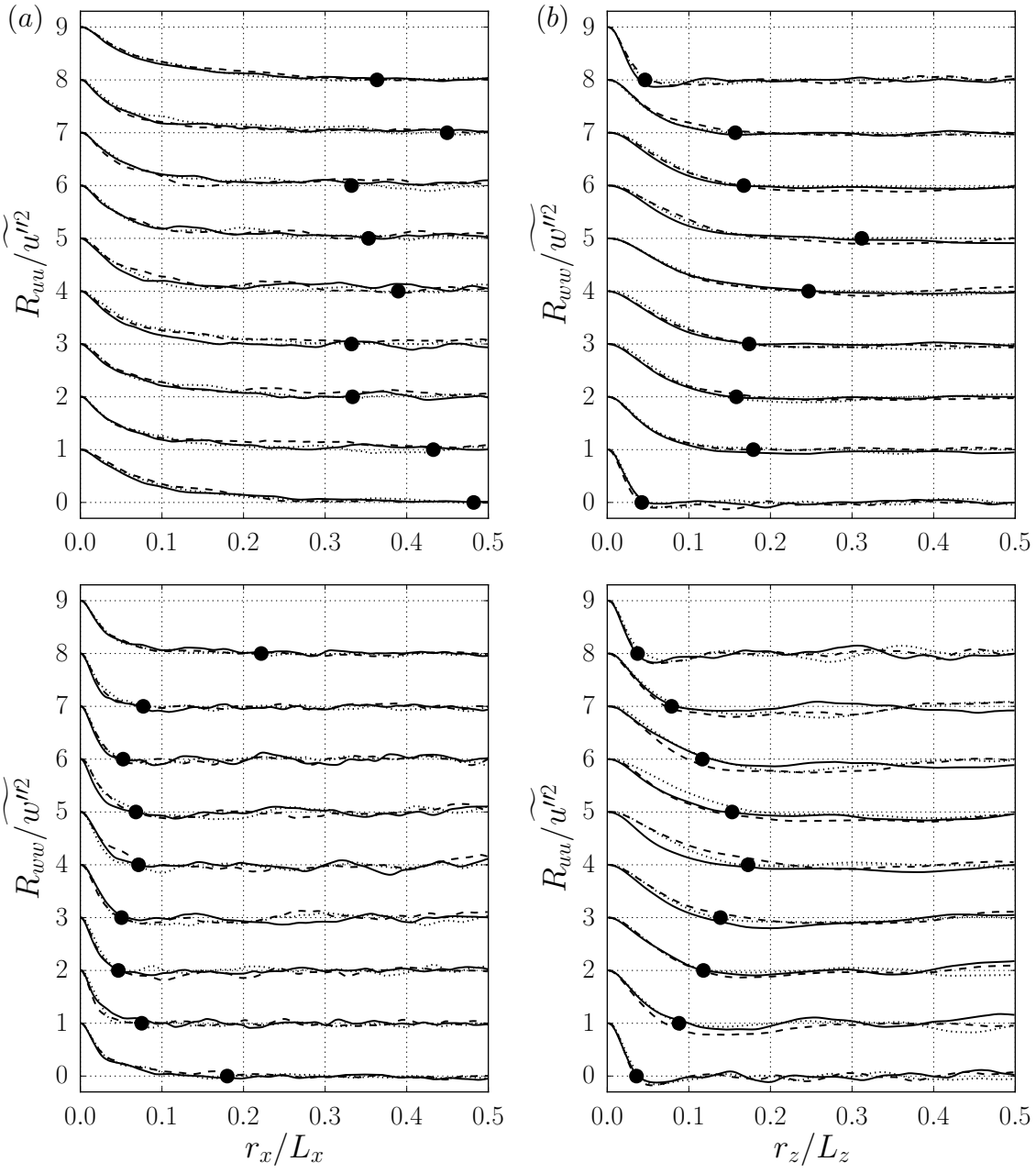

Figure 4.26. Normalized longitudinal (top) and lateral (bottom) two-point correlations of velocity in the streamwise (a) and spanwise (b) direction extracted at $y/h = -0.97$, -0.75, -0.50, -0.25, 0.00, 0.25, 0.50, 0.75, and 0.97 for $p_b = 1.1p_{cr}$ and $\Delta T = 5$ K (——), 10 K (- - -), and 20 K ($\cdots$). The lines have been shifted vertically corresponding to each y/h from bottom to top. Average location of first zero-crossing points for $\Delta T = 5$ K, 10 K, and 20 K (●).

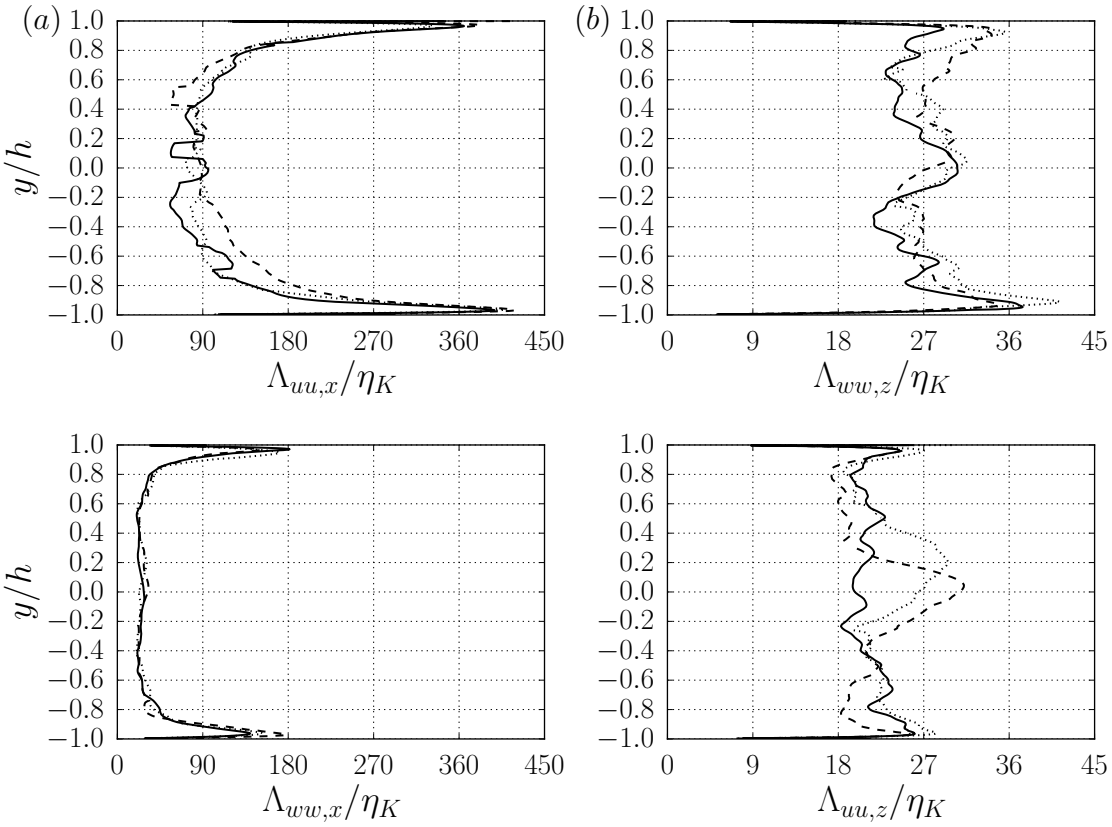

Figure 4.27. Ratio of the integral length scale (longitudinal (top) and lateral (bottom)) and the local Kolmogorov scale in the streamwise (a) and spanwise (b) direction. $\Delta T = 5$ K (——), 10 K (- - -), and 20 K ($\cdots$).

In addition to the hydrodynamic correlations, thermodynamic two-point correlations are presented in Figure 4.28. The two-point correlations for density and compressibility factor reflect the real fluid characteristics discussed in Figure 4.8. The correlations have the identical tendency showing the long streamwise and short spanwise correlation lengths near the walls and vice versa in the center region. The large streamwise coherence near the walls accords with the manifestation of pseudoliquid flow streaks observed in Figure 4.25. These longer streaky structures are also observed in variable density, supersonic wall-bounded flows with cooled walls [73]. As the fluctuating density is enhanced (see Figure 4.10), so is the momentum transfer in

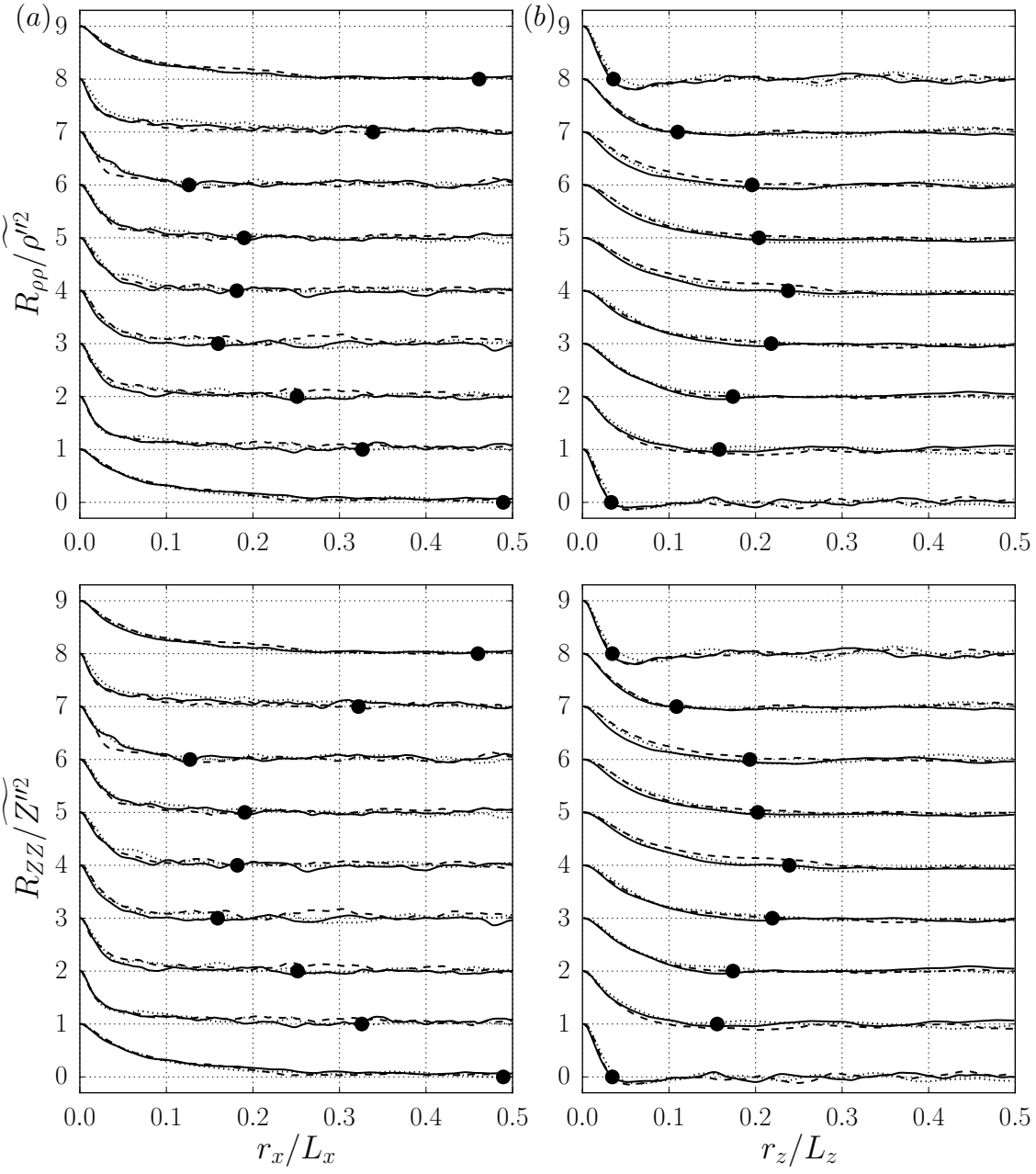

Figure 4.28. Normalized two-point correlations of density (top) and compressibility factor (bottom) in the streamwise (a) and spanwise (b) direction extracted at $y/h = -0.97$, -0.75, -0.50, -0.25, 0.00, 0.25, 0.50, 0.75, and 0.97 for $p_b = 1.1p_{cr}$ and $\Delta T = 5$ K (——), 10 K (- - -), and 20 K ($\cdots$). The lines have been shifted vertically corresponding to each y/h from bottom to top. Average location of first zero-crossing points for $\Delta T = 5$ K, 10 K, and 20 K (●).

the wall normal. As a result, the higher momentum particles travel a longer distance, imparting an enhanced streaky-structure to the near wall flow. The flow ejected from the walls in long streamwise streaks eventually take on a blob-like (shorter streamwise, longer spanwise structure) form as the ejected fluid reaches the channel centerplane. The strong similarity between all ΔT conditions is noted.

5 CONCLUSIONS

We have performed direct numerical simulations of natural and forced convection with differentially heated walls (ΔT equals $T_{bot} - T_{top}$ for natural convection pseudoboiling and $T_{top} - T_{bot}$ for turbulent forced convection) bracketing the pseudoboiling temperature at a slightly supercritical pressure in order to investigate their turbulent structures and heat transfer dynamics. R-134a (also called 1,1,1,2-tetrafluoroethane, CH_2FCF_3), carbon dioxide (CO_2), and methanol (CH_3OH) are used as the working fluid (only R-134a for forced convection). By defining a statistically steady flow at transcritical temperature conditions, the turbulence and thermodynamic coupling could be studied. The simulations were conducted by solving the fully compressible Navier–Stokes equations and special attention was paid to fully resolving all scales of the hydro- and thermodynamics of the setup to avoid nonphysical oscillations which are characteristic of these flows. The Peng–Robinson equation of state was used with a consistent thermodynamic formulation to investigate the real fluid effects. A realistic Prandtl number is used and computed from the Chung's model to estimate the dynamic viscosity and thermal conductivity.

The natural convection pseudoboiling study expiscated that increasing temperature difference between the walls enables to shorten the period of recirculation occured by the buoyancy effect and enhance the flow mixing and heat transfer. The two-dimensional simulation of carbon dioxide at $\Delta T = 20$ K results in the even-numbered mode change in the pseudoliquid region. The equivalent wall heat flux increases logarithmically with ΔT and the scaled equivalent wall heat flux introducing the thermal conductive sublayer thickness shows good agreement except for the two-dimensional carbon dioxide case. The proposed heat transfer correlation model considering Gr, Pr, density, and transport properties is proper (roughly) to characterize the supercritical natural convection. The conditioned probability distribution function proves

the breakup of global recirculation zone observed in the instantaneous flow fields by increasing ΔT. The analysis on turbulent statistics shows that the real fluid effects result in the large gradient of thermodynamic quantities at the location occuring the pseudophase change and the higher ΔT condition needs finer grid resolution in order to capture the turbulence length scales fully.

In the turbulent forced convection study, by varying the differential heating of the channel walls, the average location of the pseudophase change could be controlled, varying from $y/h = -0.23$, 0.55, and 0.89 for $\Delta T = 5$ K, 10 K, and 20 K, respectively. At the pseudophase change, the thermodynamic nonlinearity are maximal, therefore the resulting effects of the thermodynamic nonlinearities on turbulence could be investigated. Conventional near-wall velocity scaling laws cannot capture the velocity distribution in transcritical flows due to the large density and thermophysical variations; even recent improvements to scaling laws for heated and cooled walls cannot accurately capture these effects. This leads us to conclude that additional wall modeling for transcritical flow is essential to correctly capture the near-wall dynamics of transcritical flows. One justification for the near-wall modeling challenges stems from nonlinear thermodynamic effects in the wall turbulence. The real fluid thermodynamic effects inhibit hydrodynamic turbulence through a decrease in the dilatational production term of the enstrophy equation (not shown). The profiles of the thermodynamic fluctuations show a higher intensity in the pseudogas (hot wall) compared to the pseudoliquid (cold wall) region; this occurs despite a reduction in the turbulence intensity near the top wall. The conditional probability distribution function of density shows a narrowing of the distribution with increasing differential heating. When the pseudophase change occurs near the wall ($\Delta T = 20$ K case), a highly skewed and very narrow distribution is observed, which results from the nonlinear dynamics as the pseudophase change occurs near the viscous sublayer. The structural signature of the turbulence in transcritical flows remains the most striking. Near the wall, the turbulence is aligned in long, yet meandering, streamwise coherent structures and the integral length scales are over 400 times the local Kolmogorov scale. The instanta-

neous visualizations and the two-point correlations have shown that strong ejections of heavy fluid into the channel core affect the structures and dynamics of turbulent channel flow and leave streaks in the temperature gradients at the wall.

REFERENCES

REFERENCES

[1] V. P. Carey. *Pool boiling.*, chapter 7. Taylor & Francis, second edition, 2007.

[2] Y. Katto. Critical heat flux. *Int. J. Multiphase Flow*, 20(1):53–90, 1994.

[3] V. Yang. Modeling of supercritical vaporization, mixing, and combustion processes in liquid-fueled propulsion systems. *Proc. Combust. Inst.*, 28:925–942, 2000.

[4] J. Y. Yoo. The turbulent flows of supercritical fluids with heat transfer. *Annu. Rev. Fluid Mech.*, 45:495 – 525, 2013.

[5] L. Xu, P. Kumar, S. V. Buldyrev, S.-H. Chen, P. H. Poole, F. Sciortino, and H. E. Stanley. Relation between the Widom line and the dynamic crossover in systems with a liquid–liquid phase transition. *Proc. Natl. Acad. Sci.*, 102(46):16558–16562, 2005.

[6] F. Sciortino, P. H. Poole, U. Essmann, and H. E. Stanley. Line of compressibility maxima in the phase diagram of supercooled water. *Phys. Rev. E*, 55(1):727–737, 1997.

[7] L. Liu, S.-H. Chen, A. Faraone, C.-W. Yen, and C.-Y. Mou. Pressure dependence of fragile-to-strong transition and a possible second critical point in supercooled confined water. *Phys. Rev. Lett.*, 95(11):117802 1–4, 2005.

[8] G. G. Simeoni, T. Bryk, F. A. Gorelli, M. Krisch, G. Ruocco, M. Santoro, and T. Scopigno. The Widom line as the crossover between liquid-like and gas-like behaviour in supercritical fluids. *Nature Physics*, 6:503–507, 2010.

[9] V. V. Brazhkin, Y. D. Fomin, A. G. Lyapin, V. N. Ryzhov, and E. N. Tsiok. Widom line for the liquid–gas transition in Lennard–Jones system. *J. Phys. Chem. B*, 115(48):14112–14115, 2011.

[10] S. Artemenko, P. Krijgsman, and V. Mazur. The Widom line for supercritical fluids. *J. Mol. Liq.*, 238:122–128, 2017.

[11] D. T. Banuti. Crossing the Widom-line – Supercritical pseudo-boiling. *J. Supercritical Fluids*, 98:12–16, 2015.

[12] S. C. Tucker. Solvent density inhomogeneities in supercritical fluids. *Chem. Rev.*, 99:391–418, 1999.

[13] F. Gorelli, M. Santoro, T. Scopigno, M. Krisch, and G. Ruocco. Liquid-like behavior of supercritical fluids. *Phys. Rev. Lett.*, 97(24):245702, 2006.

[14] S. Yoshikawa, R. L. Smith Jr., H. Inomata, Y. Matsumura, and K. Arai. Performance of a natural convection circulation system for supercritical fluids. *J. Supercritical Fluids*, 36(1):70–80, 2005.

[15] H. Tokanai, Y. Ohtomo, H. Horiguchi, E. Harada, and M. Kuriyama. Heat transfer of supercritical CO_2 flow in natural convection circulation system. *Heat Transfer Eng.*, 31(9):750–756, 2010.

[16] K. K. Knapp and R. H. Sabersky. Free convection heat transfer to carbon dioxide near the critical point. *Int. J. Heat Mass Transfer*, 9(1):41–51, 1966.

[17] N. Hasan and B. Farouk. Buoyancy driven convection in near-critical and supercritical fluids. *Int. J. Heat Mass Transfer*, 55(15–16):4207–4216, 2012.

[18] V. Chatoorgoon. Stability of supercritical fluid flow in a single-channel natural-convection loop. *Int. J. Heat Mass Transfer*, 44(10):1963–1972, 2001.

[19] G. R. Dimmick, V. Chatoorgoon, H. F. Khartabil, and R. B. Duffey. Natural-convection studies for advanced CANDU reactor concepts. *Nucl. Eng. Des.*, 215(1–2):27–38, 2002.

[20] P. K. Vijayan, H. Austregesilo, and V. Teschendorff. Simulation of the unstable oscillatory behavior of single-phase natural circulation with repetitive flow reversals in a rectangular loop using the computer code ATHLET. *Nucl. Eng. Des.*, 155(3):623–641, 1995.

[21] X.-R. Zhang, L. Chen, and H. Yamaguchi. Natural convective flow and heat transfer of supercritical CO_2 in a rectangular circulation loop. *Int. J. Heat Mass Transfer*, 53(19–20):4112–4122, 2010.

[22] L. Chen, X.-R. Zhang, H. Yamaguchi, and Z.-S. Liu. Effect of heat transfer on the instabilities and transitions of supercritical CO_2 flow in a natural circulation loop. *Int. J. Heat Mass Transfer*, 53(19–20):4101–4111, 2010.

[23] L. Chen and X.-R. Zhang. Simulation of heat transfer and system behavior in a supercritical CO_2 based thermosyphon: Effect of pipe diameter. *J. Heat Transfer*, 133(12):122505–1–8, 2011.

[24] B. Zappoli, D. Bailly, Y. Garrabos, B. Le Neindre, P. Guenoun, and D. Beysens. Anomalous heat transport by the piston effect in supercritical fluids under zero gravity. *Phys. Rev. A*, 41(4):2264–2267, 1990.

[25] A. Onuki and R. A. Ferrel. Adiabatic heating effect near the gas-liquid critical point. *Physica A: Statistical Mechanics and its Applications*, 164(2):245–264, 1990.

[26] H. Boukari, M. E. Briggs, J. N. Shaumeyer, and R. W. Gammon. Critical speeding up observed. *Phys. Rev. Lett.*, 65(21):2654–2657, 1990.

[27] H. S. Swenson, J. R. Carver, and C. R. Kakarala. Heat transfer to supercritical water in smooth-bore tubes. *J. Heat Transfer*, 87(4):477–483, 1965.

[28] Y.-Y. Bae and H.-Y. Kim. Convective heat transfer to CO_2 at a supercritical pressure flowing vertically upward in tubes and an annular channel. *Exp. Thermal Fluid Sci.*, 33(2):329–339, 2009.

[29] S. Mokry, I. Pioro, A. Farah, K. King, S. Gupta, W. Peiman, and P. Kirillov. Development of supercritical water heat-transfer correlation for vertical bare tubes. *Nucl. Eng. Des.*, 241(4):1126–1136, 2011.

[30] E. W. P. Hahne. Natural convection heat transfer through an enclosed horizontal layer of supercritical carbon dioxide. *Wärme- und Stoffübertragung*, 1:190–196, 1968.

[31] R. J. Neumann and E. W. P. Hahne. Free convective heat transfer to supercritical carbon dioxide. *Int. J. Heat Mass Transfer*, 23(12):1643–1652, 1980.

[32] R. C. Hendricks, R. J. Simoneau, and R. V. Smith. Survey of heat transfer to near-critical fluids. Technical Report NASA TN D-5886, National Aeronautics and Space Administration, 1970.

[33] I. L. Pioro and R. B. Duffey. Experimental heat transfer in supercritical water flowing inside channels (survey). *Nucl. Eng. Des.*, 235(22):2407–2430, 2005.

[34] J. Wang, H. Li, S. Yu, and T. Chen. Investigation on the characteristics and mechanisms of unusual heat transfer of supercritical pressure water in vertically-upward tubes. *Int. J. Heat Mass Transfer*, 54(9–10):1950–1958, 2011.

[35] I. Pioro. *Application of supercritical pressure in power engineering: Specifics of thermophysical properties and forced-convective heat transfer.*, chapter 11. Elsevier, first edition, 2014.

[36] P. J. Giarratano, V. D. Arp, and R. V. Smith. Forced convection heat transfer to supercritical helium. *Cryogenics*, 11(5):385–393, 1971.

[37] I. L. Pioro and R. B. Duffey. *Heat-transfer enhancement at supercritical pressures.*, chapter 9. ASME Press, first edition, 2007.

[38] J. W. Ackerman. Pseudoboiling heat transfer to supercritical pressure water in smooth and ribbed tubes. *J. Heat Transfer*, 92(3):490–497, 1970.

[39] K. Yamagata, K. Nishikawa, S. Hasegawa, T. Fujii, and S. Yoshida. Forced convective heat transfer to supercritical water flowing in tubes. *Int. J. Heat Mass Transfer*, 15(12):2575–2593, 1972.

[40] B. S. Shiralkar and P. Griffith. Deterioration in heat transfer to fluids at supercritical pressure and high heat fluxes. *J. Heat Transfer*, 91(1):27–36, 1969.

[41] S. M. Liao and T. S. Zhao. An experimental investigation of convection heat transfer to supercritical carbon dioxide in miniature tubes. *Int. J. Heat Mass Transfer*, 45(25):5025–5034, 2002.

[42] J. H. Bae, J. Y. Yoo, and H. Choi. Direct numerical simulation of turbulent supercritical flows with heat transfer. *Phys. Fluids*, 17:105104, 2005.

[43] X. R. Zhang and H. Yamaguchi. Forced convection heat transfer of supercritical CO_2 in a horizontal circular tube. *J. Supercritical Fluids*, 41(3):412–420, 2007.

[44] H. Nemati, A. Patel, B. J. Boersma, and R. Pecnik. The effect of thermal boundary conditions on forced convection heat transfer to fluids at supercritical pressure. *J. Fluid Mech.*, 800:531–556, 2016.

[45] M. J. Casiano, J. R. Hulka, and V. Yang. Liquid-propellant rocket engine throttling: A comprehensive review. *J. Propul. Power*, 26(5):897–923, 2010.

[46] R. S. Thurston. Pressure oscillations induced by forced convection heat transfer to two phase and supercritical hydrogen. Technical Report LAMS-3070, Los Alamos Scientific Laboratory, February 1964.

[47] M. Palumbo. *Predicting the onset of thermoacoustic oscillations in supercritical fluids.* PhD thesis, Purdue University, October 2009.

[48] H. Wang, J. Zhou, Y. Pan, and N. Wang. Experimental investigation on the onset of thermo-acoustic instability of supercritical hydrocarbon fuel flowing in a small-scale channel. *Acta Astronautica*, 117:296–304, December 2015.

[49] S. Kawai, H. Terashima, and H. Negishi. A robust and accurate numerical method for transcritical turbulent flows at supercritical pressure with an arbitrary equation of state. *J. Comput. Phys.*, 300(Supplement C):116 – 135, 2015.

[50] D.-Y. Peng and D. B. Robinson. A new two-constant equation of state. *Ind. Eng. Chem. Fundam.*, 15(1):59–64, 1976.

[51] M. B. Ewing and C. J. Peters. *Fundamental considerations.*, chapter 2. Elsevier, first edition, 2000.

[52] T.-H. Chung, M. Ajlan, L. L. Lee, and K. E. Starling. Generalized multiparameter correlation for nonpolar and polar fluid transport properties. *Ind. Eng. Chem. Res.*, 27(4):671–679, 1988.

[53] B. E. Poling, J. M. Prausnitz, and J. P. O'Connell. *The properties of gases and liquids.* McGraw-Hill, 2001.

[54] E. W. Lemmon, M. O. McLinden, and D. G. Friend. *Thermophysical properties of fluid systems, NIST chemistry webbook, NIST standard reference database.* Number 69. National Institute of Standards and Technology, Gaithersburg MD, 20899, 2016.

[55] J. Larsson, S. K. Lele, and P. Moin. Effect of numerical dissipation on the predicted spectra for compressible turbulence. *Annual Research Briefs, Center for Turbulence Research, Stanford*, 2007.

[56] J. Larsson and S. K. Lele. Direct numerical simulation of canonical shock/turbulence interaction. *Phys. Fluids*, 21:126101, 2009.

[57] J. Larsson, I. Bermejo-Moreno, and S. K. Lele. Reynolds- and Mach-number effects in canonical shock–turbulence interaction. *J. Fluid Mech.*, 717:293–321, 2 2013.

[58] I. Bermejo-Moreno, J. Bodart, J. Larsson, and B. M. Barney. Solving the compressible Navier–Stokes equations on up to 1.97 million cores and 4.1 trillion grid points. In *IEEE International Conference on High Performance Computing*, 2013.

[59] The HDF Group. Hierarchical data format, version 5., 1998. http://www.hdfgroup.org/HDF5/.

[60] P. G. Huang, G. N. Coleman, and P. Bradshaw. Compressible turbulent channel flows: DNS results and modelling. *J. Fluid Mech.*, 305:185–218, 1995.

[61] Y. Morinishi, S. Tamano, and K. Nakabayashi. Direct numerical simulation of compressible turbulent channel flow between adiabatic and isothermal walls. *J. Fluid Mech.*, 502:273–308, 2004.

[62] A. Patel, J. W. R. Peeters, B. J. Boersma, and R. Pecnik. Semi-local scaling and turbulence modulation in variable property turbulent channel flows. *Phys. Fluids*, 27:095101, 2015.

[63] L. Sciacovelli, P. Cinnella, and X. Gloerfelt. Direct numerical simulations of supersonic turbulent channel flows of dense gases. *J. Fluid Mech.*, 821:153–199, 2017.

[64] S. Kawai. Direct numerical simulation of transcritical turbulent boundary layers at supercritical pressures with strong real fluid effects. In *54th AIAA Aerospace Sciences Meeting, San Diego, CA*, page 1992, 2016.

[65] M. V. Morkovin. Effects of compressibility on turbulent flows. *Mécanique de la Turb.*, 367:380, 1962.

[66] H. Nemati, A. Patel, B. J. Boersma, and R. Pecnik. Mean statistics of a heated turbulent pipe flow at supercritical pressure. *Int. J. Heat Mass Transfer*, 83:741–752, 2015.

[67] M. Pizzarelli, F. Nasuti, R. Paciorri, and M. Onofri. Numerical analysis of three-dimensional flow of supercritical fluid in asymmetrically heated channels. *AIAA J.*, 47:2534–2543, 2009.

[68] U. Sengupta, H. Nemati, B. J. Boersma, and R. Pecnik. Fully compressible low-mach number simulations of carbon-dioxide at supercritical pressures and trans-critical temperatures. *Flow Turb. Combust.*, 99:909–931, 2017.

[69] A. Trettel and J. Larsson. Mean velocity scaling for compressible wall turbulence with heat transfer. *Phys. Fluids*, 28:026102, 2016.

[70] E. R. van Driest. Turbulent boundary layer in compressible fluids. *J. Aero. Sci.*, 18:145–160, 216, 1951.

[71] P. C. Ma, X. I. A. Yang, and M. Ihme. Structure of wall-bounded flows at transcritical conditions. *Phys. Rev. Fluids*, 3(3):034609 1–24, 2018.

[72] K. Kim, J.-P. Hickey, and C. Scalo. Numerical investigation of transcritical-T heat-and-mass-transfer dynamics in compressible turbulent channel flow. In *55th AIAA Aerospace Sciences Meeting*, January 2017.

[73] G. N. Coleman, J. Kim, and R. D. Moser. A numerical study of turbulent supersonic isothermal-wall channel flow. *J. Fluid Mech.*, 305:159–183, 1995.

APPENDICES

A COMPARISON OF THERMODYNAMIC AND TRANSPORT PROPERTIES OF REAL FLUIDS

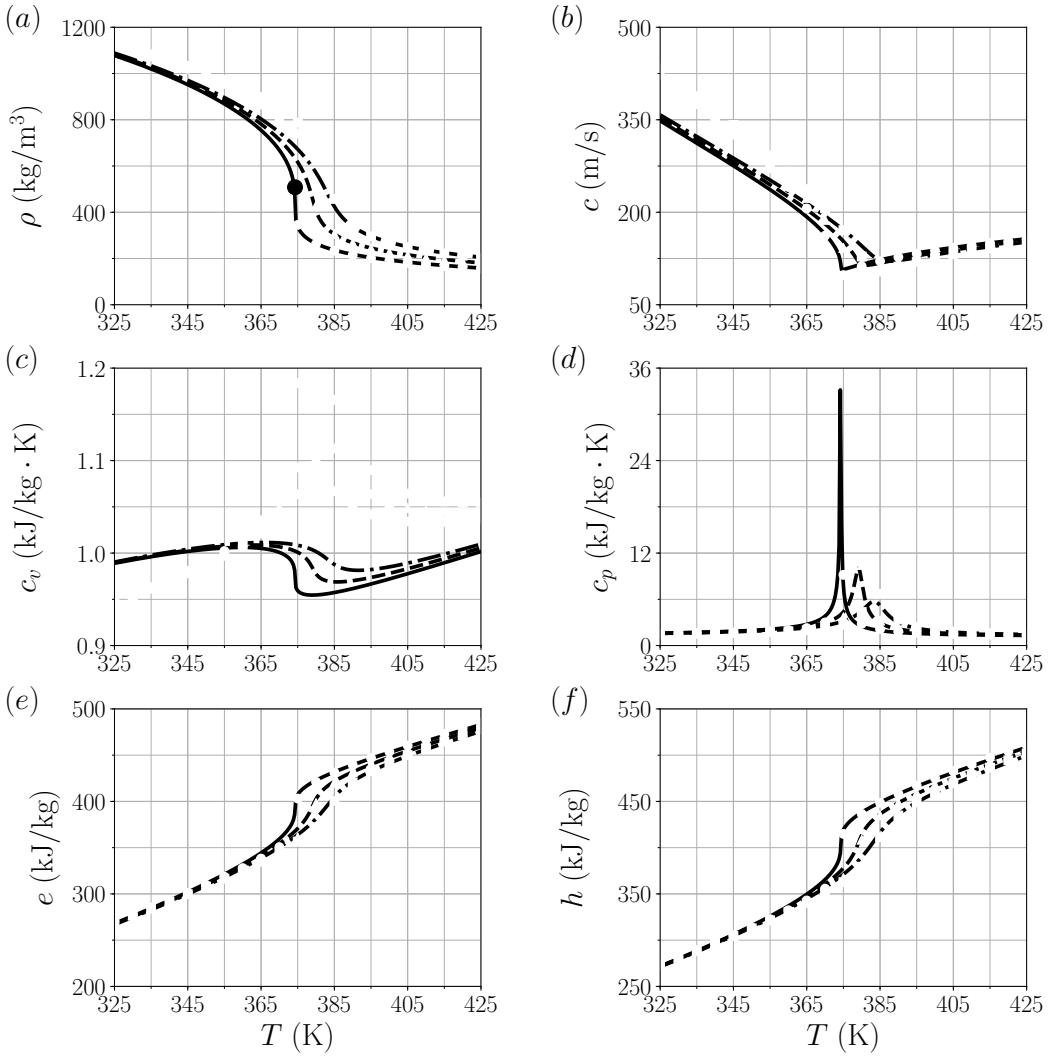

Figure A.1. Thermodynamic properties of R-134a predicted by the PR EoS and the Chung's model (lines) and the NIST data (symbols) at various pressure conditions (—— ○, p_{cr} = 40.590 bar; - - - △, 1.1p_{cr} = 44.649 bar; - · - □, 1.2p_{cr} = 48.708 bar) I. (*a*) Density (● critical point). (*b*) Speed of sound. (*c*) Heat capacity at constant volume. (*d*) Heat capacity at constant pressure. (*e*) Internal energy. (*f*) Enthalpy.

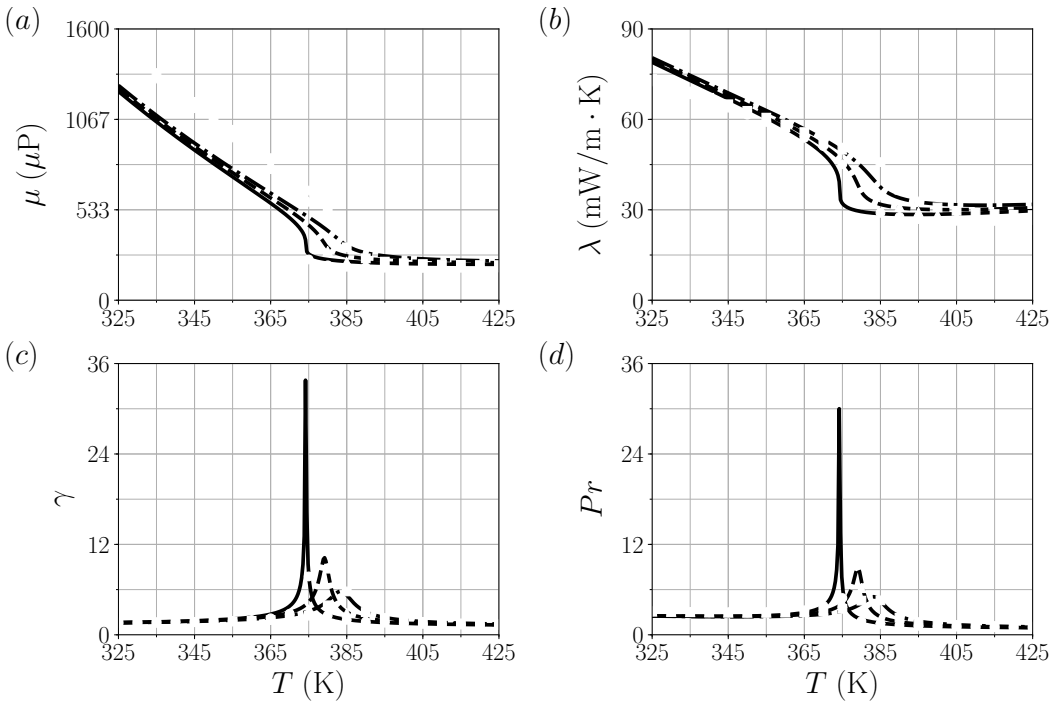

Figure A.2. Thermodynamic properties of R-134a predicted by the PR EoS and the Chung's model (lines) and the NIST data (symbols) at various pressure conditions (—— ○, p_{cr} = 40.590 bar; - - - △, 1.1p_{cr} = 44.649 bar; -·- □, 1.2p_{cr} = 48.708 bar) II. (*a*) Dynamic viscosity. (*b*) Thermal conductivity. (*c*) Specific heat ratio. (*d*) Prandtl number.

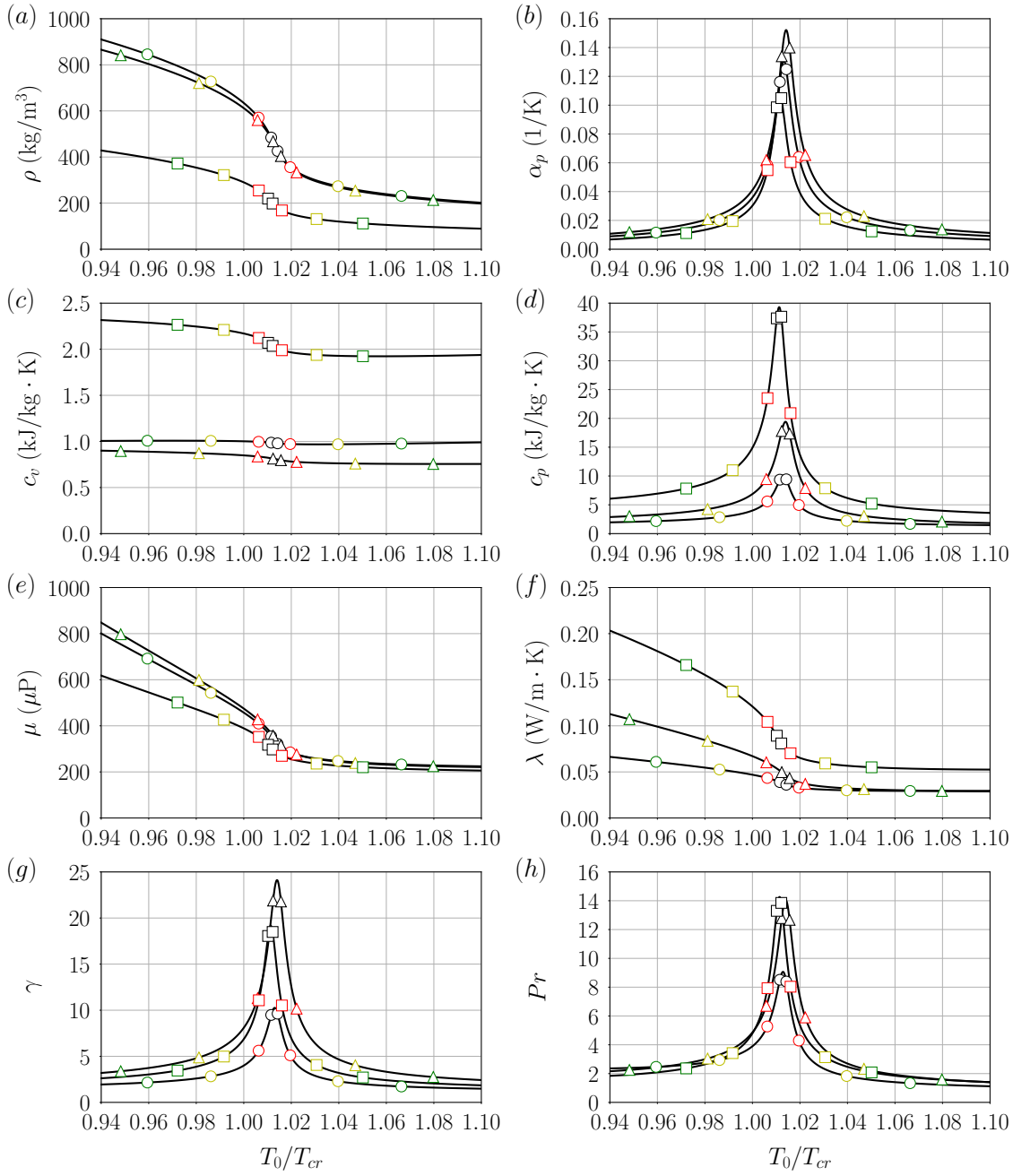

Figure A.3. Thermodynamic properties of R-134a (○), carbon dioxide (△), and methanol (□) predicted by the PR EoS and the Chung's model at $p_b = 1.1p_{cr}$ and $\Delta T = 1$ K (black), 5 K (red), 20 K (yellow), and 40 K (green). (*a*) Density. (*b*) Isobaric thermal expantion coefficient. (*c*) Heat capacity at constant volume. (*d*) Heat capacity at constant pressure. (*e*) Dynamic viscosity. (*f*) Thermal conductivity. (*g*) Specific heat ratio. (*h*) Prandtl number.

B CONSIDERATIONS ON THE TRANSFORMATION BY TRETTEL & LARSSON

Table B.1. Semi-local scaling factors where $\overline{u}^*_\tau(y) = \sqrt{\overline{\tau}_w/\overline{\rho}(y)}$.

Variable for turbulent statistics	Semi-local scaling factors ( )*
y	$\delta^*_v = \overline{\mu}(y)/(\overline{\rho}(y)\overline{u}^*_\tau(y))$
u''_{rms}, v''_{rms}, w''_{rms}	$\overline{u}^*_\tau(y)$
$\widetilde{u''v''}$	$\overline{u}^*_\tau(y)^2$
T'_{rms}	$\overline{T}(y)$
ρ'_{rms}	$\overline{\rho}(y)$

As shown in Figure B.1 (top row), the improper use of the velocity transformation by Trettel & Larsson [69] as inadvertently done in the previous non-refereed communication [72], specifically where $\overline{u}^+$ in Equation (4.5) describing the transformation by Trettel & Larsson [69] (TL) is replaced by $\overline{u}(y)/\overline{u}^*_\tau(y)$, leads to a systematic increase of the intercept in the log-law region for increasing ΔT. Correcting this mistake (Figure B.1 (bottom row)) yields a much more acceptable collapse of bottom and top wall data. The results shown in a later refereed publication by Ma *et al.* [71], who argue that the TL transform performs poorly, especially at the top heated wall, showing very high values of $\overline{u}^+_{TL}$, are in fact consistent with this misuse of the transformation. The latter was implicitly suggested in the previous communication [72] by the proximity of the velocity normalization $\overline{u}^+ = \overline{u}(y)/\overline{u}^*_\tau(y)$ to the equation reporting the TL transformation (Equation (4.5) in Section §4.2.1). If one carefully reviews the published work by Trettel & Larsson [69], nowhere in their manuscript is $\overline{u}^+$ scaled with the semi-local quantity $\overline{u}^*_\tau(y)$. This clarification can benefit the community by

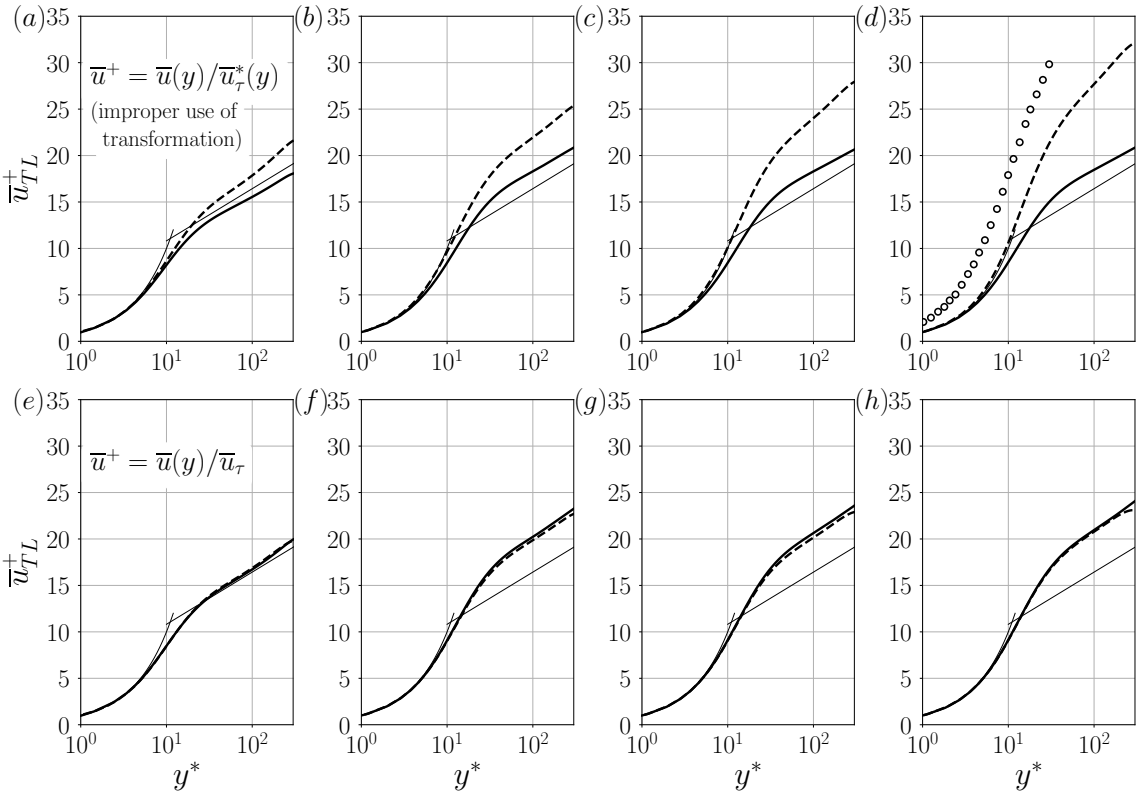

Figure B.1. Mean streamwise velocity versus semi-locally scaled wall-normal coordinate y^* based on the transformation by Trettel & Larsson [69] with improper normalization for the $\overline{u}^+$ term appearing in Equation (4.5), that is $\overline{u}^+ = \overline{u}(y)/\overline{u}^*_\tau(y)$ (top row, (a)–(d)) compared with the correct one $\overline{u}^+ = \overline{u}(y)/\overline{u}_\tau$ (bottom row, (e)–(h)); reference ideal gas data ((a), (e)) and $p_b = 1.1p_{cr}$ and $\Delta T = 5$ K ((b), (f)), 10 K ((c), (g)), and 20 K ((d), (h)); bottom wall (——, thickened) and top wall (- - -). Profiles by the law of the wall ($\overline{u}^+ = y^+$ for the viscous sublayer; $\overline{u}^+ = \frac{1}{\kappa}\ln y^+ + C$ where $\kappa = 0.41$ and $C = 5.2$ for the log-law region) are shown with a thin solid line for reference. Ma *et al.* [71]'s reporting of the Trettel & Larsson [69]'s transformation at the top heated wall of their computational setup is shown with symbols ($\circ$) in subfigure (d) which is consistent with the improper normalization for the $\overline{u}^+$ term in Equation (4.5); they used nitrogen as a working fluid at $p_b = 38.7$ bar $\simeq 1.14p_{cr}$; $T_{bot} = 100$ K and $T_{top} = 300$ K.

reducing confusion on the correct application of the TL transform that may have stemmed from the previous non-refereed communication.

VITA

VITA

Kukjin Kim, born on August 30, 1982 in Seoul, Republic of Korea

03/2002–02/2009, Bachelor of Science in Aerospace and Mechanical Engineering, Korea Aerospace University (Thesis: *Thrust vectoring control by injection of secondary jets inside supersonic nozzle*).

03/2009–02/2011, Master of Science in Aerospace and Mechanical Engineering, Korea Aerospace University (Thesis: *Thermophysical properties of rocket propellant and turbulent mixing dynamics of LOx and kerosene at supercritical conditions*).

08/2013–08/2018, Doctor of Philosophy in Mechanical Engineering, Purdue University (Dissertation: *Turbulent heat transfer in supercritical fluids under transcritical temperature conditions*).

Publications and Presentations

Non-Peer-Reviewed Conference Abstracts/Presentations

- **Kukjin Kim**, Jean-Pierre Hickey, and Carlo Scalo, "Role of near-wall turbulent structures in the heat transfer of transcritical channel flow," *2nd IAEA Technical Meeting on Heat Transfer, Thermal-Hydraulics and System Design for Supercritical Water Cooled Reactors*, Sheffield, UK, August 2016.
- **Kukjin Kim**, Carlo Scalo, and Jean-Pierre Hickey, "Turbulent heat-and-mass transfer in channel flow at transcritical temperature conditions," *69th Annual Meeting of the APS Division of Fluid Dynamics*, Portland, Oregon, USA, November 2016.

Non-Peer-Reviewed Conference Papers

- **Kukjin Kim**, Jean-Pierre Hickey, and Carlo Scalo, "Numerical investigation of transcritical-T heat-and-mass-transfer dynamics in compressible turbulent channel flow," *2017 AIAA Science and Technology Forum (55th AIAA Aerospace Sciences Meeting)*, Grapevine, Texas, USA, AIAA Paper No. 2017-1711, January 2017.

Peer-Reviewed Conference Papers

- **Kukjin Kim**, Carlo Scalo, and Jean-Pierre Hickey, "Turbulent dynamics and heat transfer in transcritical channel flow," *10th International Symposium on Turbulence and Shear Flow Phenomena*, Chicago, Illinois, USA, July 2017.

Peer-Reviewed Journal Papers

- Haifeng Wang and **Kukjin Kim**, "Effect of molecular transport on PDF modeling of turbulent non-premixed flames," *Proceedings of the Combustion Institute*, Vol. 35, Issue 2, pp. 1137–1145, 2015.
- **Kukjin Kim**, Jean-Pierre Hickey, and Carlo Scalo, "Pseudophase change effects in turbulent channel flow under transcritical temperature conditions," *Journal of Fluid Mechanics (under review)*.
- **Kukjin Kim**, Carlo Scalo, and Jean-Pierre Hickey, "Heat transfer characteristics by pseudoboiling in natural convection," *Journal of Fluid Mechanics (in preparation)*.